
Electrochemical Reduction of CO₂: Catalyst and Catalytic System Development

By
Charles Shaughnessy

Submitted to the graduate degree program in the Department of Chemical and Petroleum Engineering and the Graduate Faculty of the University of Kansas in partial fulfillment of the requirements for the degree of Doctor of Philosophy.

Committee Members

Prof. Kevin C. LEONARD, Chair

Prof. Bala SUBRAMANIAM

Prof. Raghunath V. CHAUDHARI

Prof. Alan M. ALLGEIER

April 18, 2019

Date Defended

Prof. Timothy A. JACKSON

The Dissertation Committee for Charles Shaughnessy certifies that this is the approved version of the following dissertation: Electrochemical Reduction of CO₂: Catalyst and Catalytic System Development

Prof. Kevin C. LEONARD, Chair

Date Approved

Abstract

Electrochemical CO₂ reduction to fuels and chemicals could improve industrial sustainability, as the process is readily powered by renewable energy sources. In aqueous solvents it is important to minimize parasitic water reduction. Both metallic indium and indium oxide electrocatalysts typically have high selectivity for producing formate via the electrochemical reduction of CO₂ in aqueous media. It has been suggested that under highly negative potentials, i.e. potentials typically sufficient to reduce indium oxide to In⁰, the native oxide layer on metallic indium or indium oxide particles is not reduced to In⁰ when exposed to CO₂-saturated electrolytes. This meta-stable oxide layer is crucial in the mechanism for producing formate via the two-electron, two-proton reduction of CO₂, however it prevents the catalysis from occurring on In⁰. Herein, we report that by electrochemically reducing In₂O₃ nanocatalysts in Ar-saturated electrolytes *in-situ*, prior to CO₂ exposure, will remove this metastable oxide layer and create a In⁰-In₂O₃ composite. This In⁰-In₂O₃ composite material changes the selectivity and is able to electrochemically reduce CO₂ to CO with near 100% selectivity at relatively low overpotentials (c.a. -1.0 V vs Ag/AgCl). We attribute the change in selectivity to the direct exposure of In⁰ to CO₂ in solution that typically does not exist due to the native oxide layer that forms on In metal. In addition, we observed that the first electron-transfer step to form the surface adsorbed intermediates is highly reversible on the In⁰-In₂O₃ composite, however it is irreversible on an In foil electrode. We also report the utilization of Substrate Generation-Tip Collection Scanning Electrochemical Microscopy (SG-TC SECM) to measure the production of CO as function of applied potential. This technique allows for the collection of CO *in-situ* during the voltammetry experiment as it is produced on the catalytic electrode, which results in accurate potential dependent measurements of CO production.

Despite the good selectivity achieved with the indium catalysts, limited CO₂ solubility in con-

ventional liquid phases starves active electrocatalysts of substrate and results in low conversion rates. In this dissertation, we show that multimolar CO_2 concentrations can be achieved in an organic solvent containing supporting electrolyte at relatively mild CO_2 pressures (<5 MPa) and ambient temperature, a phenomenon driven by working with CO_2 near its critical temperature (31.1 C). We term such CO_2 -rich, supporting electrolyte-containing solutions as CO_2 -eXpanded Electrolytes (CXEs), as significant volumetric expansion of the liquid phase accompanies CO_2 dissolution. CXEs represent a continuum of pressure-tunable media characterized by various concentrations of dissolved CO_2 and supporting electrolyte that enable electrochemistry and electrocatalysis to be performed at high CO_2 concentrations. Cathodic polarization of a model polycrystalline gold electrocatalyst in CXE media enhances CO_2 to CO conversion rates by up to an order of magnitude compared to those attainable at near-ambient pressures. The observed enhancement in catalytic rates stems from markedly increased CO_2 availability. At the highest CO_2 pressures measured (> 2.8 MPa), electrocatalysis is significantly attenuated. Taken together, these studies reveal that pressure-tunable CXE media could improve the performance of many known electrocatalysts by alleviating substrate starvation. Simultaneously, the non-monotonic enhancement of CO_2 reduction with pressure suggests that pressure is a crucial variable in maximizing the efficiency of electrocatalytic CO_2 conversion.

Investigating the non-monotonic behavior for CO_2 reduction in CO_2 Expanded Electrolytes we utilize the ability to tunably solvate multi-molar amounts of CO_2 . By utilizing tunability to generate cyclic voltammograms at widely separated concentrations of CO_2 it was found that on multiple catalysts the catalytic rate decreased at the highest concentrations of CO_2 . Using COMSOL modeling of CO_2 electroreduction on gold we show that the maximum value for catalysis is a result of a decrease in the rate of an elementary reaction step at high concentrations of CO_2 .

Continuing the use of CO_2 Expanded Electrolytes to understand the kinetics of CO_2 reduction, the kinetics of a homogeneous catalyst, $\text{Re}(\text{CO})_3(\text{bpy})\text{Cl}$, were investigated. Again the pressure tunability of CXEs was exploited to generate cyclic voltammograms at widely separated concentrations of CO_2 . The observed rates increased until a plateauing rate with increasing concentration of CO_2 . These rates match well with Michealis-Menten kinetics for enzymatic catalysis. Using the Michealis-Menten equation, the kinetic rate constant for electrochemical reduction was found. After the plateau a reduction in the catalytic rate was observed at the highest degree of expansion,

consistent with what has previously been observed for heterogeneous catalysts. The use of CXEs to investigate the relationship between CO_2 concentration and catalytic rate will guide the future development of electrochemical CO_2 reduction systems.

Acknowledgements

It is said that it takes a village to raise a child, and I believe that it takes more than that to raise a Ph.D, thus the following is an incomplete list of who has helped me along the way to this achievement. First and foremost I would like to thank my family. My parents, Anne and Sean Shaughnessy, my siblings, John, Aidan, Bernadette, and Ambrose and the entire extended clan have been supporting me for my entire life. I could not have achieved this without them.

Academically, I must first thank my advisor, Kevin Leonard. He took a chance on a random chemistry graduate who wanted to come work in chemical engineering. Over the last four years I have learned materials science, kinetics, and electrochemistry from him. It has been a genuine pleasure working for and with him. Next, I would like to thank the members of my committee, Bala Subramaniam, Alan Allgeier, RV Chaudhari, and Tim Jackson for shepherding me through the process. Lastly I would like to thank two professors from my previous schools, Ellen Steinmiller from the University of Dallas, and Barbara Spohr from Dodge City Community College. I would not have continued in, or even started my chemistry career without these two excellent teachers and mentors.

I could not have carried out the research I have done without support from a team. First, the SUSChem team which includes, Kevin Leonard, Bala Subramaniam, James Blakemore, David Sconyers, Hyun-Jin Lee, and Tyler Kerr. The multiplicity of talent, ideas, and specialities brought to the table by these researchers has enabled me to learn and grow in my abilities as a researcher. I also would like to thank my labmates, Joe Barforoush, Dylan Jantz, and Tess Souferling for helping me with my explorations, classes, and accompanying me through the last four years in the lab. In addition, I would like to acknowledge the unique experimental facilities made available by the Subramaniam group and the CEBC to measure the physical and thermodynamic properties of

carbon dioxide-expanded liquids and perform catalyst characterization. Last, but not least, I could not have accomplished my work without the skill of Ed Atchinson in both CAD and as a machinist.

Lastly I would like to thank all of my friends from UD, BC, KC, and KU. You know who you are, and you've made the last eight years pretty amazing.

My deepest thanks go out to all of the people here, and anyone I may have inadvertently left out. I am looking forward with great excitement to the places we will find together going forward.

Dedicated to Hermena Skalsky

“The wheat’s looking pretty good down here”

Contents

1	Overview and Introduction	1
1.1	The Problem of CO ₂	1
1.2	Electrochemical Reduction of CO ₂	2
1.2.1	Heterogeneous Catalytic Reduction of CO ₂	3
1.2.2	Homogeneous Catalytic Reduction of CO ₂	8
1.3	Gas Expanded Liquids	9
1.3.1	Gas Expanded Liquids for Conventional Catalysis	10
1.3.2	Gas Expanded Liquids for Electrocatalysis:	10
1.4	Goals of Dissertation	11
2	Selective Electrochemical CO₂ Reduction to CO Using In-Situ Reduced In₂O₃ Nanocatalysts	22
2.1	Abstract	22
2.2	Introduction	23
2.3	Materials and Methods	25
2.3.1	Chemicals	25
2.3.2	Catalyst Synthesis	25
2.3.3	Materials Characterization	26
2.3.4	Electrochemical and Product Characterization	26
2.4	Results and Discussion	26
2.4.1	Materials Synthesis and Characterization	26
2.4.2	Electrochemical Characterization	28

2.4.3	Product Detection and Scanning Electrochemical Microscopy	31
2.5	Conclusions	33
2.6	Acknowledgement of Contributions	33
2.7	Supporting Figures	34
3	Enhanced Electrocatalytic CO₂ Conversion in Pressure-Tunable CO₂-Expanded Electrolytes	43
3.1	Abstract	43
3.2	Introduction	44
3.3	Experimental	46
3.3.1	General considerations	46
3.3.2	Vapor-liquid equilibrium (VLE) studies	46
3.3.3	Electronic absorption spectroscopy	46
3.3.4	Electrochemical experiments	46
3.3.5	Sample preparation for gas chromatography	47
3.3.6	Product detection by gas chromatography	48
3.4	Results and Discussion	48
3.5	Acknowledgement of Contributions	59
3.6	Supporting Information	60
3.6.1	Reactor Design for Studies Involving CO ₂ -Expanded Electrolytes	60
3.6.2	Supporting Electrochemical Experiments	63
3.6.3	Electronic Absorbance Spectroscopy Supporting Experiments	73
3.6.4	Gas Chromatography Supporting Figures	78
3.6.5	COMSOL Modeling	84
4	Insights Into the Pressure Dependent Reaction Rates for the Electrochemical Reduction of CO₂ in CO₂ Expanded Electrolytes	94
4.1	Introduction	95
4.2	Materials and Methods	96
4.3	Results and Discussion	97
4.4	Conclusion	104

4.5	Supporting Information	106
5	Insights Into the Kinetics of $\text{Re}(\text{CO})_3(\text{bpy})\text{Cl}$ for the Electrochemical Reduction of CO_2 in CO_2 Expanded Electrolytes	117
5.1	Abstract	117
5.2	Introduction	118
5.3	Experimental	119
5.3.1	Reactor	119
5.3.2	Materials	119
5.3.3	Electrochemical reaction procedures	119
5.3.4	Product detection by gas chromatography	120
5.4	Results and Discussion	121
5.5	Conclusion	128
5.6	Acknowledgement of Contributions	128
5.7	Supporting Figures	129
6	Conclusions and Future Work	135
6.1	Conclusion	135
6.2	Future Work	137
6.3	Final Thoughts	142

List of Figures

1.1	Chronological growth of atmospheric CO ₂ concentration (red line) and seasonally corrected concentration of CO ₂ (black line) measured at the Mauna Loa Observatory. ¹	1
1.2	Aprotic adsorbed mechanism for CO ₂ reduction	4
1.3	Protic adsorbed mechanism for CO ₂ reduction	4
1.4	Aprotic nonadsorbed mechanism for CO ₂ reduction	5
1.5	Protic nonadsorbed mechanism for CO ₂ reduction	5
2.1	Schematic of the synthesis route for producing the In ⁰ -In ₂ O ₃ composite structure. .	25
2.2	X-ray Diffraction data of the In ⁰ -In ₂ O ₃ composite structure (top) and the untreated In ₂ O ₃ nanoparticles (bottom) showing the presence of both In ⁰ (blue arrows) and In ₂ O ₃ in the composite structure, but only In ₂ O ₃ in the untreated nanoparticles (a). Ten consecutive cyclic voltammograms (1 st cycle - black trace, 10 th cycle - blue trace) of the In ₂ O ₃ nanoparticles in Ar-saturated 0.1 M Na ₂ SO ₄ at 100 mV s ⁻¹ showing that the In ₂ O ₃ reduction peak increases with each subsequent cyclic voltammogram (b). SEM images of the untreated In ₂ O ₃ nanoparticles (c), the In ⁰ -In ₂ O ₃ after voltammetry cycling in Ar-saturated Na ₂ SO ₄ (d), and In ⁰ -In ₂ O ₃ after voltammetry cycling in CO ₂ -saturated Na ₂ SO ₄ (e).	27

2.3	Cyclic voltammograms of the $\text{In}^0\text{-In}_2\text{O}_3$ composite structure, a In foil electrode, and untreated In_2O_3 nanoparticles. Comparison voltammograms of the $\text{In}^0\text{-In}_2\text{O}_3$ composite structure and an In foil electrode at 10 mV s^{-1} in CO_2 -saturated $0.1 \text{ M Na}_2\text{SO}_4$ (a). Comparison voltammograms of untreated In_2O_3 nanoparticles an In foil electrode at 50 mV s^{-1} in CO_2 -saturated $0.1 \text{ M Na}_2\text{SO}_4$ (b). Comparison voltammograms of the $\text{In}^0\text{-In}_2\text{O}_3$ composite structure in CO_2 -saturated and Ar-saturated $0.1 \text{ M Na}_2\text{SO}_4$ at 10 mV s^{-1} (c). Comparison voltammograms of the In foil electrode in CO_2 -saturated and Ar-saturated $0.1 \text{ M Na}_2\text{SO}_4$ at 10 mV s^{-1} (d). Comparison voltammograms between the 1^{st} cycle and 6^{th} cycle of the $\text{In}^0\text{-In}_2\text{O}_3$ composite structure in CO_2 -saturated $0.1 \text{ M Na}_2\text{SO}_4$ (e).	28
2.4	Schematic of the SG-TC SECM experiment showing the collection of CO but not COOH^- on a Pt tip electrode (a). Collection tip current vs time as a function of the potential applied to the $\text{In}^0\text{-In}_2\text{O}_3$ electrode in CO_2 -saturated $0.1 \text{ M Na}_2\text{SO}_4$ (b). Product collection charge density as a function of the potential applied to the catalytic electrode for both the $\text{In}^0\text{-In}_2\text{O}_3$ composite and the In foil electrode in both CO_2 -saturated and Ar-saturated $0.1 \text{ M Na}_2\text{SO}_4$ (c).	30
2.5	Ratio of the peak area of the reduction wave over the oxidation wave for consecutive voltammetry cycles of the In_2O_3 nanoparticles in Ar-saturated Na_2SO_4 . Inset is a photograph of the In_2O_3 electrode showing the coloration change (black circle) that occurs after cycle in CO_2 saturated Na_2SO_4	34
2.6	Current as a function of time for a 200 micron diameter Pt SECM tip electrode in Ar-saturated, CO -saturated, H_2 -saturated $0.1 \text{ M Na}_2\text{SO}_4$ along with 0.1 M NaCOOH at $+0.2 \text{ V vs Ag/AgCl}$. This shows that CO and H_2 can be collected on a Pt tip electrode while COOH^- can not be collected.	35
2.7	Current as a function of time for a 200 micron diameter Pt SECM tip electrode in Ar-saturated, CO -saturated, H_2 -saturated $0.1 \text{ M Na}_2\text{SO}_4$ along with 0.01 M NaCOOH in $0.1 \text{ M Na}_2\text{SO}_4$ at $+0.2 \text{ V vs Ag/AgCl}$. This shows that CO and H_2 can be collected on a Pt tip electrode while COOH^- can not be collected.	35

2.8	Schematic showing the cell used for the bulk electrolysis measurements (a). Example gas chromatography data showing the detection of CO and non-quantifiable detection of H ₂ (b).	36
2.9	Cyclic voltammetry data of CO ₂ -saturated and Ar-saturated 0.1 M Na ₂ SO ₄ in pH 4.5 acetate buffer taken at 5 mV s ⁻¹ on both a thinly coated In ⁰ -In ₂ O ₃ composite sample and on In foil. This demonstrates that the pH change that occurs when the electrolyte is saturated with CO ₂ is not responsible for the increase in catalytic current.	37
3.1	CO ₂ expansion of electrolytes. (a) Change in volume of a 10 mL sample of MeCN (black) and MeCN initially containing 0.4 M TBAPF ₆ (blue) upon CO ₂ pressurization. (b) Increasing CO ₂ concentration as the volume expands with increasing pressure. MeCN (black) and MeCN initially containing 0.4 M TBAPF ₆ (blue). The CO ₂ concentration in the expanded liquid asymptotically approaches the concentration of liquid CO ₂ (gray dashed line). (c) Cyclic voltammetry of metallocene complexes in CO ₂ -expanded electrolyte solution (3.18 MPa CO ₂). 0.4 M TBAPF ₆ present in acetonitrile prior to expansion. Redox couples of ferrocene (E _{p,1/2} = 0 V), decamethylferrocene (E _{p,1/2} = -0.5 V) and cobaltocene (E _{p,1/2} = -1.34 V) shown. Working electrode was the basal plane of highly-oriented pyrolytic graphite (HOPG, 0.09 cm ²).	49
3.2	Cyclic voltammetry of the Fc ⁺⁰ redox couple and extracted experimental diffusivities as a function of CO ₂ pressure in CXEs. (a) Experimental (solid dark lines) and simulated (transparent shade lines) cyclic voltammetry of ferrocene conducted under various CO ₂ pressures at 25 °C. Black: 0.79 MPa of CO ₂ . Blue: 3.2 MPa of CO ₂ . Red: 5.2 MPa CO ₂ . Working electrode was the basal plane of highly-oriented pyrolytic graphite (HOPG, 0.09 cm ²). Scan rate 100 mV/s. (b) Diffusion coefficients of ferrocene as obtained from the cyclic voltammetry data as a function of CO ₂ pressure. Error bars were calculated directly from experimental data for gray points, and from variance in low-pressure curve fits for black points. Black: Obtained from simulation of voltammetry. Gray: Determined experimentally via double-step chronoamperometry. The gray line is only intended to guide the eye.	52

3.3	Electrochemical current response as a function of potential and pressure in CXE media. (a) Cyclic voltammetry conducted under varying pressures of CO ₂ (Red: 0.3 MPa; Blue: 3.2 MPa; Black: 5.2 MPa; Gray: Control under 0.3 MPa of Ar gas. Au disk microelectrode; A = 0.031 mm ² ; scan rate: 100 mV/s. (b) Steady-state currents with the same electrode at -2.5 V as a function of CO ₂ pressure. Following initial agitation to achieve equilibrium CO ₂ dissolution in the electrolyte phase, solution was quiescent during the cyclic voltammetry experiments. The gray line is parabolic and intended only to guide the eye.	55
3.4	Enhancement of electrochemical CO ₂ reduction in CXE media. (a) Plot of charge passed and CO detected by gas chromatography for different bulk electrolysis times, using a 1.2 cm ² Au coil electrode. Dark circles represent charge passed in coulombs and light circles CO detected in μmol under 3.2 MPa CO ₂ (blue) and 0.3 MPa CO ₂ (black). (b) Faradaic efficiency following various bulk electrolysis times with respect to CO detected. Error bars are calculated based on replicate experiments across the full pressure range. Blue: 3.2 MPa CO ₂ . Black: 0.3 MPa CO ₂ . Lines shown are linear fits, assuming efficiency for CO production remains constant with time. (c) Pressure dependence of CO formation following bulk electrolysis for 8 h. Gray line is parabolic and intended only to guide the eye. The electrolysis experiments were performed at -2.5 V vs Fc ^{+ / 0} without stirring.	58
3.5	CAD drawing of reactor vessel. (1) 50 mL Parr reaction vessel. (2) Teflon liner. (3) Stir Rod. (4) Custom reactor cap with PTFE O-ring seal. (5) Ceramtec electrical feedthrough. (6) Split-ring clamp. (7) Magnetic drive adaptor. (8) Parr magnetic drive.	61
3.6	CAD drawings of cap assembly. (a) Assembled cap with feedthroughs. (b) Custom cap. (c) Ceramtec electrical feedthrough.	61
3.7	Pressure stability within reactor over time. Plot showing low pressure variance within the reactor (± 50 kPa) over a period of over twelve hours	62
3.8	Temperature stability within reactor over time. Plot showing low temperature variance within the reactor (± 0.2 K) over a period of over twelve hours.	62

3.9	<p>Measurements of solution resistance as a function of pressure on carbon. Data were collected with a commercial script provided with the potentiostat; this script relies on controlled-potential electrochemical impedance spectroscopy (EIS) to determine the solution resistance by interpreting collected data using a model circuit. The data points shown are average values collected on an HOPG working electrode ($A = 0.09 \text{ cm}^2$) across quadruplicate measurements at four different potentials (-0.2 V, -0.5 V, -0.9 V and -1.2 V vs. $\text{Fc}^{+/0}$). Thus each data point and error represents sixteen unique measurements. Error bars are shown as $\pm 1\sigma$</p>	64
3.10	<p>Measurements of solution resistance as a function of pressure on gold. Data were collected with a commercial script provided with the potentiostat; this script relies on controlled-potential electrochemical impedance spectroscopy (EIS) to determine the solution resistance by interpreting collected data using a model circuit. , The data points shown are average values collected on an gold working microelectrode ($A = 0.031 \text{ mm}^2$) across quadruplicate measurements at four different potentials (-0.2 V, -0.5 V, -0.9 V and -1.2 V vs. $\text{Fc}^{+/0}$). Thus each data point and error represents sixteen unique measurements. Error bars are shown as $\pm 1\sigma$</p>	65
3.11	<p>Cyclic voltammetry of metallocenes at ambient and high pressures. Cyclic voltammetry of the ferrocenium/ferrocene ($\Delta E_{p,\text{atm}} = 82 \text{ mV}$, $\Delta E_{p,5.2\text{MPa}} = 159 \text{ mV}$), decamethylferrocenium/decamethylferrocene ($\Delta E_{p,\text{atm}} = 91 \text{ mV}$, $\Delta E_{p,5.2\text{MPa}} = 130 \text{ mV}$) and cobaltocenium/cobaltocene ($\Delta E_{p,\text{atm}} = 76 \text{ mV}$, $\Delta E_{p,5.2\text{MPa}} = 122 \text{ mV}$) quasi-reversible redox couples under ambient pressure of N_2 in a glovebox (gray) and at 5.2 MPa in the high pressure cell (black). HOPG working electrode (0.09 cm^2), 100 mV/s scan rate.</p>	66
3.12	<p>Pressure dependence of the relative midpoint potentials of metallocenes. Plot of the deviation in the midpoint potentials of cobaltocene and decamethylferrocene as a function of CO_2 pressure. Note there is no distinguishable difference even at the highest pressures, suggesting the medium's behavior is still dictated primarily by the properties of acetonitrile.</p>	67

3.13	Current dependence on scan rate at elevated pressure with Cp2Fe. Plot demonstrating diffusional behavior of ferrocene in CO ₂ expanded electrolyte via application of the Randles-Sevcik equation on variable scan rate data. Linear fits of the observed current versus the square root of scan rate are forced through zero. Reactor was initially charged with 2 mM ferrocene and 0.4 M TBAPF ₆ before being pressurized to 3.7 MPa CO ₂ . HOPG working electrode (0.09 cm ²).	68
3.14	Current dependence on scan rate at elevated pressure with Cp*2Fe. Plot demonstrating diffusional behavior of ferrocene in CO ₂ expanded electrolyte via application of the Randles-Sevcik equation on variable scan rate data. Linear fits of the observed current versus the square root of scan rate are forced through zero. Reactor was initially charged with 2 mM decamethylferrocene and 0.4 M TBAPF ₆ before being pressurized to 3.7 MPa CO ₂ . HOPG working electrode (0.09 cm ²).	69
3.15	Potential of ferrocene internal standard before and after electrolysis. Cyclic voltammetry of the ferrocenium/ferrocene redox couple at 3.2 MPa CO ₂ , both before (black) and after (gray) 14 h of polarization at -2.5 V vs. Fc ⁺⁰ . The redox couple is originally +694 mV versus reference, and after electrolysis there is a minor 30 mV shift to +664 mV vs. reference.	70
3.16	Current response as a function of pressure in CXE media. Chronoamperometry performed under variable pressures of CO ₂ . Black: 0.24 MPa of CO ₂ . Red: 5.1 MPa CO ₂ . Blue: 3.2 MPa. 1.16 cm ² Au coil electrode, potential held at -2.5 V vs. Fc ⁺⁰	70
3.17	Steady-state current response as a function of pressure in CXE media. Cyclic voltammetry conducted under variable pressure of CO ₂ . Blue: 3.2 MPa of CO ₂ . Red: 5.2 MPa CO ₂ . Black: 0.3 MPa CO ₂ . 200 μm Au disk electrode, scan rate 100 mV/s for CVs. Squares are the steady-state currents for the electrode at a given potential after 100 seconds of polarization.	71
3.18	Representative current response as a function of potential in CXE media. Chronoamperometry performed at various potentials under 3.2 MPa of CO ₂ . Potentials reported in V vs. Fc ⁺⁰ . 200 μm Au disk electrode	71

3.19	Current response with time in nonexpanded media. Chronoamperometry performed for 8 hours under 0.24 MPa of CO ₂ . 1.16 cm ² Au coil electrode, potential held at -2.5 V vs. Fc ⁺⁰	72
3.20	Current response with time at elevated pressure. Chronoamperometry performed for 8 hours under 3.2 MPa of CO ₂ . 1.16 cm ² Au coil electrode, potential held at -2.5 V vs. Fc ⁺⁰	72
3.21	Electronic absorbance spectrum of [Re(CO) ₃ (bpy)MeCN][PF ₆]. UV-visible spectrum taken in the absence of CO ₂ to determine the extinction coefficient of the complex's absorption bands. 80 μM [Re(CO) ₃ (bpy)MeCN][PF ₆], 0.4 M TBAPF ₆ in MeCN. . .	73
3.22	Charge transfer band of [Re(CO) ₃ (bpy)MeCN][PF ₆] in MeCN. UV-visible spectroscopy performed initially with 80 μM [Re(CO) ₃ (bpy)MeCN][PF ₆] in MeCN at progressively increasing pressures of CO ₂ . Reduction in the absorption value corresponds to dilution of the metal complex taking place during volume expansion at higher pressures. Features present include π - π* (ca. 320 nm) bands and a broad MLCT band (ca. 350 nm).	74
3.23	Charge transfer band of [Re(CO) ₃ (bpy)MeCN][PF ₆] in electrolyte. UV-visible spectroscopy performed initially with 80 μM [Re(CO) ₃ (bpy)MeCN][PF ₆] and 0.4 M TBAPF ₆ in MeCN at progressively increasing pressures of CO ₂ . Reduction in the absorption value corresponds to dilution of the metal complex taking place during volume expansion at higher pressures.	75
3.24	[Re] concentration change with volume expansion. Relationship between volumetric expansion and dissolved complex concentration with increasing pressure of CO ₂ . Black line: Volumetric expansion curve of MeCN. Black squares: Concentration of rhenium complex was initially 80 μM [Re(CO) ₃ (bpy)MeCN][PF ₆], and determined from the absorption of the [Re] species at 316 nm.	75

3.25	[Re] concentration change with volume expansion in electrolyte. Relationship between volumetric expansion and dissolved complex concentration with increasing pressure of CO ₂ . Blue line: Volumetric expansion curve of MeCN initially supporting 0.4 M TBAPF ₆ . Blue squares: Concentration of rhenium complex in electrolyte, initially 80 μM [Re(CO) ₃ (bpy)MeCN][PF ₆] and 0.4 M TBAPF ₆ , and determined from the absorption of the [Re] species at 316 nm.	76
3.26	Electronic absorption spectrum of ferrocene. UV-visible spectrum taken in the absence of CO ₂ to determine the extinction coefficient of the complex's different absorption bands. 8 mM ferrocene, 0.4 M TBAPF ₆ in MeCN.	76
3.27	d-d band of ferrocene. UV-visible spectrum of ferrocene showing the extinction coefficient of a d-d band of interest. 8 mM ferrocene, 0.4 M TBAPF ₆ in MeCN. . . .	77
3.28	Response of d-d band with increasing CO ₂ pressure. UV-visible spectroscopy performed initially with 8 mM ferrocene and 0.4 M TBAPF ₆ in MeCN at progressively increasing pressures of CO ₂ . Reduction in the absorption value corresponds to dilution of the metal complex taking place during volume expansion at higher pressures.	77
3.29	Production of CO as a function of CO ₂ pressure. Mirroring the figure in the main text, this is a plot of the observed rates of CO production, determined from gas chromatography, as a function of CO ₂ pressure. Error bars are calculated from the standard deviation of replicate measurements.	78
3.30	Quantification of detected carbon monoxide at various pressures. Bar plot depicting the average quantity of gas products generated at different pressures following 8 h bulk electrolysis at -2.5 V vs. Fc ^{+ / 0} . 1.16 cm ² Au coil electrode used. Trace amounts of methane (nmol quantities) were detected in all experiments from an impurity in the CO ₂ gas supply.	79
3.31	FID gas chromatogram of near-ambient pressure electrolysis headspace. Gas chromatogram of headspace gas from an 8 h electrolysis at -2.5 V vs. Fc ^{+ / 0} on Au wire, 0.4 MPa CO ₂ , FID with methanizer. Inset shows a detailed view of CO signal. No other products were detected by the methanizer-equipped FID. Peak intensities are large enough that valve changes are not visible.	79

3.32	TCD gas chromatogram of near-ambient pressure electrolysis headspace. Gas chromatogram of headspace gas from an 8 h electrolysis at -2.5 V vs. $\text{Fc}^{+/0}$ on Au wire at 0.4 MPa CO_2 , TCD. No other products were detected by the TCD.	80
3.33	FID gas chromatogram of mid pressure electrolysis headspace. Gas chromatogram of headspace gas from an 8 h electrolysis at -2.5 V vs. $\text{Fc}^{+/0}$ on Au wire at 3.2 MPa CO_2 , FID with methanizer. Inset shows a detailed view of CO signal. Peak intensities are large enough that valve changes are not visible.	80
3.34	TCD gas chromatogram of mid pressure electrolysis headspace. Gas chromatogram of headspace gas from an 8 h electrolysis at -2.5 V vs. $\text{Fc}^{+/0}$ on Au wire at 3.2 MPa CO_2 , TCD. Inset shows a detailed view of H_2 and N_2/O_2 signals. No other products were detected by the TCD.	81
3.35	FID gas chromatogram of high pressure electrolysis headspace. Gas chromatogram of headspace gas from an 8 h electrolysis at -2.5 V vs. $\text{Fc}^{+/0}$ on Au wire at 5.2 MPa CO_2 , FID with methanizer. Inset shows a detailed view of CO signal. Peak intensities are large enough that valve changes are not visible.	81
3.36	TCD gas chromatogram of high pressure electrolysis headspace. Gas chromatogram of headspace gas from an 8 h electrolysis at -2.5 V vs. $\text{Fc}^{+/0}$ on Au wire at 5.2 MPa CO_2 , TCD. Inset shows absence of an H_2 signal. No other products were detected by the TCD.	82
3.37	FID gas chromatogram of electrolyte liquid. Gas chromatogram of liquid sampled from electrolyte solution, FID. Inset shows a detailed view of the only signal observed, associated with the electrolyte itself. Peak intensities are large enough that valve changes are not visible.	82
3.38	FID gas chromatogram of liquid from mid pressure electrolysis. Gas chromatogram of liquid sampled from an 8 h electrolysis on Au wire at -2.5 V vs. $\text{Fc}^{+/0}$, 3.2 MPa CO_2 , FID. Inset shows a detailed view of the only signal observed, associated with the electrolyte itself. Peak intensities are large enough that valve changes are not visible.	83

3.39	FID gas chromatogram of CO ₂ gas. Control gas chromatogram of high purity CO ₂ gas used in all other experiments, FID with methanizer. Besides trace amounts of methane impurity, no other gases were detected. Peak intensities are large enough that valve changes are not visible.	83
3.40	TCD gas chromatogram of CO ₂ gas. Control gas chromatogram of high purity CO ₂ gas used in all other experiments, TCD. Aside from the response at ca. 5 min retention time, no other signals were observed.	84
3.41	Reactor mesh for COMSOL Cp ₂ Fe diffusion simulations.	85
3.42	Reactor mesh near surface for COMSOL Cp ₂ Fe diffusion simulations. Outer rectangle of electrode is modeled as an insulating sheath to capture the electrode shape.	86
4.1	Pressure dependant properties of CO ₂ -eXpanded Electrolytes. (a) Volumetric Expansion, (b) CO ₂ concentration, (c) Diffusion Coefficient of CO ₂ , (d) Solution resistance.	98
4.2	Pressure dependant cyclic voltammograms. (a) CO ₂ reduction on polycrystalline Au, (b) CO ₂ reduction on polycrystalline Cu, (c) Current density as a function of CO ₂ pressure at -2.7 V.	100
4.3	(Pressure dependant cyclic voltammograms for the electrochemical reduction of CO ₂ on Au. (a) Experimental, (b) Simulated, (c) Combined. (Black 0.17 MPa, Orange 1.44 MPa, Red 3.13 MPa, Green 4.48 MPa, Blue 5.10 MPa	102
4.4	Relationship between volumetric expansion and k_1 as a function of CO ₂ pressure	104
4.5	Model sensitivity for the elementary rates of reaction over five orders of magnitude. (k1 : Red: 2×10^{-10} Orange: 2×10^{-9} , Green: 2×10^{-8} Blue: 2×10^{-7} Violet: 2×10^{-6} mol ⁻¹ s ⁻¹ m ³)(k2 : Red: 1×10^3 Orange: 1×10^2 Green: 1×10^1 , Blue: 1 Violet: 1×10^{-1} mol ⁻¹ s ⁻¹ m ³)(k3 : Red: 8×10^{-7} Orange: 8×10^{-6} Green: 8×10^{-5} Blue: 8×10^{-4} Violet: 8×10^{-3} s ⁻¹)(k4 : Red: 5 Orange: 5×10^1 Green: 5×10^2 Blue: 5×10^1 Violet: 5×10^4 s ⁻¹) Black: Experimental for all cases	107
4.6	Comsol mesh reproducing the geometry of the reactor for CO ₂ reduction simulations	108
4.7	Comsol mesh reproducing the geometry of the reactor for CO ₂ reduction simulations zoomed into the area around the electrode	108

4.8	Cyclic voltammograms for CO ₂ reduction on gold in CXEs corrected for resistance. (Red: 3.13 Mpa, Blue: 5.10 MPa, Black: 0.17 MPa, Solid: Experimental with IR correction, Dashed: Simulated with IR correction)	109
4.9	Utilizing the calculated k ₁ for atmospheric [CO ₂] for all pressures (Red: Simulated 3.13 Mpa, Orange: Simulated 0.17 MPa, Green: Simulated 5.10 MPa, Black: Experimental at all pressures)	110
4.10	EIS data and fits for 5.10 MPa CO ₂ on 200 μm diameter Au disk electrode. Insert is a zoom of region critical for finding solution resistance.	111
4.11	EIS data and fits for 3.13 MPa CO ₂ on 200 μm diameter Au disk electrode. Insert is a zoom of region critical for finding solution resistance.	112
4.12	EIS data and fits for 0.17 MPa CO ₂ on 200 μm diameter Au disk electrode. Insert is a zoom of region critical for finding solution resistance.	113
5.1	Cyclic voltammetry of the rhenium catalyst. (upper left) Forward sweep of cyclic voltammetry experiments performed on the rhenium system at various pressures (black 0.44 MPa, dark gray 0.61 MPa, light gray 0.79 MPa). The initial visible reduction event (E _{p,c} = -1.75 V) corresponds to a primarily ligand-centered reduction of the [Re] complex, after which the onset of catalysis is observed. A kinetic potential shift can be seen in the data, where with increasing pressure (and concomitantly concentration of CO ₂), the onset potential of catalysis is moving toward more positive values. (upper right) Full range of the voltammetry at 0.44 MPa. (lower) Reversible electrochemistry of the rhenium catalyst in the absence of CO ₂ , at ambient conditions inside a glovebox. All experiments were conducted with 2 mM [Re], [TBAPF ₆] _{initial} = 0.4 M, and an HOPG working electrode (A = 0.09 cm ²) at a 100 mV/s scan rate.	121
5.2	Representative Re(CO) ₃ (bpy)Cl catalytic sweep at 3.13 MPa (a), Linearization of this sweep using FOWA (b)	123

5.3	Observed rates of electrocatalytic reduction by $\text{Re}(\text{CO})_3(\text{bpy})\text{Cl}$ in CO_2 expanded acetonitrile at various concentrations of CO_2 . $\text{Re}(\text{CO})_3(\text{bpy})\text{Cl}$ concentration for all experiments calibrated to 2 mM after expansion, working electrode was the basal plane of highly-oriented pyrolytic graphite (HOPG, 0.09 cm ²). 0.4 M concentration of TBAPF_6 prior to expansion. Error bars are calculated from the error of a linear fit applied to replicate experiments at multiple scan rates.	124
5.4	Reaction used for Michaelis-Menten kinetic model where E is the catalyst, S is CO_2 , ES is the catalyst\CO ₂ complex, and P is CO	125
5.5	Rhenium concentration dependence of kinetics under zero-order conditions for CO_2 . (left) Concentration dependence of rhenium on the calculated observed rate, determined from FOWA. Cell pressurized to 2.5 MPa CO_2 (3.5 M CO_2), working electrode was the basal plane of highly-oriented pyrolytic graphite (HOPG, 0.09 cm ²). 0.4 M concentration of TBAPF_6 prior to expansion. (right) Normalized concentration dependence exhibiting linear behavior. Error bars are calculated from the error of a linear fit applied to replicate experiments at multiple scan rates.	126
5.6	Kinetics of electrocatalysis by the rhenium complex. Rate of electrocatalysis determined by foot-of-the-wave analysis performed on cyclic voltammetry data as a function of CO_2 concentration (i.e. with increasing pressure). The red line is a nonlinear regression of the data, modeled by Michaelis-Menten kinetic model. Error bars are calculated from the error of a linear fit applied to replicate experiments at multiple scan rates.	127
5.7	Scan rate dependence of 0.2 mM $\text{Re}(\text{CO})_3(\text{bpy})\text{Cl}$ at 0.17 MPa. Working electrode was the basal plane of highly-oriented pyrolytic graphite (HOPG, 0.09 cm ²). 0.4 M concentration of TBAPF_6 prior to expansion. (Green:50 mV/s, Red:100 mV/s, Blue:150 mV/s, Purple: 200 mV/s, Orange: 250 mV/s, Black: 300mV/s	129
5.8	Scan rate dependence of 0.2 mM $\text{Re}(\text{CO})_3(\text{bpy})\text{Cl}$ at 2.46 MPa CO_2 . Working electrode was the basal plane of highly-oriented pyrolytic graphite (HOPG, 0.09 cm ²). 0.4 M concentration of TBAPF_6 prior to expansion. (Green:50 mV/s, Red:100 mV/s, Blue:150 mV/s, Purple: 200 mV/s, Orange: 250 mV/s, Black: 300mV/s	130

5.9	Scan rate dependence of 0.2 mM $\text{Re}(\text{CO})_3(\text{bpy})\text{Cl}$ at 2.46 MPa CO_2 . Working electrode was the basal plane of highly-oriented pyrolytic graphite (HOPG, 0.09 cm ²). 0.4 M concentration of TBAPF_6 prior to expansion. (Green:50 mV/s, Red:100 mV/s, Blue:150 mV/s, Purple: 200 mV/s, Orange: 250 mV/s, Black: 300mV/s	131
6.1	Electrodes after a chronoamperometry experiment using the current reactor. This shows the oxidation product buildup on the counter electrode	139
6.2	Schematic of an experimental electrocarboxylation setup utilizing a sacrificial anode	140

List of Tables

1.1	Thermodynamic reaction potentials for common electrochemical reduction reactions ²	3
1.2	Reduction Products of Planar Metal electrodes in Organic and Aqueous Solvents ³	4
2.1	Reproducibility results showing the faradic efficiency of CO ₂ reduction on In ⁰ -In ₂ O ₃ composite structure.	37
4.1	Detailed mechanism for the electrochemical reduction of CO ₂ on Au.	101
4.2	Input and regressed parameters for the COMSOL model.	103
5.1	Product Characterization Data for Re(CO) ₃ (bpy)Cl	125

Chapter 1

Overview and Introduction

1.1 The Problem of CO₂

One of the greatest challenges facing the scientific community and the world as a whole is the specter of anthropocentric global warming. The major cause for global warming is an increase in carbon dioxide (CO₂) concentrations in the atmosphere as shown in Figure 1.1. There have been many proposed solutions to address this increase but as yet the problem is still unsolved. A logical place to start building a sustainable carbon economy is the capture of CO₂ at large point sources such as power plants due to the low atmospheric concentrations of CO₂⁴. The technology to do this exists and is

operational in several places, however, the most widespread use of the captured CO₂ is in enhanced oil recovery (EOR).⁵ This practice, in theory, does have the benefit of sequestering the CO₂ away from the atmosphere. However, there are questions as to the long term ability of the rock formations to keep the CO₂ from leaking into the atmosphere in addition to the fact that the entire point of EOR is to get more fuels that will be burned to generate more carbon.⁶ With EOR clearly not

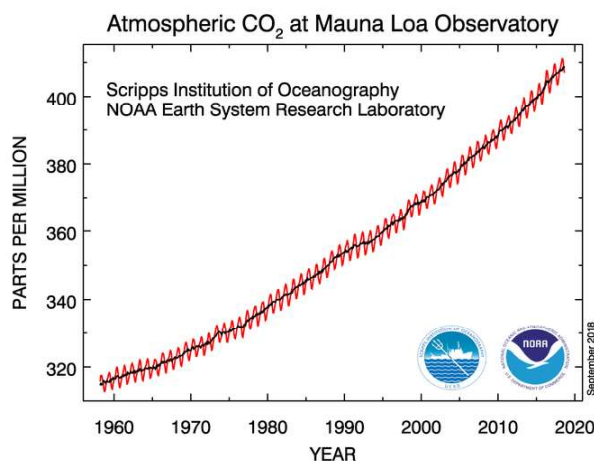


Figure 1.1. Chronological growth of atmospheric CO₂ concentration (red line) and seasonally corrected concentration of CO₂ (black line) measured at the Mauna Loa Observatory.¹

as carbon friendly as could be hoped, an alternative is needed. Utilizing this undesirable waste CO_2 to synthesize value added organic compounds is an elegant way to use the captured CO_2 . One method to do this that has attracted considerable interest is electrocatalysis. The rapid development of carbon-free renewable electricity generation such as wind and solar raises the promise that electrocatalysis may be a viable way to utilize the rising amounts of excess CO_2 in the atmosphere. Electrocatalysis in general, and electrochemical reduction in particular, is attractive because it can be readily powered by carbon free energy sources and is typically carried out at near ambient temperatures.

Unfortunately, the large scale industrial adoption of electrochemical reduction of CO_2 has some major problems which thus far have stymied any adoption.⁷ The main obstacles to adoption are:

1. Low catalyst activity
2. Low product selectivity
3. Insufficient catalyst stability
4. Insufficient fundamental understanding
5. Non-optimized reactor and system design.

This dissertation details efforts to overcome several of these fundamental problems.

1.2 Electrochemical Reduction of CO_2

The electrochemical reduction of CO_2 is accomplished by applying a voltage to a system to add electrons to the CO_2 . An important constraint upon electrochemistry in general is that it must occur in a conductive medium with at least two electrodes, each with its own redox reaction. To simplify the electrocatalytic systems, generally most research efforts have neglected either the oxidation or the reduction reaction, except to separate the cathode and anode with a membrane to prevent the decomposition of the reaction products at the unstudied electrode. The efficiency of various systems are measured using faradaic efficiency, which is the ratio of actual product formed to theoretical product possible based on charge passed through the system. A wide variety of catalysts, including both homogeneous and heterogeneous, have been explored for CO_2 electrochemical

Table 1.1. Thermodynamic reaction potentials for common electrochemical reduction reactions²

$\text{CO}_2(aq) + e^- \rightleftharpoons \text{CO}_2^{\cdot-}(aq)$	$E^0 = -1.90V$
$\text{CO}_2 + 2H^+ + 2e^- \rightleftharpoons \text{HCOOH}$	$E^0 = +0.85V$
$\text{CO}_2 + 2H^+ + 2e^- \rightleftharpoons \text{CO} + \text{H}_2\text{O}$	$E^0 = -0.76V$
$\text{CO}_2 + 4H^+ + 4e^- \rightleftharpoons \text{HCHO} + \text{H}_2\text{O}$	$E^0 = -0.72V$
$\text{CO}_2 + 6H^+ + 6e^- \rightleftharpoons \text{CH}_3\text{OH} + \text{H}_2\text{O}$	$E^0 = -0.62V$
$\text{CO}_2 + 8H^+ + 8e^- \rightleftharpoons \text{CH}_4 + 2\text{H}_2\text{O}$	$E^0 = -0.48V$

reduction. Catalysts are necessary for the reduction of CO_2 due to the energy intensive addition of the first electron transfer as shown in Table 1.1 where the initial reduction step from CO_2 to $\text{CO}_2^{\cdot-}$ has a much more negative potential than any of the final products. The reason for this high energy requirement is that the electron must go into a π^* orbital, necessitating a rearrangement of the molecule from linear to bent.

CO_2 reduction has been explored in both aqueous and organic systems. In aqueous systems, the water oxidation reaction provides a cheap and easy source of protons. Unfortunately aqueous solutions also allow hydrogen production as a side reaction. This decreases the efficiency of the process. In addition the solubility of CO_2 in aqueous systems, even under elevated pressure, is low and so is inadequate to sustain high current densities. Nonaqueous systems offer remedies to the hydrogen production and CO_2 solubility issues, however, they do not have a ready proton source. The absence of an easy oxidation reaction leads to the oxidation of the solvent, which means an expensive process.

1.2.1 Heterogeneous Catalytic Reduction of CO_2

There have been many types of catalysts explored for heterogeneous electrochemical reduction of CO_2 . Some of the most common are the transition metals. There has been considerable effort to determine which metal is the gives optimal results for both reaction rate and selectivity. Complicating the picture is that some catalysts change product selectivity in aqueous vs. organic media. The extensive work both done and categorized by Hori,³ to determine the typical products for both types of systems is shown in Table 1.2.

The most commonly produced reaction products (CO , HCOO^- , C_2O_4) have well accepted reac-

Table 1.2. Reduction Products of Planar Metal electrodes in Organic and Aqueous Solvents³

r

Organic			Aqueous		
Oxalate	Oxalate and CO	CO	HCCO ⁻	CO	HCCO ⁻ and CO
Pb	Fe	Cu	Pb	Au	Zr
Hg	Cr	Sn	Hg	Ag	Cr
Tl	Mo	Ag	Tl	Zn	Fe
Pt	Pd	Zn	In	Pd	Co
Ni	Cd	In	Sn	Ga	Ni
	Ti	Au	Cd	Ni-Cd	Rh
	Nb		Bi	W	Ir
	Stainless Steel				Pt

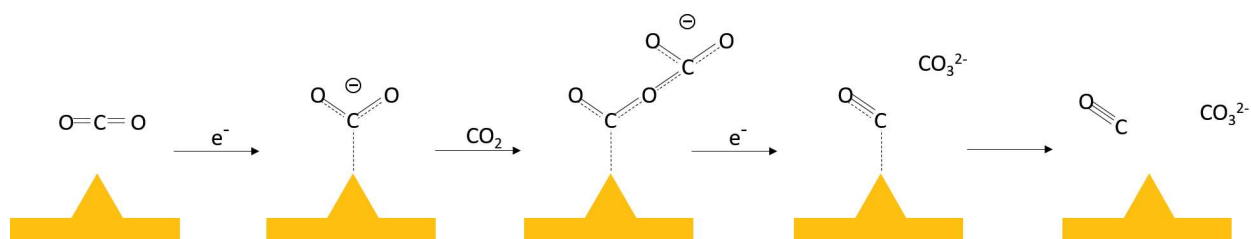


Figure 1.2. Aprotic adsorbed mechanism for CO₂ reduction

tion mechanisms. These mechanisms can be broken down by categories, protic or aprotic solvents and adsorbed or desorbed reaction mechanism. These mechanisms are detailed in Figures 1.2 - 1.5.

Prior research in electrocatalytic transition metals used in this work

Indium

Indium (In) typically is known to reduce CO₂ to formate in aqueous media, but CO in non-aqueous media.^{3,8} In is also known as one of the worst catalysts for water splitting.⁹ In aqueous

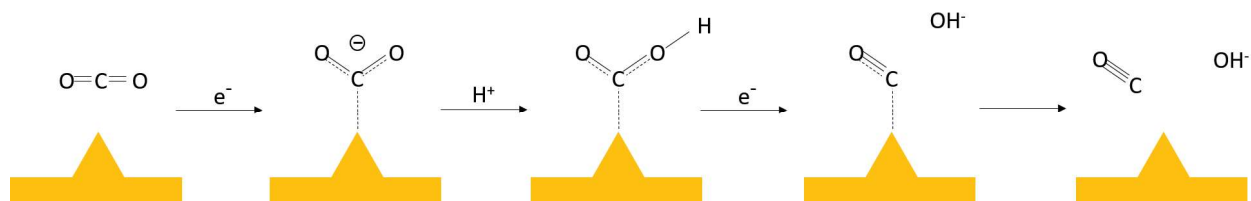


Figure 1.3. Protic adsorbed mechanism for CO₂ reduction

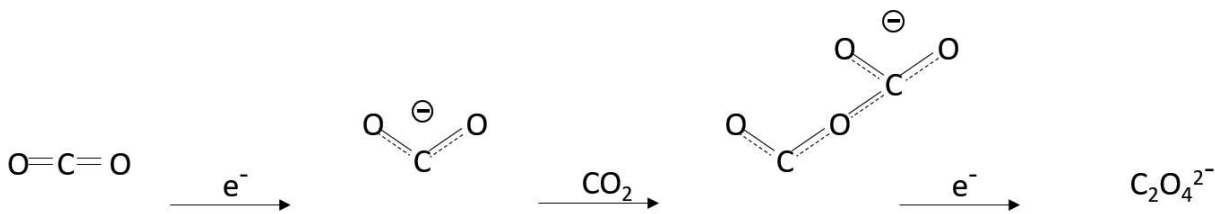


Figure 1.4. Aprotic nonadsorbed mechanism for CO_2 reduction

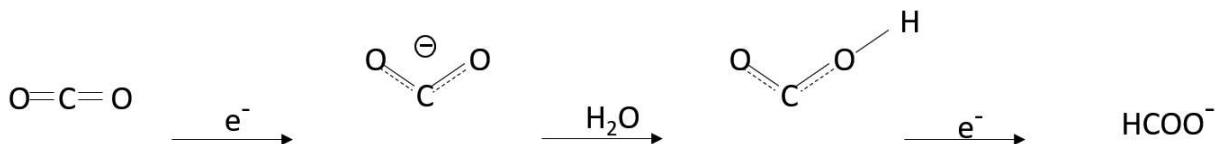


Figure 1.5. Protic nonadsorbed mechanism for CO_2 reduction

reaction media parasitic hydrogen evolution is one of the largest inefficiencies in reducing CO_2 , thus the inability of In to reduce water makes it a promising catalyst for CO_2 reduction. Initial studies found that bulk In was found to produce 95% formate at -1.55V vs SHE.^{3,8} Since these studies the focus has been upon improving the catalyst by nanostructuring and alloying. Ding et al report electrodepositing In nanocrystals for the conversion of CO_2 to CO.¹⁰ Interestingly it was found that the conversion rate was higher with an ionic liquid (BMIMPF_6) supporting electrolyte in acetonitrile than with the more typical TBAPF_6 salt. This was attributed to the formation of a $\text{BMIMPF}_6\backslash\text{CO}_2$ complex which activates the CO_2 . The possible increase in CO_2 concentration in solution due to the ionic liquid acting as a cosolvent was not investigated. Detweiler et al investigated the effects of the oxidation state of In upon the electrochemical reduction of CO_2 to formate.¹¹ It was found that CO_2 in solution acts to prevent the reduction of the In oxide layer. There has also been considerable interest in alloying In with copper in various ways. Hoffman et al electrodeposited dendritic copper-indium alloys of various compositions.¹² It was found that the composition of the alloy affected the product distribution and that it was possible to tune the products to an optimal syngas composition while producing formate as well. Core\Shell nanoparticles have also been used to make syngas.¹³ In this report it was found that by varying the shell thickness it was possible to tune the syngas composition. Rasul et al worked with a simultaneously reduced copper oxide surface and electrodeposited In metal.¹⁴ It was found that the electrodeposition of In inhibits the formation of H_2 while keeping the CO production from Cu intact. It is hypothesized

that the In selectively decorates the edge sites on the Cu while leaving the corner sites open for CO₂ reduction. There has also been an effort to employ rapid screening for the creation of In alloys with various other metals than copper.¹⁵ It was found that some previously uninvestigated metals (Fe, Co, and Ni) were beneficial to the selectivity of CO evolution. It was also found that the composition for these mixed metal catalysts was more important than the crystal phase for the selectivity.

Indium, being a relatively low cost metal, is an excellent candidate to be a catalyst for electrochemical reduction of CO₂ because of its ability to tunably produce syngas. This tunability, however, is not well understood. A better understanding of what makes In change reduction products from CO to formate would enable rational design of future In catalysts.

Gold

Gold (Au) is known for its selectivity in reducing CO₂ to CO using the adsorbed reaction mechanism (Figures 1.2 and 1.3). The first investigations into its electroreductive properties were carried out by Hori in 1985.³ Unmodified polycrystalline Au can achieve up to 80% faradaic efficiency in aqueous 0.1 M KHCO₃.¹⁶ This selectivity, combined with the addition of hydrogen from water splitting, offers the possibility of creating a Fisher-Tropsch process to make hydrocarbons.

Modifying the Au surface has led to improvements in the activity and selectivity of Au. These efforts have focused on three main areas, surface engineering, morphology control and composition manipulation.¹⁷

Surface engineering is focused on improving catalytic activity through increasing surface area and catalytic active sites. Many techniques have been used to accomplish this. In-situ reduced Au oxide derived catalysts have shown great promise.¹⁸ The reduced surfaces show higher porosity, which leads to greater surface area and more exposed active sites. Another technique that has been investigated is sputtering. Varying sputtering conditions with Au was found to influence the surface geometry and area. These changes resulted in differing CO₂ reduction potentials.¹⁹ Another type of surface engineering that has been used on Au is plasma treatments, to create a structured surface. These surfaces were then investigated in different solvents in addition to comparing to the polycrystalline starting material. In this study, Tafel plots indicated that the rate determining step was the initial electron transfer to the CO₂ regardless of the solvent.²⁰ Grain boundary engineering has also been used which resulted on higher activity on catalysts

with higher grain boundary densities.²¹ Functionilization with monolayers of tethered ligands has also been pursued. Interestingly, it was possible to change the product distribution with these monolayers.^{22,23}

Another active area is using nanostructures to control morphology. These nanostructures work to increase catalysis in several ways including increasing surface area, exposing specific crystal facets,²⁴ increasing edge sites,²⁵⁻²⁷ and increasing reactant concentrations.²⁸

An interesting attempt to control selectivity is alloying and interfacing Au with other metals. Copper, being the only metal that regularly creates multicarbon reduction products is a natural choice to investigate. It was found that although the mechanism on copper is not yet understood, the product distribution can be tuned by varying the composition from pure copper to pure gold.^{29,30} Using ordered gold-copper nanoparticles it was found that compressively strained gold layers over copper exhibited higher activity of CO₂ reduction. Palladium alloys have also been investigated. For flat films, it was found that the palladium and the gold act synergistically to improve CO₂ reduction.³¹ Interestingly, for Au-Pd core-shell particles, in contrast to the improved performance in strained gold, a decrease in strain on the palladium coatings leads to improved CO₂ reduction.³² Experiments with cadmium alloys show that CO₂ reduction is decreased.³³ Alloying is not the only way to synergistically improve gold, the support can affect the catalysis as well. It has been shown that a graphite nanoribbon support for gold can improve performance.³⁴ In addition, placing gold on a cerium oxide support improves catalysis.³⁵

The use of gold for electrocatalysis is of course constrained by its high cost. However, if the current density could be increased, the excellent selectivity of gold in catalyzing the reduction of CO₂ to CO will make it an extremely competitive candidate for eventual industrial adoption in CO₂ electrochemical reduction processes.

Copper

Another metal that has attracted many research efforts is copper (Cu) as it is the only metal to commonly make multicarbon products.³⁶ This ability is very attractive due to the higher prices that that these can command over the more commonly produced single carbon products, CO and formic acid. Unfortunately Cu is non-selective, making many products.³⁷ Efforts to develop Cu electrodes have been wideranging. Bulk Cu has been investigated and found to produce a wide range of products³⁸, as well as changing product distribution at different potentials.³⁹ Electrodeposited

Cu has been used to create high surface area catalysts. The possible increase in current density due to the increased surface area is inhibited by diffusion into the pores.⁴⁰ Copper-porphyrins complexes, deposited onto a carbon support, have shown high current densities for ethylene and methane.^{41,42} Oxide-derived Cu has been used to drive selectivity towards C2 products. It was shown that a cesium electrolyte, combined with a modest roughness was optimal for the production of C2 products achieving up to 70% faradaic efficiency.⁴³ Attempting to overcome mass transport limitation Cu Gas Diffusion Electrodes (GDEs) have also been looked into. It was shown that increasing the pressure of CO₂ led to higher current densities.⁴²

The mechanism of CO₂ reduction on Cu is more complicated than on other transition metals. It is widely accepted that the reason that Cu creates hydrocarbon species is that it has an intermediate binding energy for CO.³⁶ The mechanism then becomes more debated with many influences. There has been work that shows that the crystal plane can affect potential dependent reduction.⁴⁴ Another reports shows that the edge sites are also important as well as confirming a dependence on the crystal plane.^{45,46} Another factor that has been identified as affecting selectivity is that the loading of the catalyst. Denser loadings enabled growth of nanostructures promoting C2 and C3 products over leaner loadings.⁴⁷ Local pH has also been implicated as affecting the electrocatalysis.⁴⁸

Overall, the optimal way to conduct electrochemical reduction of CO₂ on Cu is still unknown. Standing in the way of future development of Cu as an electrocatalysis is a need for a greater understanding of the mechanism of the electrochemical reduction of CO₂ on copper. In addition, a method to increase the availability of CO₂ to the surface is imperative. With these obstacles overcome, the ability of Cu to create C2 products, combined with its cheap cost, will make Cu a very attractive potential catalyst for industrial adoption of CO₂ reduction.

1.2.2 Homogeneous Catalytic Reduction of CO₂

Homogeneous catalysis for the reduction of CO₂ has focused on reduced transition metal complexes. The most investigated catalysts typically use nickel, copper, palladium, cobalt, or rhenium metal centers.⁴⁹ The best characterized homogeneous catalyst utilizes rhenium.

Rhenium (Re) in CO₂ electrochemical reduction catalysts is typically used in tricarbonyl Re complexes. This type of complex was first investigated by Hawecker and coworkers in 1984 where they found that it could both photochemically and electrochemically reduce CO₂.⁵⁰ Subsequent

work with this complex ($\text{Re}(\text{CO})_3\text{bpyCl}$) as a homogeneous catalyst has focused on modifying the base complex in attempts to improve it. It has been found that the substituents on the 4,4' position of the bipyridine ligand affected the reduction potential of the overall complex.⁵¹ The order of the change is $\text{OCH}_3 < \text{C}(\text{CH}_3)_3 < \text{CH}_3 < \text{H} < \text{COOH}$. Catalysts in this family have also been immobilized onto electrodes to create heterogeneous electrodes.⁵²

In addition to the modifications to the catalyst itself, there have been efforts to improve the catalytic system. One method investigated is to use this catalyst under high pressures of CO_2 for photocatalysis. Hori et al found that in an amine, increasing the pressure of CO_2 increased the photoreduction of CO_2 until a limiting plateau.^{53,54} It has also been found that the addition of Bronsted acids enhances the catalysis.⁵⁵

The mechanism for homogeneous reduction by Re has also been investigated by both electrochemical and spectroscopic means.^{51,56-60} The mechanism for $\text{Re}(\text{CO})_3\text{bpyCl}$ is proposed to be an initial electron transfer to the Re complex, followed by the loss of the chloride ion. A subsequent electron transfer leads to a negatively charged complex which attacks the CO_2 . Proton transfers then create CO and H_2O and the complex is reset for further catalysis.

The adoption of these Re catalysts for industrial use is hampered by cost, difficulty in separations, and the low current densities due to diffusion of available CO_2 to the catalyst. Homogeneous Re catalysts are excellent model systems to investigate the effects of other parameters due to the extensive characterization that they have received.

1.3 Gas Expanded Liquids

Gas Expanded Liquids (GXLs) are a relatively new type of solvent, fitting between ordinary solvents and supercritical fluids while offering advantages in some cases over both. A GXL is a mixed solvent composed of a compressible gas and a liquid solvent. Under pressure the solubility of the gas in the liquid solvent is high enough that the liquid volume of the solvent increases by a significant amount. The formation of a GXL is highly dependent on the base solvent, of which there are three classes⁶¹. Class I solvents, such as water, do not form GXLs in any appreciable degree due to their limited ability to dissolve CO_2 . Class II solvents such as methanol, acetonitrile and most other organic solvents solvate large amounts of gas and have large changes to their physical

properties. Class III solvents include crude oil and ionic liquids solvate smaller amounts of the compressible gas and thus have smaller changes in their solvent properties.

1.3.1 Gas Expanded Liquids for Conventional Catalysis

GXLs have been used to tune the product distribution for catalytic reactions. In one report on the nickel catalyzed carbonylation of alkenes and acetylenes with allyl bromides, it was shown that the product distribution could be tuned utilizing CO₂ expanded acetone.⁶² At lower pressures of CO₂, cyclopentanone is the major product, while at high pressures, the acyclic product is favored. Another carbonylation reaction reported to be improved by utilizing GXLs is the Pd catalyzed carbonylation of primary amines to ureas.⁶³ In this reaction, a biphasic system consists of an expanded amine liquid phase and a CO₂ air pressurized gas phase. This system is believed to promote the formation of the carbamate in addition to increasing the turnover number for the catalyst. In addition, the use of the GXL is believed to suppress the oxidation of the catalyst.

There have also been hydroformulations carried out in GXLs particularly in ionic liquids.⁶⁴ The rationale behind the use of ionic liquids is that ionic liquids have good solubility for CO₂. They do not have dramatic expansion as seen in acetonitrile, methanol etc., however they will solvate large amounts of CO₂ and moderately expand. At the same time, these expanded ionic liquids will be insoluble in supercritical CO₂. Retaining the catalyst in the ionic liquid enables easy partition of the products into the supercritical CO₂.⁶⁵

1.3.2 Gas Expanded Liquids for Electrocatalysis:

There previously have been no reports of electrochemical reduction in GXLs prior to the work in this dissertation. This neglect has been unfortunate for electrocatalysis because it has been shown that gas expanded liquids (GXLs) can increase the diffusivities of various species in assorted solvents by an order of magnitude over the neat solvent.⁶⁶ In addition it is possible to achieve much higher concentrations of CO₂ (15 M) than in traditional aqueous solvents (0.036 M) at 25°C. This increase in concentration will have a large impact on the rate of electrocatalysis. This can be seen by inspection of the Butler-Volmer equation that governs electrochemical reactions. The current is directly proportional to [Ox], the concentration of oxidized species in the bulk, while we assume the amount of [Red] is negligible in the bulk.

$$i = nFAk_0 \left\{ [Ox] \exp\left(-\frac{\alpha nF}{RT}(E - E_0)\right) - [Red] \exp\left(\frac{(1 - \alpha)nF}{RT}(E - E_0)\right) \right\} \quad (1.1)$$

Eqn. 1.1 Butler-Volmer Equation for electrochemical kinetics where E_0 (in V) is the standard potential of the redox reaction, E (in V) is the applied potential, R is the gas constant (8.314 JK mol), F is the Faraday constant (96485 C/mol), T (in K) is the temperature, n is the number of electrons transferred, k is the standard heterogeneous rate constant (in ms), and α is the transfer coefficient

Although electrochemical reduction has not been done in GXLs, two reports on electrocarboxylation, both carboxylating halides, have utilized high pressures of CO_2 in liquids that will expand although the expansion effect is not taken into account explicitly. Tateno et al reports that the current efficiency in an ionic liquid increases from 32 percent at atmospheric CO_2 to 60 percent at 10 MPa on a Pt working electrode.⁶⁷ Chanfreau et al reports that for electrocarboxylation of benzyl chloride in supercritical CO_2 and in DMF that there existed an optimum pressure for selectivity at 6 MPa with experiments conducted at 1,6,7 and 8 MPa.⁶⁸ DMF has been found to exhibit expansion behavior under this pressure regime.⁶¹ This report on using a GXL for electrochemistry neglects all pressures between 1 and 6 MPa.

Unfortunately the benefits of using GXLs for electrocatalysis also come with downsides. The first and most obvious is that GXLs require equipment that can handle the pressures necessary to create them. The pressure presents safety and experiment design challenges. From a chemical standpoint, the changing polarity can affect the ability of a supporting electrolyte to remain in solution, as well as possibly changing the catalytic effects. Despite these downsides, the use of GXLs for electrochemical reduction is promising.

1.4 Goals of Dissertation

Throughout this dissertation I will show efforts to address the fundamental problems for the electrochemical reduction of CO_2 . This work will directly address three of the five fundamental problems identified by Qiao et al.⁷ as well as outlining future approaches to address the remaining two through work based on the use of Gas eXpanded Electrolytes. Through addressing every fundamental problem identified, the work in this dissertation will advance the field of electrocatalytic CO_2 reduction toward industrial relevance.

In Chapter 2, Selective Electrochemical CO₂ Reduction to CO Using In-Situ Reduced In₂O₃ Nanocatalysts, I will address Problem 2, low product selectivity. I will show the successful efforts to create and characterize a selective oxide-derived In catalyst for CO₂ reduction to CO in aqueous media. This characterization was carried out through the use of Scanning Electrochemical Microscopy, which enabled facile, potential dependent, collection of products.

In Chapter 3, Enhanced Electrocatalytic CO₂ Conversion in Pressure-Tunable CO₂-Expanded Electrolytes, I will pivot focus from catalysts to catalytic systems. I will show the successful efforts to create a new reaction media, Gas eXpanded Electrolytes. The concept behind this effort is to increase the availability of CO₂ to the surface of the electrode through the ability of GXEs to solvate massive amounts of CO₂. The hypothesized result of greater CO₂ availability to the electrode is that the catalytic rate will increase. These efforts have succeeded and resulted in both an order of magnitude improvement in catalyst activity (Problem 1: Low catalyst activity) while retaining and even slightly improving catalytic selectivity (Problem 2: Low product selectivity) To accomplish this, an understanding of the vapor-liquid equilibrium and the diffusion characteristics was developed. Then the electrocatalytic activity of polycrystalline gold was characterized over a wide pressure range. The subsequent finding of an order of magnitude increase in the current density abundantly addresses the fundamental problem of low catalyst activity.

In Chapter 4, Insights Into the Pressure Dependent Reaction Rates for Electrochemical Reduction of CO₂ in CO₂ Expanded Electrolytes, I will address Problem 4, insufficient fundamental understanding of electrochemical reduction. In Chapter 3 a puzzling decrease in the current density was observed at the highest degrees of expansion of the Gas eXpanded Electrolyte. Through the use of COMSOL modeling, the kinetic rate constants for the fundamental reaction steps were extracted from cyclic voltammograms at various degrees of expansion. It was found that a decrease in the first electron transfer step becomes rate limiting at high degrees of expansion.

In Chapter 5, Insights Into the Kinetics of Re(CO)₃(bpy)Cl For the Electrochemical Reduction of CO₂ in CO₂ Expanded Electrolytes, I will again address Problem 4, this time for homogeneous electrocatalysts. Building upon the success in the use of Gas eXpanded Electrolytes for electrochemical reduction of CO₂ with a heterogeneous gold catalyst, a homogeneous catalyst, Re(CO)₃(bpy)Cl, was investigated. By using Foot of the Wave Analysis to extract an observed rate of reaction, combined with the ability of Gas eXpanded Electrolytes to tune the concentra-

tion of CO₂, Michaelis-Menten kinetics were observed. In this chapter, in addition to Chapter 4, shows how the ability of Gas eXpanded Electrolytes to tune the concentration of CO₂ enhances the understanding of the fundamentals of electrochemical reduction.

In Chapter 6, Conclusions and Future Work, I will provide an overview of the most important findings from this work. In addition, I will provide a roadmap of how to use Gas eXpanded Electrolytes to address the remaining two problems, insufficient catalyst stability and non-optimized reactor and system design.

References

- [1] ESRL Global Monitoring Division - Global Greenhouse Gas Reference Network. 2005.
- [2] Schneider, J., Jia, H., Muckerman, J. T., and Fujita, E. (2012) Thermodynamics and kinetics of CO₂, CO, and H⁺ binding to the metal centre of CO₂ reduction catalysts. *Chemical Society Reviews* 41, 2036–2051.
- [3] Hori, Y. i. *Modern aspects of electrochemistry*; Springer, 2008; pp 89–189.
- [4] Chen, Y., Lewis, N. S., and Xiang, C. (2015) Operational constraints and strategies for systems to effect the sustainable, solar-driven reduction of atmospheric CO₂. *Energy Environ. Sci.* 8, 3663–3674.
- [5] Leung, D. Y., Caramanna, G., and Maroto-Valer, M. M. (2014) An overview of current status of carbon dioxide capture and storage technologies. *Renewable and Sustainable Energy Reviews* 39, 426 – 443.
- [6] Zoback, M. D., and Gorelick, S. M. (2012) Earthquake triggering and large-scale geologic storage of carbon dioxide. *Proceedings of the National Academy of Sciences* 109, 10164–10168.
- [7] Qiao, J., Liu, Y., Hong, F., and Zhang, J. (2014) A review of catalysts for the electroreduction of carbon dioxide to produce low-carbon fuels. *Chemical Society Reviews* 43, 631–675.
- [8] Kapusta, S., and Hackerman, N. (1983) The electroreduction of carbon dioxide and formic acid on tin and indium electrodes. *Journal of The Electrochemical Society* 130, 607–613.
- [9] Leonard, K. C., and Bard, A. J. (2013) Pattern recognition correlating materials properties of the elements to their kinetics for the hydrogen evolution reaction. *Journal of the American Chemical Society* 135, 15885–15889.

- [10] Ding, C., Li, A., Lu, S.-M., Zhang, H., and Li, C. (2016) In Situ Electrodeposited Indium Nanocrystals for Efficient CO₂ Reduction to CO with Low Overpotential. *ACS Catalysis* 6, 6438–6443.
- [11] Detweiler, Z. M., White, J. L., Bernasek, S. L., and Bocarsly, A. B. (2014) Anodized indium metal electrodes for enhanced carbon dioxide reduction in aqueous electrolyte. *Langmuir* 30, 7593–7600.
- [12] Hoffman, Z. B., Gray, T. S., Moraveck, K. B., Gunnoe, T. B., and Zangari, G. (2017) Electrochemical reduction of carbon dioxide to syngas and formate at dendritic copper–indium electrocatalysts. *ACS Catalysis* 7, 5381–5390.
- [13] Xie, H., Chen, S., Ma, F., Liang, J., Miao, Z., Wang, T., Wang, H.-L., Huang, Y., and Li, Q. (2018) Boosting Tunable Syngas Formation via Electrochemical CO₂ Reduction on Cu/In₂O₃ Core/Shell Nanoparticles. *ACS applied materials & interfaces* 10, 36996–37004.
- [14] Rasul, S., Anjum, D. H., Jedidi, A., Minenkov, Y., Cavallo, L., and Takanabe, K. (2015) A highly selective copper–indium bimetallic electrocatalyst for the electrochemical reduction of aqueous CO₂ to CO. *Angewandte Chemie International Edition* 54, 2146–2150.
- [15] He, J., Dettelbach, K. E., Salvatore, D. A., Li, T., and Berlinguette, C. P. (2017) High-Throughput Synthesis of Mixed-Metal Electrocatalysts for CO₂ Reduction. *Angewandte Chemie International Edition* 56, 6068–6072.
- [16] Noda, H., Ikeda, S., Oda, Y., Imai, K., Maeda, M., and Ito, K. (1990) Electrochemical reduction of carbon dioxide at various metal electrodes in aqueous potassium hydrogen carbonate solution. *Bulletin of the Chemical Society of Japan* 63, 2459–2462.
- [17] Zhao, S., Jin, R., and Jin, R. (2018) Opportunities and Challenges in CO₂ Reduction by Gold- and Silver-Based Electrocatalysts: From Bulk Metals to Nanoparticles and Atomically Precise Nanoclusters. *ACS Energy Letters* 3, 452–462.
- [18] Chen, Y., Li, C. W., and Kanan, M. W. (2012) Aqueous CO₂ Reduction at Very Low Overpotential on Oxide-Derived Au Nanoparticles. *Journal of the American Chemical Society* 134, 19969–19972, PMID: 23171134.

- [19] Ohmori, T., Nakayama, A., Mametsuka, H., and Suzuki, E. (2001) Influence of sputtering parameters on electrochemical CO₂ reduction in sputtered Au electrode. *Journal of Electroanalytical Chemistry* 514, 51–55.
- [20] Koh, J. H., Jeon, H. S., Jee, M. S., Nursanto, E. B., Lee, H., Hwang, Y. J., and Min, B. K. (2014) Oxygen plasma induced hierarchically structured gold electrocatalyst for selective reduction of carbon dioxide to carbon monoxide. *The Journal of Physical Chemistry C* 119, 883–889.
- [21] Feng, X., Jiang, K., Fan, S., and Kanan, M. W. (2015) Grain-boundary-dependent CO₂ electroreduction activity. *Journal of the American Chemical Society* 137, 4606–4609.
- [22] others., et al. (2016) A molecular surface functionalization approach to tuning nanoparticle electrocatalysts for carbon dioxide reduction. *Journal of the American Chemical Society* 138, 8120–8125.
- [23] Fang, Y., and Flake, J. C. (2017) Electrochemical reduction of CO₂ at functionalized Au electrodes. *Journal of the American Chemical Society* 139, 3399–3405.
- [24] Lee, H.-E., Yang, K. D., Yoon, S. M., Ahn, H.-Y., Lee, Y. Y., Chang, H., Jeong, D. H., Lee, Y.-S., Kim, M. Y., and Nam, K. T. (2015) Concave rhombic dodecahedral Au nanocatalyst with multiple high-index facets for CO₂ reduction. *ACS nano* 9, 8384–8393.
- [25] Mistry, H., Reske, R., Zeng, Z., Zhao, Z.-J., Greeley, J., Strasser, P., and Cuenya, B. R. (2014) Exceptional size-dependent activity enhancement in the electroreduction of CO₂ over Au nanoparticles. *Journal of the American Chemical Society* 136, 16473–16476.
- [26] Mostafa, S., Behafarid, F., Croy, J. R., Ono, L. K., Li, L., Yang, J. C., Frenkel, A. I., and Cuenya, B. R. (2010) Shape-dependent catalytic properties of Pt nanoparticles. *Journal of the american chemical society* 132, 15714–15719.
- [27] Zhu, W., Zhang, Y.-J., Zhang, H., Lv, H., Li, Q., Michalsky, R., Peterson, A. A., and Sun, S. (2014) Active and selective conversion of CO₂ to CO on ultrathin Au nanowires. *Journal of the American Chemical Society* 136, 16132–16135.

- [28] others., et al. (2016) Enhanced electrocatalytic CO₂ reduction via field-induced reagent concentration. *Nature* 537, 382.
- [29] Kim, D., Resasco, J., Yu, Y., Asiri, A. M., and Yang, P. (2014) Synergistic geometric and electronic effects for electrochemical reduction of carbon dioxide using gold–copper bimetallic nanoparticles. *Nature communications* 5, 4948.
- [30] Xu, Z., Lai, E., Shao-Horn, Y., and Hamad-Schifferli, K. (2012) Compositional dependence of the stability of AuCu alloy nanoparticles. *Chemical Communications* 48, 5626–5628.
- [31] others., et al. (2015) Synthesis of thin film AuPd alloys and their investigation for electrocatalytic CO₂ reduction. *Journal of Materials Chemistry A* 3, 20185–20194.
- [32] Plana, D., Flórez-Montano, J., Celorrio, V., Pastor, E., and Fermín, D. J. (2013) Tuning CO₂ electroreduction efficiency at Pd shells on Au nanocores. *Chemical Communications* 49, 10962–10964.
- [33] Jovanov, Z. P., Hansen, H. A., Varela, A. S., Malacrida, P., Peterson, A. A., Nørskov, J. K., Stephens, I. E., and Chorkendorff, I. (2016) Opportunities and challenges in the electrocatalysis of CO₂ and CO reduction using bifunctional surfaces: A theoretical and experimental study of Au–Cd alloys. *Journal of Catalysis* 343, 215–231.
- [34] Rogers, C., Perkins, W. S., Veber, G., Williams, T. E., Cloke, R. R., and Fischer, F. R. (2017) Synergistic enhancement of electrocatalytic CO₂ reduction with gold nanoparticles embedded in functional graphene nanoribbon composite electrodes. *Journal of the American Chemical Society* 139, 4052–4061.
- [35] others., et al. (2017) Enhancing CO₂ electroreduction with the metal–oxide interface. *Journal of the American Chemical Society* 139, 5652–5655.
- [36] Raciti, D., and Wang, C. (2018) Recent advances in CO₂ reduction electrocatalysis on copper. *ACS Energy Letters* 3, 1545–1556.
- [37] Kuhl, K. P., Cave, E. R., Abram, D. N., and Jaramillo, T. F. (2012) New insights into the electrochemical reduction of carbon dioxide on metallic copper surfaces. *Energy & Environmental Science* 5, 7050–7059.

- [38] Kuhl, K. P., Cave, E. R., Abram, D. N., and Jaramillo, T. F. (2012) New insights into the electrochemical reduction of carbon dioxide on metallic copper surfaces. *Energy and Environmental Science* 5, 7050–7059.
- [39] Kuhl, K. P., Hatsukade, T., Cave, E. R., Abram, D. N., Kibsgaard, J., and Jaramillo, T. F. (2014) Electrocatalytic conversion of carbon dioxide to methane and methanol on transition metal surfaces. *Journal of the American Chemical Society* 136, 14107–14113.
- [40] Hoang, T. T., Ma, S., Gold, J. I., Kenis, P. J., and Gewirth, A. A. (2017) Nanoporous copper films by additive-controlled electrodeposition: CO₂ reduction catalysis. *ACS Catalysis* 7, 3313–3321.
- [41] Weng, Z., Jiang, J., Wu, Y., Wu, Z., Guo, X., Materna, K. L., Liu, W., Batista, V. S., Brudvig, G. W., and Wang, H. (2016) Electrochemical CO₂ reduction to hydrocarbons on a heterogeneous molecular Cu catalyst in aqueous solution. *Journal of the American Chemical Society* 138, 8076–8079.
- [42] Sonoyama, N., Kirii, M., and Sakata, T. (1999) Electrochemical reduction of CO₂ at metal-porphyrin supported gas diffusion electrodes under high pressure CO₂. *Electrochemistry communications* 1, 213–216.
- [43] Lum, Y., Yue, B., Lobaccaro, P., Bell, A. T., and Ager, J. W. (2017) Optimizing C–C coupling on Oxide-Derived copper catalysts for electrochemical CO₂ reduction. *The Journal of Physical Chemistry C* 121, 14191–14203.
- [44] Hahn, C., Hatsukade, T., Kim, Y.-G., Vailionis, A., Baricuatro, J. H., Higgins, D. C., Niotopi, S. A., Soriaga, M. P., and Jaramillo, T. F. (2017) Engineering Cu surfaces for the electrocatalytic conversion of CO₂: Controlling selectivity toward oxygenates and hydrocarbons. *Proceedings of the National Academy of Sciences* 114, 5918–5923.
- [45] Loiudice, A., Lobaccaro, P., Kamali, E. A., Thao, T., Huang, B. H., Ager, J. W., and Buon-santi, R. (2016) Tailoring Copper Nanocrystals towards C₂ Products in Electrochemical CO₂ Reduction. *Angewandte Chemie - International Edition* 55, 5789–5792.

- [46] Tang, W., Peterson, A. A., Varela, A. S., Jovanov, Z. P., Bech, L., Durand, W. J., Dahl, S., Nørskov, J. K., and Chorkendorff, I. (2012) The importance of surface morphology in controlling the selectivity of polycrystalline copper for CO₂ electroreduction. *Physical Chemistry Chemical Physics* 14, 76–81.
- [47] Kim, D., Kley, C. S., Li, Y., and Yang, P. (2017) Copper nanoparticle ensembles for selective electroreduction of CO₂ to C₂–C₃ products. *Proceedings of the National Academy of Sciences* 201711493.
- [48] Roberts, F. S., Kuhl, K. P., and Nilsson, A. (2015) High selectivity for ethylene from carbon dioxide reduction over copper nanocube electrocatalysts. *Angewandte Chemie International Edition* 54, 5179–5182.
- [49] Finn, C., Schnittger, S., Yellowlees, L. J., and Love, J. B. (2012) Molecular approaches to the electrochemical reduction of carbon dioxide. *Chemical Communications* 48, 1392–1399.
- [50] Hawecker, J., Lehn, J.-M., and Ziessel, R. (1984) Electrocatalytic reduction of carbon dioxide mediated by Re (bipy)(CO)₃Cl (bipy= 2, 2'-bipyridine). *Journal of the Chemical Society, Chemical Communications* 328–330.
- [51] Smieja, J. M., and Kubiak, C. P. (2010) Re (bipy-tBu)(CO)₃Cl- improved catalytic activity for reduction of carbon dioxide: IR-spectroelectrochemical and mechanistic studies. *Inorganic chemistry* 49, 9283–9289.
- [52] Cosnier, S., Deronzier, A., and Moutet, J.-C. (1988) Electrocatalytic reduction of CO₂ on electrodes modified by fac-Re (2, 2'-bipyridine)(CO)₃Cl complexes bonded to polypyrrole films. *Journal of molecular catalysis* 45, 381–391.
- [53] Hori, H., Koike, K., Suzuki, Y., Ishizuka, M., Tanaka, J., Takeuchi, K., and Sasaki, Y. (2002) High-pressure photocatalytic reduction of carbon dioxide using [fac-Re (bpy)(CO)₃P (OiPr)₃]+(bpy= 2, 2'-bipyridine). *Journal of Molecular Catalysis A: Chemical* 179, 1–9.
- [54] Hori, H., Takano, Y., Koike, K., and Sasaki, Y. (2003) Efficient rhenium-catalyzed photochemical carbon dioxide reduction under high pressure. *Inorganic Chemistry Communications* 6, 300–303.

- [55] Wong, K.-Y., Chung, W.-H., and Lau, C.-P. (1998) The effect of weak Brönsted acids on the electrocatalytic reduction of carbon dioxide by a rhenium tricarbonyl bipyridyl complex. *Journal of electroanalytical chemistry* 453, 161–170.
- [56] Sullivan, B. P., Bolinger, C. M., Conrad, D., Vining, W. J., and Meyer, T. J. (1985) One- and two-electron pathways in the electrocatalytic reduction of CO₂ by fac-Re (bpy)(CO)₃Cl (bpy= 2, 2'-bipyridine). *Journal of the Chemical Society, Chemical Communications* 1414–1416.
- [57] Stor, G., Hartl, F., Van Outersterp, J., and Stufkens, D. (1995) Spectroelectrochemical (IR, UV/Vis) Determination of the Reduction Pathways for a Series of [Re (CO)₃ (. alpha.-diimine) L']^{0/+}(L'= Halide, Otf-, THF, MeCN, n-PrCN, PPh₃, P (OMe)₃) Complexes. *Organometallics* 14, 1115–1131.
- [58] Johnson, F. P., George, M. W., Hartl, F., and Turner, J. J. (1996) Electrocatalytic Reduction of CO₂ Using the Complexes [Re (bpy)(CO)₃L]ⁿ (n=+ 1, L= P (OEt)₃, CH₃CN; n= 0, L= Cl-, Otf-; bpy= 2, 2'-Bipyridine; Otf= CF₃SO₃) as Catalyst Precursors: Infrared Spectroelectrochemical Investigation. *Organometallics* 15, 3374–3387.
- [59] Sampson, M. D., Froehlich, J. D., Smieja, J. M., Benson, E. E., Sharp, I. D., and Kubiak, C. P. (2013) Direct observation of the reduction of carbon dioxide by rhenium bipyridine catalysts. *Energy & Environmental Science* 6, 3748–3755.
- [60] Smieja, J. M., Benson, E. E., Kumar, B., Grice, K. A., Seu, C. S., Miller, A. J., Mayer, J. M., and Kubiak, C. P. (2012) Kinetic and structural studies, origins of selectivity, and interfacial charge transfer in the artificial photosynthesis of CO. *Proceedings of the National Academy of Sciences* 109, 15646–15650.
- [61] Jessop, P. G., and Subramaniam, B. (2007) Gas-Expanded Liquids. *Chemical Reviews* 107, 2666–2694, PMID: 17564482.
- [62] del Moral, D., Osuna, A. M. B., Cordoba, A., Moreto, J. M., Veciana, J., Ricart, S., and Ventosa, N. (2009) Versatile chemoselectivity in Ni-catalyzed multiple bond carbonylations and cyclocarbonylations in CO₂-expanded liquids. *Chemical Communications* 4723–4725.

- [63] Della Ca, N., Bottarelli, P., Dibenedetto, A., Aresta, M., Gabriele, B., Salerno, G., and Costa, M. (2011) Palladium-catalyzed synthesis of symmetrical urea derivatives by oxidative carbonylation of primary amines in carbon dioxide medium. *Journal of catalysis* 282, 120–127.
- [64] Jutz, F., Andanson, J.-M., and Baiker, A. (2010) Ionic liquids and dense carbon dioxide: a beneficial biphasic system for catalysis. *Chemical reviews* 111, 322–353.
- [65] Kunene, T. E., Webb, P. B., and Cole-Hamilton, D. J. (2011) Highly selective hydroformylation of long-chain alkenes in a supercritical fluid ionic liquid biphasic system. *Green Chemistry* 13, 1476–1481.
- [66] Akien, G. R., and Poliakoff, M. (2009) A critical look at reactions in class I and II gas-expanded liquids using CO₂ and other gases. *Green Chem.* 11, 1083–1100.
- [67] Tateno, H., Nakabayashi, K., Kashiwagi, T., Senboku, H., and Atobe, M. (2015) Electrochemical fixation of CO₂ to organohalides in room-temperature ionic liquids under supercritical CO₂. *Electrochimica Acta* 161, 212 – 218.
- [68] Chanfreau, S., Cognet, P., Camy, S., and Condoret, J.-S. (2008) Electrocarboxylation in supercritical CO₂ and CO₂-expanded liquids. *The Journal of Supercritical Fluids* 46, 156 – 162.

Chapter 2

Selective Electrochemical CO₂ Reduction to CO Using In-Situ Reduced In₂O₃ Nanocatalysts

Previously published in: Journal of Materials Chemistry A, Volume 5, Pages 22743–22749

2.1 Abstract

Both metallic indium and indium oxide electrocatalysts typically have high selectivity for producing formate via the electrochemical reduction of CO₂ in aqueous media. It has been suggested that under highly negative potentials, i.e. potentials typically sufficient to reduce indium oxide to In⁰, the native oxide layer on metallic indium or indium oxide particles is not reduced to In⁰ when exposed to CO₂-saturated electrolytes. This meta-stable oxide layer is crucial in the mechanism for producing formate via the two-electron, two-proton reduction of CO₂, however it prevents the catalysis from occurring on In⁰. Herein, we report that by electrochemically reducing In₂O₃ nanocatalysts in Ar-saturated electrolytes *in-situ*, prior to CO₂ exposure, will remove this metastable oxide layer and create a In⁰-In₂O₃ composite. This In⁰-In₂O₃ composite material changes the selectivity and is able to electrochemically reduce CO₂ to CO with near 100% selectivity at relatively low overpotentials (c.a. -1.0 V vs Ag/AgCl). We attribute the change in selectivity to the direct exposure of In⁰ to CO₂ in solution that typically does not exist to due to the native

oxide layer that forms on In metal. In addition, we observed that the first electron-transfer step to form the surface adsorbed intermediates is highly reversible on the $\text{In}^0\text{-In}_2\text{O}_3$ composite, however it is irreversible on an In foil electrode. We also report the utilization of Substrate Generation-Tip Collection Scanning Electrochemical Microscopy (SG-TC SECM) to measure the production of CO as function of applied potential. This technique allows for the collection of CO *in-situ* during the voltammetry experiment as it is produced on the catalytic electrode, which results in accurate potential dependent measurements of CO production.

2.2 Introduction

The efficient conversion of CO_2 feedstocks into value-added products is a grand challenge in sustainability science.¹⁻⁵ Since the reduction of CO_2 occurs through proton-coupled electron-transfer processes, electrocatalysts can electrochemically reduce CO_2 at room temperature because the energy needed to overcome the activation barrier can be delivered in the form of an electrical potential.⁶⁻¹¹ Converting CO_2 to CO with high selectivity is of great interest because it could potentially be combined with existing industrial processes (e.g. Fischer-Tropsch-type processes) to produce liquid fuels and chemicals from CO_2 feedstocks.¹²⁻¹⁴ However, achieving high selectivity for electrochemical CO_2 reduction is a major challenge in catalyst development. This is because numerous carbon products can be obtained (e.g. CO, formate, alcohols, etc.),¹⁵⁻¹⁷ and the electrochemical reduction of CO_2 must also compete with the electrochemical reduction of protons (and/or water) to hydrogen (i.e. the hydrogen evolution reaction or HER), which typically occurs at less negative potentials on most electrodes.^{18,19} In heterogeneous electrocatalysis, one of the most common techniques to improve the selectivity towards carbon products is to use metal electrodes or oxide-derived metal electrodes that have high HER overpotentials (e.g. Cu, Sn, Au).²⁰⁻²³ However, there is still great interest in understanding how to better control the selectivity of the carbon products produced from electrochemical CO_2 reduction and to design catalysts in which the product selectivity could be finely tuned.²⁴

Indium (In) is one of the least active metals for the HER,²⁵ and the Bocarsly group has shown that In and indium-oxide nanoparticles can produce formate with high selectivity in aqueous environments.²⁶⁻²⁸ The Bocarsly group²⁶⁻²⁸ has also demonstrated that the native surface oxide layer

on In metal electrodes and In_2O_3 nanoparticles will be electrochemically reduced to In^0 in the absence of CO_2 . However, in the presence of CO_2 , indium oxide is not reduced to In^0 . Instead, an In-CO_3 surface adsorbed intermediate forms on the oxide layer, which is responsible for producing formate through the two-electron, two-proton reduction. Because of the vital role of the oxide layer in the mechanism for producing formate on In-based catalysts, we hypothesized that if electrochemical CO_2 reduction could occur directly on a In^0 surface (e.g. by reducing the surface oxide layer to In^0 *in-situ* prior to exposure of CO_2), the product selectivity may change. There exists prior evidence that this may be the case. For example, Li and co-workers demonstrated that indium-based catalyst, prepared via *in-situ* electrodeposition, was able to selectively reduce CO_2 to CO in acetonitrile containing an imidazolium ionic liquid.²⁹ In addition, In_2O_3 have also recently been shown to be a photocatalyst for converting CO_2 to CO and CH_4 when coated with carbon and combined with Pt catalysts.³⁰

Here, we show that the selectivity of electrochemical CO_2 reduction on In-based electrocatalysts can be tuned to produce CO, as opposed to formate, at lower potentials (onset potential around -1.0 V vs. Ag/AgCl) in aqueous electrolytes. By electrochemically reducing In_2O_3 nanoparticles *in-situ* prior to exposure of CO_2 we observed the formation of a In^0 - In_2O_3 composite. Then when exposed to CO_2 , the In-based composite nanocatalysts will electrochemically convert CO_2 to CO with near 100% selectivity. We attribute the increased CO selectivity to the direct exposure of In^0 to CO_2 in solution that typically does not exist to due to the native oxide layer that forms on In metal. We also report the utilization of Substrate Generation-Tip Collection Scanning Electrochemical Microscopy (SG-TC SECM) to measure the production of CO as function of applied potential. SECM has been widely used in the study of water-splitting electrocatalysis,³¹⁻³⁵ but has been underutilized in studying electrochemical CO_2 reduction. Here we show that by using a Pt SECM tip electrode, we can selectively collect CO *in-situ* during the voltammetry experiment as it is produced on the catalytic electrode to obtain accurate potential dependent measurements of CO production.

2.3 Materials and Methods

2.3.1 Chemicals

Indium (III) chloride (>99.9% Chem-Impex International), acetylacetonone (>99.0+ TCI), Sodium sulfate (>99.0%, ACS Reagent, Fisher), ethanol (99.9% Decon Labs), UHP Argon and UHP CO₂ (Matheson) were all used as received without additional purification. 18.2 mΩ (Millipore) water was used in all syntheses and solutions.

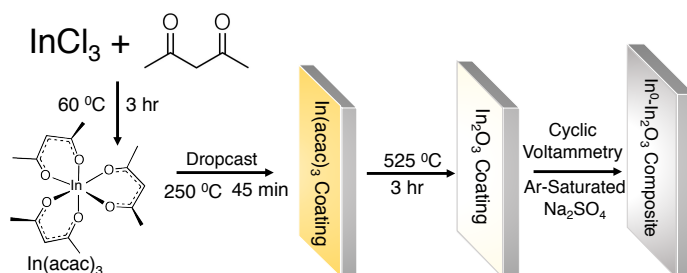


Figure 2.1. Schematic of the synthesis route for producing the In⁰-In₂O₃ composite structure.

2.3.2 Catalyst Synthesis

Indium-oxide nanoparticles were synthesized by modifying the method reported by Alam and Cameron for producing indium-tin oxide.³⁶ Briefly, an In(acac)₃ solution was synthesized by adding 25 mL of acetylacetonone to a roundbottom flask with Teflon boiling beads and a stir bar, to which 5.0 g of Indium(III) chloride were then added. Subsequently, an additional 50 mL of acetylacetonone was added. The roundbottom flask was fitted with a water cooled condenser and refluxed at 60 °C while stirring vigorously. During the refluxing period the solution first turned pale yellow then darkened. After 3 hours the solution was allowed to cool to room temperature and 36 mL of absolute ethanol was added. The In(acac)₃ solution was dropcast onto fluorine-doped tin oxide (FTO) glass (Sigma-Aldrich) and then dried at 250 °C for 3 hours. Prior to dropcasting, the FTO glass was cleaned with a dilute soap solution, rinsed with water, rinsed with ethanol, and then sonicated in ethanol for 15 minutes. The dropcast In(acac)₃ coated electrodes were then annealed at 525 °C for 3 hours to produce In₂O₃ nanoparticles. The In⁰-In₂O₃ composite structure was formed by 10 sequential cyclic voltammetry experiments performed at 100 mV/s from -0.6 to -1.3 V vs Ag/AgCl in 0.1M Na₂SO₄ pH 5.6 after purging the cell with Ar gas. The cell was allowed to

reach open circuit potential prior to each scan.

2.3.3 Materials Characterization

Scanning electron microscope (SEM) images were obtained using a FEI Versa 3D Dual Beam SEM. X-ray Diffraction (XRD) data were obtained with a Panalytical Empyrean X-ray diffractometer with a 0.013° step size and $\text{CuK}\alpha$ radiation ($\lambda = 1.54$ over a 2θ range of $10.0^\circ - 90.0^\circ$).

2.3.4 Electrochemical and Product Characterization

All electrochemical measurements were obtained via a CH Instruments (Austin, TX) potentiostat. The Scanning Electrochemical Microscopy (SECM) experiments were performed on a custom built SECM as described previously.³⁷ Cyclic Voltammetry was performed in a custom Teflon cell with 0.1 M Na_2SO_4 at an initial pH of 5.6 under both Ar and CO_2 atmospheres. All potentials were referenced to the saturated Ag/AgCl electrode with a porous Teflon tip (CH Instruments). A 200 μm Pt wire (Electron Microscopy Instruments) was used as the counter electrode for CV experiments. The size of all working electrodes for cyclic voltammetry experiments was 0.154 cm^2 . Indium foil (99.99% Alfa Aesar) was used as received with native oxide coating. All bulk electrolyses were performed in a custom gas tight cell as shown in the Supporting Information with a tungsten counter electrode compartment separated from the working electrode with a Nafion membrane. Aqueous electrolysis products were analyzed on a Bruker AVIIIHD 400MHz NMR. Gas phase product characterization was performed with a Shimadzu 2014 GC with a Restek ShinCarbon ST Micropacked column, ID 1.0 mm, Length 2 m, Mesh 100/120.

2.4 Results and Discussion

2.4.1 Materials Synthesis and Characterization

The $\text{In}^0\text{-In}_2\text{O}_3$ composite was synthesized (Scheme 2.1) by first refluxing InCl_3 in acetylacetone to form an $\text{In}(\text{acac})_3$ metal complex. The $\text{In}(\text{acac})_3$ complex was dropcast on a FTO-coated glass electrode, which was subsequently thermally annealed to form In_2O_3 nanoparticles. X-ray diffraction (XRD) data (Fig. 2.2a - black trace) confirms the In_2O_3 crystal structure of the untreated

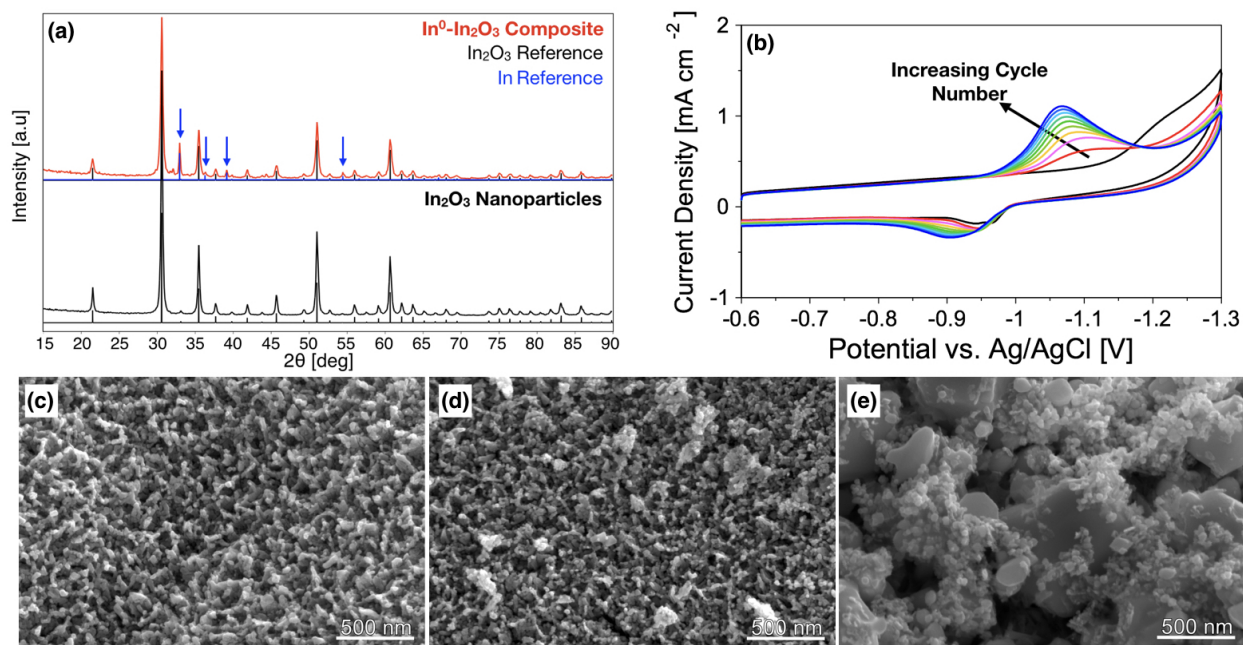


Figure 2.2. X-ray Diffraction data of the $\text{In}^0\text{-In}_2\text{O}_3$ composite structure (top) and the untreated In_2O_3 nanoparticles (bottom) showing the presence of both In^0 (blue arrows) and In_2O_3 in the composite structure, but only In_2O_3 in the untreated nanoparticles (a). Ten consecutive cyclic voltammograms (1^{st} cycle - black trace, 10^{th} cycle - blue trace) of the In_2O_3 nanoparticles in Ar-saturated 0.1 M Na_2SO_4 at 100 mV s^{-1} showing that the In_2O_3 reduction peak increases with each subsequent cyclic voltammogram (b). SEM images of the untreated In_2O_3 nanoparticles (c), the $\text{In}^0\text{-In}_2\text{O}_3$ after voltammetry cycling in Ar-saturated Na_2SO_4 (d), and $\text{In}^0\text{-In}_2\text{O}_3$ after voltammetry cycling in CO_2 -saturated Na_2SO_4 (e).

nanoparticles, and Scherrer analysis combined with SEM images (Fig. 2.2c) show a network of In_2O_3 nanoparticles that are c.a. 20 nm in size.

As stated above, our goal was to reduce the In_2O_3 nanoparticles to In^0 *in-situ*, to allow CO_2 reduction to occur on In^0 . In order to create the $\text{In}^0\text{-In}_2\text{O}_3$ composite, 10 consecutive cyclic-voltammograms were performed on the In_2O_3 nanoparticles in Ar-saturated Na_2SO_4 (Fig. 2.2b). During the first potential sweep (black trace of Fig. 2.2b), we observed that the typical $\text{In}_2\text{O}_3/\text{In}^0$ reduction peak²⁶ was not present, but the oxidation wave was present on the reverse scan. Subsequent cycles (red through blue traces of Fig. 2.2b) show an increase in both the reduction and oxidation wave of the $\text{In}_2\text{O}_3/\text{In}^0$ redox couple. During these potential sweeps in Ar-saturated Na_2SO_4 , the reduction and oxidation peaks grow asymmetrically, with the reduction peak growing larger with each cycle compared to the oxidation peak (See Supporting Information Figure S1a for details). This asymmetry in the cyclic voltammetry allows for the formation of the In^0 to grow on the surface and thus producing the $\text{In}^0\text{-In}_2\text{O}_3$ composite structure where the In^0 is exposed to

the electrolyte. SEM images of the $\text{In}^0\text{-In}_2\text{O}_3$ composite structure after voltammetry cycling in Ar-saturated Na_2SO_4 show very little change in the overall structure of the catalyst. However, when cyclic voltammetry was performed in CO_2 -saturated Na_2SO_4 , the particles become a metallic-gray color in appearance as opposed to the white color of the untreated In_2O_3 nanoparticles (Supporting Information Figure S1b). In addition, SEM images show that upon exposure to CO_2 , crystal aggregation was observed as shown by the SEM image of the $\text{In}^0\text{-In}_2\text{O}_3$ composite (Fig. 2.2e). XRD data on the In_2O_3 nanoparticles after electrochemical reduction via cyclic voltammetry cycling in Ar-saturated Na_2SO_4 and exposure to CO_2 (Fig. 2.2a - red trace) show the formation of new peaks at c.a. 32° and 38° , indicative of the formation of In^0 and confirming the creation of the $\text{In}^0\text{-In}_2\text{O}_3$ composite structure.

2.4.2 Electrochemical Characterization

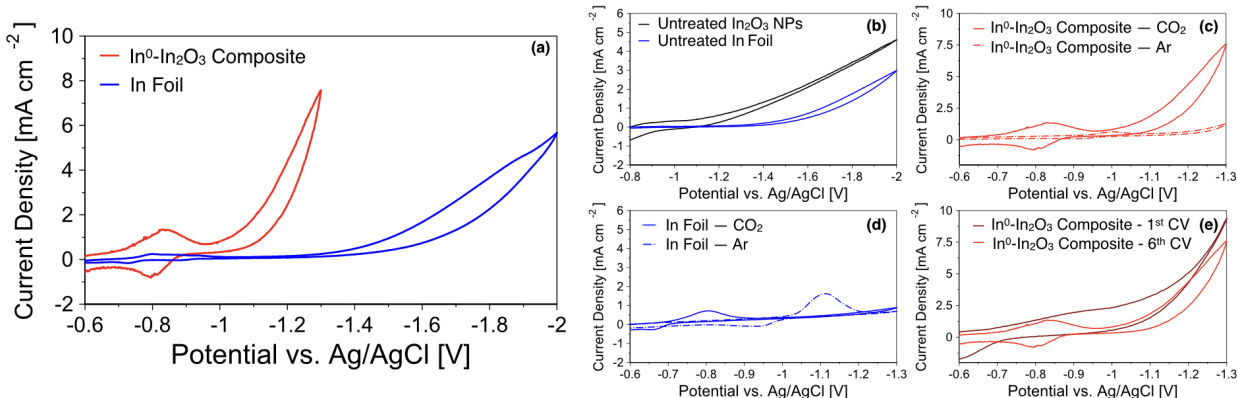


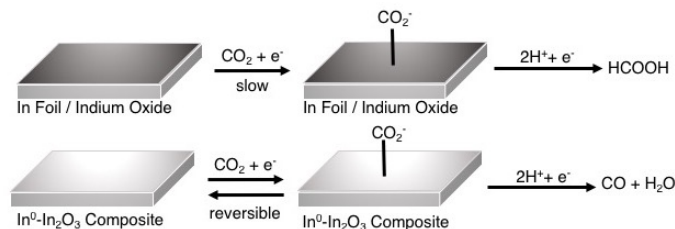
Figure 2.3. Cyclic voltammograms of the $\text{In}^0\text{-In}_2\text{O}_3$ composite structure, a In foil electrode, and untreated In_2O_3 nanoparticles. Comparison voltammograms of the $\text{In}^0\text{-In}_2\text{O}_3$ composite structure and an In foil electrode at 10 mV s^{-1} in CO_2 -saturated $0.1 \text{ M Na}_2\text{SO}_4$ (a). Comparison voltammograms of untreated In_2O_3 nanoparticles and an In foil electrode at 50 mV s^{-1} in CO_2 -saturated $0.1 \text{ M Na}_2\text{SO}_4$ (b). Comparison voltammograms of the $\text{In}^0\text{-In}_2\text{O}_3$ composite structure in CO_2 -saturated and Ar-saturated $0.1 \text{ M Na}_2\text{SO}_4$ at 10 mV s^{-1} (c). Comparison voltammograms of the In foil electrode in CO_2 -saturated and Ar-saturated $0.1 \text{ M Na}_2\text{SO}_4$ at 10 mV s^{-1} (d). Comparison voltammograms between the 1st cycle and 6th cycle of the $\text{In}^0\text{-In}_2\text{O}_3$ composite structure in CO_2 -saturated $0.1 \text{ M Na}_2\text{SO}_4$ (e).

Cyclic voltammograms of the $\text{In}^0\text{-In}_2\text{O}_3$ composite structure, In foil electrodes, and untreated In_2O_3 nanoparticles are shown in Figure 2.3. Comparing the voltammograms of the $\text{In}^0\text{-In}_2\text{O}_3$ composite material to a standard polycrystalline In foil electrode (Fig. 2.3a) shows that the onset potential for electrochemical CO_2 reduction is c.a. 500 mV lower for the $\text{In}^0\text{-In}_2\text{O}_3$ composite material compared to the standard In foil electrode. To illustrate that creating the $\text{In}^0\text{-In}_2\text{O}_3$

composite improves the electrocatalysis for CO₂ reduction, Figure 2.3b shows the voltammograms of the untreated In₂O₃ compared to the In foil electrode. For both the In-foil electrode and the untreated In₂O₃ nanoparticles, the typical In₂O₃/In⁰ redox wave that occurs around -1.0 V vs. Ag/AgCl in Ar-saturated aqueous environments is not present. This is presumably due to the In-CO₃ surface adsorbed intermediate that forms on the oxide layer, which is a key intermediate in the production of formate. Also, the onset potential for CO₂ reduction electrocatalysis decreases from about -1.6 V vs Ag/AgCl on the In foil to about -1.2 V vs Ag/AgCl on the untreated In₂O₃ nanoparticles as expected (Fig. 2.3b)^{26,28} However, by simply pretreating the In₂O₃ nanoparticles by performing cyclic voltammetry in Ar-saturated electrolytes, and then directly exposing the catalyst to CO₂, we observed a decrease in the onset potential for CO₂ electrolysis by over 200 mV (c.a. -1.0 V vs Ag/AgCl) compared to the untreated In₂O₃ nanoparticles.

Comparing the voltammograms of the In⁰-In₂O₃ composite in both Ar-saturated Na₂SO₄ and CO₂-saturated Na₂SO₄ (Fig. 2.3c) shows that the catalytic wave is observed only when CO₂ is present, thus suggesting a high selectivity towards carbon products compared to hydrogen. Voltmetry experiments performed in pH 4.5 Ar-saturated acetate buffer show that the pH change that occurs when the electrolyte is saturated with CO₂ is not responsible for the increase in catalytic current (see Supporting Information Figure S5). In addition, the typical In₂O₃/In⁰ redox wave is present around -1.0 V vs Ag/AgCl in Ar-saturated Na₂SO₄ but is not present in CO₂-saturated Na₂SO₄. However, instead of being electrochemically silent, we observed a new redox feature (at c.a. -0.75 V vs Ag/AgCl) on the In⁰-In₂O₃ electrode that is only present when the electrode is exposed to CO₂-saturated electrolyte. We attribute this redox feature to the formation of a surface-adsorbed intermediate on the active-site of the In⁰-In₂O₃ composite structure. The difference in voltage between the cathodic peak and anodic peak (ΔE_p) of this redox wave is c.a. 50-60 mV, which is indicative of a reversible one-electron process.³⁸ On the In foil electrode, we also observed the expected In₂O₃/In⁰ redox wave present around -1.0 V vs Ag/AgCl in Ar-saturated Na₂SO₄, and again this feature is not present in CO₂-saturated electrolyte (Fig. 2.3d). While the In foil electrode is electrochemically silent when cycled from -0.8 V to -2.0 V vs Ag/AgCl (Fig. 2.3b) as expected,²⁶ when it is allowed to reach -0.6 V vs Ag/AgCl, we observed a similar redox feature at c.a. -0.75 V vs Ag/AgCl only when the electrode is in CO₂-saturated electrolyte. However, on the In foil electrode the ΔE_p is c.a. 120 mV suggesting a irreversible electron-transfer step. It should

be noted, however, that the redox-feature on the $\text{In}^0\text{-In}_2\text{O}_3$ is not reversible on the first few cycles, but becomes reversible as the electrode is cycled in CO_2 -saturated electrolyte (Fig. 2.3e).



Scheme 2.1. Schematic of the reaction pathways for the reduction of CO_2 where CO_2^- generically refers to any adsorbed carbon intermediate

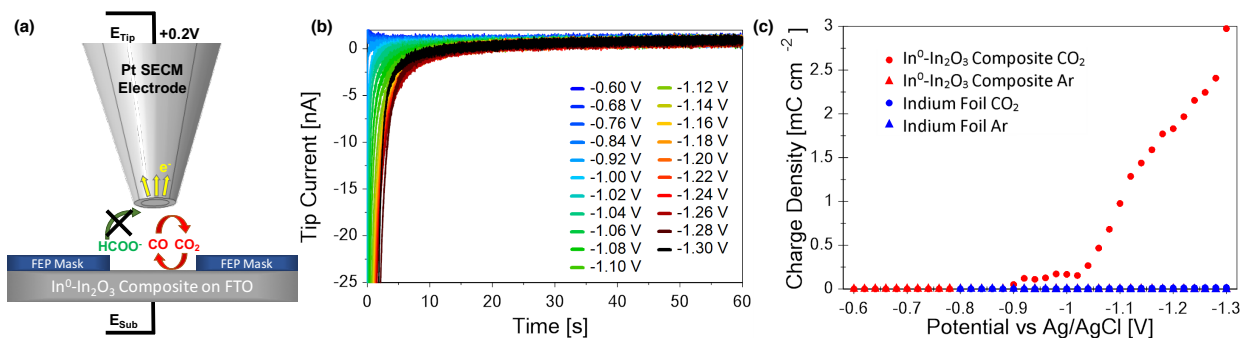


Figure 2.4. Schematic of the SG-TC SECM experiment showing the collection of CO but not COOH^- on a Pt tip electrode (a). Collection tip current vs time as a function of the potential applied to the $\text{In}^0\text{-In}_2\text{O}_3$ electrode in CO_2 -saturated 0.1 M Na_2SO_4 (b). Product collection charge density as a function of the potential applied to the catalytic electrode for both the $\text{In}^0\text{-In}_2\text{O}_3$ composite and the In foil electrode in both CO_2 -saturated and Ar-saturated 0.1 M Na_2SO_4 (c).

We attribute the improved kinetics (i.e. lower overpotential) for electrochemical CO_2 reduction on the $\text{In}^0\text{-In}_2\text{O}_3$ composite compared to an In foil electrode to the reversibility of this first electron-transfer step (Scheme 2.1). While, to the best of our knowledge, this is the first time this has been reported on an In-based electrode, the concept of a metallic coating on an oxide increasing the kinetics of the first electron-transfer step has been reported by Kanan and co-workers.¹⁰ The Kanan group showed that an oxide-derived Au electrode had a reversible first electron-transfer step, while with a polycrystalline Au electrode the first electron-transfer step was rate determining. Although both the oxide derived Au electrode and polycrystalline Au electrode produced CO as the major product, the oxide-derived electrode showed vastly improved kinetics. Here, we show a similar $\text{In}^0\text{-In}_2\text{O}_3$ composite electrode also has a reversible first-electron transfer step and faster kinetics for electrochemical CO_2 reduction. In addition, by allowing the reduction to occur on the

surface of In^0 not only does the first electron-transfer step to become reversible, but the selectivity changes such that CO is produced instead of formate.

2.4.3 Product Detection and Scanning Electrochemical Microscopy

The voltammetry data shown in Figure 2.3a suggests that on the $\text{In}^0\text{-In}_2\text{O}_3$ composite material, there is a first electron-transfer step to form surface adsorbed intermediates at c.a. -0.8 V vs Ag/AgCl followed by catalysis at -1.0 V vs Ag/AgCl. In addition, because of the change in the reversibility of the first electron transfer step and the much lower onset potential for catalysis, we hypothesized that this material may be producing CO instead of formate—the typical product on In-based electrocatalysts. To test this hypothesis, one could perform bulk electrolysis experiments over a wide range of potentials and collect gas products for analysis by gas chromatography. However, this can be a very time intensive experiment. Here, we report a novel utilization of Scanning Electrochemical Microscopy where CO can be selectively detected from formate on the tip of a SECM electrode *in-situ* during a voltammetry experiment. We anticipate that this technique could be widely used in studying CO_2 -reducing electrocatalysts.

It is possible to selectively oxidize CO and not formate on a Pt electrode at $+0.2$ V vs Ag/AgCl (See Supporting Information Figure S2). Thus, to determine the potential dependent formation of CO on the $\text{In}^0\text{-In}_2\text{O}_3$ composite, we utilized a masked electrode technique as we have previously reported.³³ Here a FEP mask with a c.a. 100 μm diameter center void was placed on the $\text{In}^0\text{-In}_2\text{O}_3$ composite electrode and a 200 μm Pt electrode was approached such that the tip /substrate distance was c.a. 10 μm . (Fig. 2.4a). Then a potential pulse was applied to the $\text{In}^0\text{-In}_2\text{O}_3$ composite electrode for 20 s per potential over a wide range of potentials to generate the CO_2 reduction products. After the 20 s potential pulse, the $\text{In}^0\text{-In}_2\text{O}_3$ composite electrode was brought to open-circuit while simultaneously applying $+0.2$ V vs Ag/AgCl to the Pt tip electrode. Performing this experiment allows us to electrochemically collect any CO and or H_2 (See Supporting Information Figure S2) that is produced on the catalytic electrode because formate is not electrochemically active at this potential.

Figure 2.4b shows the current vs. time data for the collection on the Pt tip electrode at a series of potentials that were applied to the $\text{In}^0\text{-In}_2\text{O}_3$ composite electrode. Similar SECM experiments were performed on the $\text{In}^0\text{-In}_2\text{O}_3$ composite electrode in Ar-saturated Na_2SO_4 , and on the In foil

electrode in both CO₂-saturated and Ar-saturated Na₂SO₄ (See Supporting Information Figure S3). By integrating the net current versus time, we are able to quantify the amount of charge collected on the Pt tip electrode as a function of applied potential on the In⁰-In₂O₃ composite electrode (Fig. 2.4c). Comparing Figure 2.4c to the voltammogram shown in Figure 2.3a reveals several insights about the electrochemistry of the In⁰-In₂O₃ composite electrode in CO₂-saturated Na₂SO₄. First, because we observed no collection on the Pt tip electrode in the potential range of -0.6 V to -0.9 V vs Ag/AgCl, we can conclude that the redox feature that we observed at that potential in the voltammetry is not producing either CO or H₂. Second, because we see the onset and increase in collection on the Pt tip after -1.0 V, as we observed in the voltammogram proves that the onset wave at -1.0 V vs Ag/AgCl is in fact electrocatalysis of CO₂. Moreover, since we are able to collect the product on the Pt tip electrode, it shows that formate can not be the major product, because it is not electrochemically active on Pt at +0.2 V vs Ag/AgCl. SECM experiments on the In⁰-In₂O₃ composite electrode in Ar-saturated Na₂SO₄ show no collection of products, even though H₂ oxidation will occur at +0.2 V vs Ag/AgCl (See Supporting Information Fig. S2). This indicates that the In⁰-In₂O₃ electrocatalyst is highly selective for producing carbon-based products. Finally, SECM measurements on the In foil electrode show no collection of products in either CO₂-saturated or Ar-saturated electrolytes, demonstrating that the In-foil electrode does not produce CO within the potential range investigated.

To validate the results of our SECM experiment, we performed bulk-electrolysis experiments on the In⁰-In₂O₃ composite electrode in CO₂-saturated Na₂SO₄ at -1.3 V vs Ag/AgCl (See Supporting Information Figure S4 for details). Gas phase products were measured by gas chromatography and liquid phase products were measured by proton NMR. Gas phase measurements confirmed that CO is the only quantifiable gas phase product produced with only trace (i.e. non-quantifiable) amounts of H₂ observed. Proton NMR on the liquid phase products show no liquid phase products including formate. Thus, we can conclude this material can electrochemically reduce CO₂ to CO with near 100% selectivity. However, quantification of the GC data does show a potential drawback of this catalyst in terms of faradaic efficiency. We measured a faradaic efficiency of CO production of 36 ± 3 % on the In⁰-In₂O₃ composite electrode (See Table S1 for reproducibility measurements), but since we have confirmed that no other products are being formed, further work is required to determine how the additional electrons are being consumed. For example, it may be possible that

further reduction of In_2O_3 may be occurring simultaneously with reduction of CO_2 . In addition, we may be observing resistive losses in our bulk-electrolysis electrochemical cell, and further work in this area will be in cell optimization. However, this highlights the advantage of using SECM to characterize products to those who are interesting in the materials development of electrocatalysts, due to the effort needed to properly perform bulk-electrolysis experiments.

2.5 Conclusions

Herein we demonstrated that by electrochemically reducing In_2O_3 nanoparticles *in-situ* prior to exposure of CO_2 we could create a $\text{In}^0\text{-In}_2\text{O}_3$ composite. Then, when exposed to CO_2 , the In-based composite nanocatalysts will electrochemically convert CO_2 to CO with near 100% selectivity. This demonstrates that the CO_2 -reduction products on In-based catalysts can be tuned based on the oxidation state of the In that is exposed to the electrolyte. We attribute the increased CO selectivity to the direct exposure of In^0 to CO_2 in solution that typically does not exist due to the native oxide layer that forms on In metal. In addition, we observed that the first electron-transfer step in the electrochemical reduction of CO_2 on the $\text{In}^0\text{-In}_2\text{O}_3$ was reversible, while it was irreversible on a standard In-foil electrode, suggesting that the mechanisms may be different on these two materials. We also report the utilization of Substrate Generation-Tip Collection Scanning Electrochemical Microscopy (SG-TC SECM) to measure the production of CO as function of applied potential. By using a Pt SECM tip electrode, we can selectively collect CO *in-situ* during the voltammetry experiment as it is produced on the catalytic electrode to obtain accurate potential dependent measurements of CO production. While this catalyst was able to produce CO with near 100% selectivity, future work will focus on improving the faradaic efficiency of In-based catalysts.

2.6 Acknowledgement of Contributions

SECM and SEM catalyst characterization was carried out by Dylan Jantz, XRD Data was taken by Anand Ramanathan.

2.7 Supporting Figures

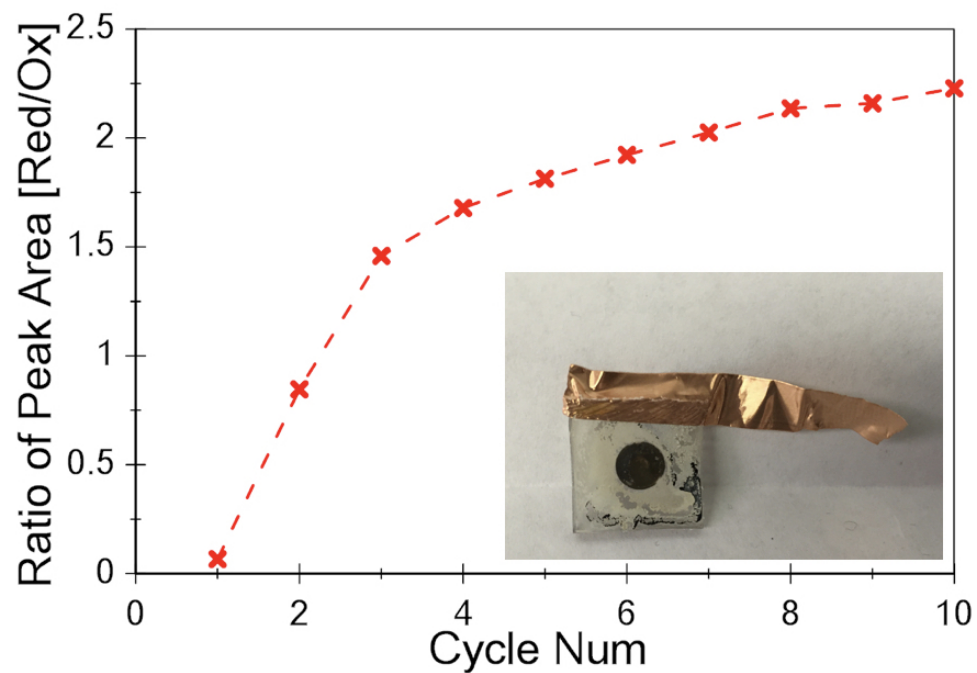


Figure 2.5. Ratio of the peak area of the reduction wave over the oxidation wave for consecutive voltammetry cycles of the In_2O_3 nanoparticles in Ar-saturated Na_2SO_4 . Inset is a photograph of the In_2O_3 electrode showing the coloration change (black circle) that occurs after cycle in CO_2 saturated Na_2SO_4 .

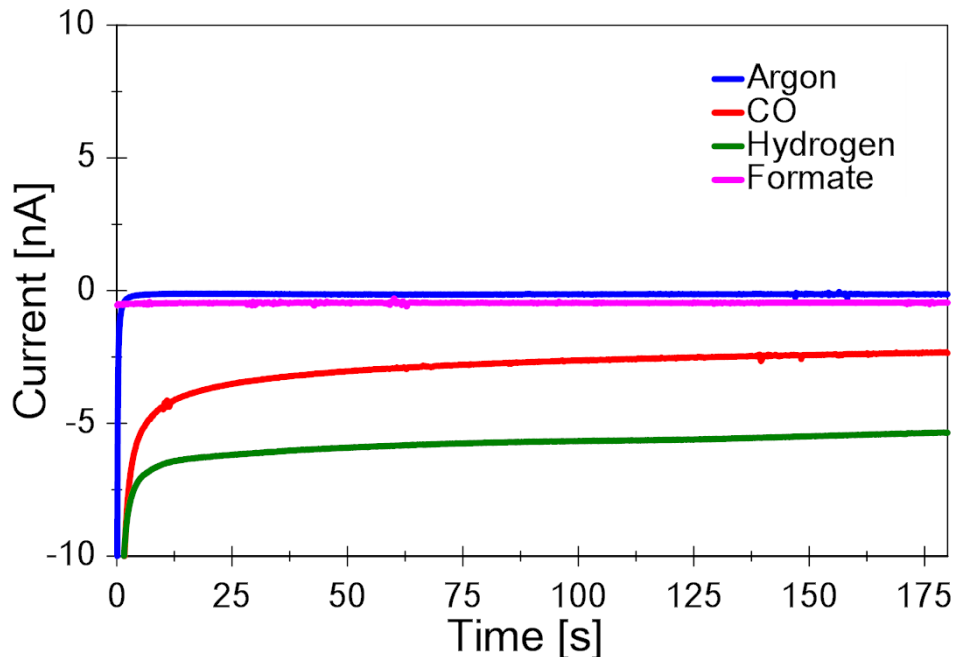


Figure 2.6. Current as a function of time for a 200 micron diameter Pt SECM tip electrode in Ar-saturated, CO-saturated, H₂-saturated 0.1 M Na₂SO₄ along with 0.1 M NaCOOH at +0.2 V vs Ag/AgCl. This shows that CO and H₂ can be collected on a Pt tip electrode while COOH⁻ can not be collected.

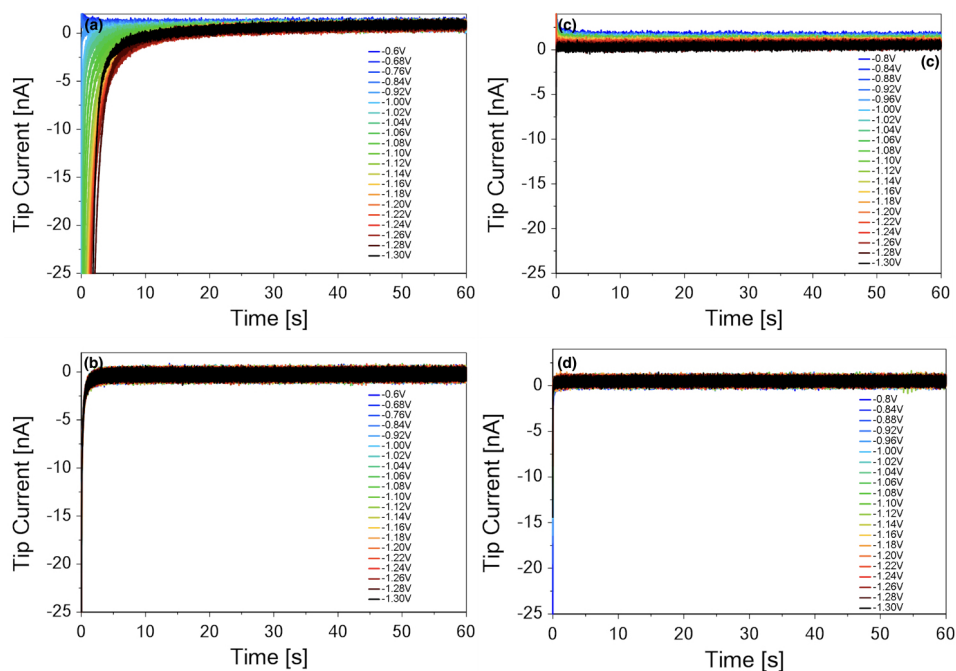


Figure 2.7. Current as a function of time for a 200 micron diameter Pt SECM tip electrode in Ar-saturated, CO-saturated, H₂-saturated 0.1 M Na₂SO₄ along with 0.01 M NaCOOH in 0.1 M Na₂SO₄ at +0.2 V vs Ag/AgCl. This shows that CO and H₂ can be collected on a Pt tip electrode while COOH⁻ can not be collected.

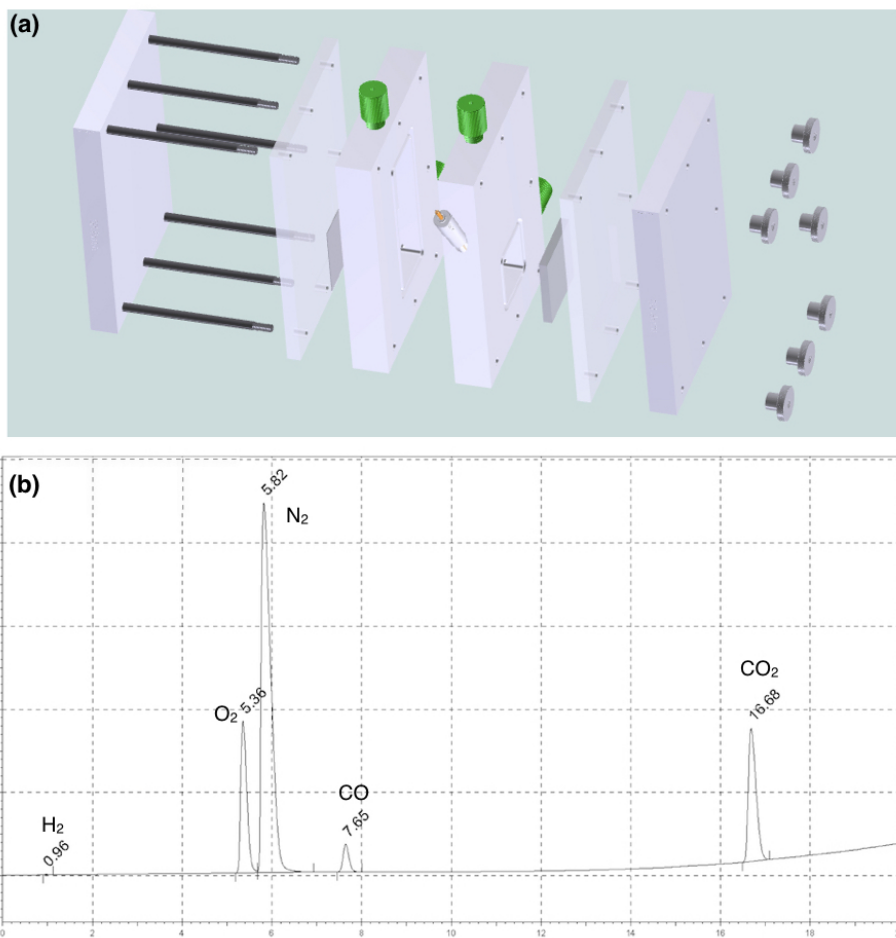


Figure 2.8. Schematic showing the cell used for the bulk electrolysis measurements (a). Example gas chromatography data showing the detection of CO and non-quantifiable detection of H₂ (b).

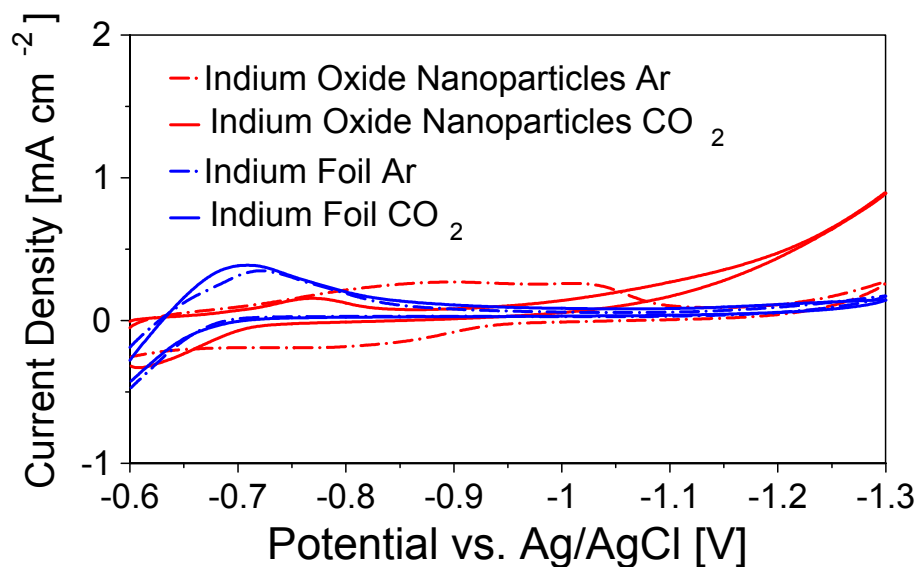


Figure 2.9. Cyclic voltammetry data of CO₂-saturated and Ar-saturated 0.1 M Na₂SO₄ in pH 4.5 acetate buffer taken at 5 mV s⁻¹ on both a thinly coated In⁰-In₂O₃ composite sample and on In foil. This demonstrates that the pH change that occurs when the electrolyte is saturated with CO₂ is not responsible for the increase in catalytic current.

Table 2.1. Reproducibility results showing the faradaic efficiency of CO₂ reduction on In⁰-In₂O₃ composite structure.

Experiment	Charge Passed [C]	Quantity of CO [μ mol]	Faradaic Efficiency [%]
Run 1	5.23	1.05E-5	38.75
Run 2	13.55	2.44E-5	34.75
Run 3	9.67	1.70E-5	33.97
Average			35.82

References

- [1] Nocera, D. G. (2017) Solar Fuels and Solar Chemicals Industry. *Accounts of Chemical Research* 50, 616–619.
- [2] Omae, I. (2006) Aspects of carbon dioxide utilization. *Catalysis Today* 115, 33–52.
- [3] Sanz-Perez, E. S., Murdock, C. R., Didas, S. A., and Jones, C. W. (2016) Direct Capture of CO₂ from Ambient Air. *Chemical Reviews* 116, 11840–11876.
- [4] Roy, S. C., Varghese, O. K., Paulose, M., and Grimes, C. A. (2010) Toward Solar Fuels : Photocatalytic Hydrocarbons. *ACS Nano* 4, 1259–1278.
- [5] Lum, Y., Yue, B., Lobaccaro, P., Bell, A. T., and Ager, J. W. (2017) Optimizing C–C coupling on Oxide-Derived copper catalysts for electrochemical CO₂ reduction. *The Journal of Physical Chemistry C* 121, 14191–14203.
- [6] Hori, Y. i. *Modern aspects of electrochemistry*; Springer, 2008; pp 89–189.
- [7] Costentin, C., Robert, M., and Saveant, J.-M. (2013) Catalysis of the electrochemical reduction of carbon dioxide. *Chem. Soc. Rev.* 42, 2423–2436.
- [8] Torelli, D. A., Francis, S. A., Crompton, J. C., Javier, A., Thompson, J. R., Brunshwig, B. S., Soriaga, M. P., and Lewis, N. S. (2016) Nickel–Gallium-Catalyzed Electrochemical Reduction of CO₂ to Highly Reduced Products at Low Overpotentials. *ACS Catalysis* 6, 2100–2104.
- [9] Weng, Z., Jiang, J., Wu, Y., Wu, Z., Guo, X., Materna, K. L., Liu, W., Batista, V. S., Brudvig, G. W., and Wang, H. (2016) Electrochemical CO₂ reduction to hydrocarbons on a heterogeneous molecular Cu catalyst in aqueous solution. *Journal of the American Chemical Society* 138, 8076–8079.

- [10] Li, C. W., and Kanan, M. W. (2012) CO₂ reduction at low overpotential on Cu electrodes resulting from the reduction of thick Cu₂O films. *Journal of the American Chemical Society* *134*, 7231–7234.
- [11] Benson, E. E., Kubiak, C. P., Sathrum, A. J., and Smieja, J. M. (2009) Electrocatalytic and homogeneous approaches to conversion of CO₂ to liquid fuels. *Chemical Society Reviews* *38*, 89–99.
- [12] Oloman, C., and Li, H. (2008) Electrochemical processing of carbon dioxide. *ChemSusChem* *1*, 385–391.
- [13] Sánchez-Sánchez, C. M., Montiel, V., Tryk, D. A., Aldaz, A., and Fujishima, A. (2001) Electrochemical approaches to alleviation of the problem of carbon dioxide accumulation. *Pure and Applied Chemistry* *73*, 1917–1927.
- [14] Delacourt, C., Ridgway, P. L., Kerr, J. B., and Newman, J. (2008) Design of an Electrochemical Cell Making Syngas (CO + H₂) from CO₂ and H₂O Reduction at Room Temperature. *Journal of The Electrochemical Society* *155*, B42–B49.
- [15] Kuhl, K. P., Cave, E. R., Abram, D. N., and Jaramillo, T. F. (2012) New insights into the electrochemical reduction of carbon dioxide on metallic copper surfaces. *Energy and Environmental Science* *5*, 7050–7059.
- [16] Lu, Q., and Jiao, F. (2016) Electrochemical CO₂ reduction: Electrocatalyst, reaction mechanism, and process engineering. *Nano Energy* *29*, 439–456.
- [17] Kortlever, R., Shen, J., Schouten, K. J. P., Calle-Vallejo, F., and Koper, M. T. M. (2015) Catalysts and Reaction Pathways for the Electrochemical Reduction of Carbon Dioxide. *Journal of Physical Chemistry Letters* *6*, 4073–4082.
- [18] Zhang, Y.-J., Sethuraman, V., Michalsky, R., and Peterson, A. A. (2014) Competition between CO₂ Reduction and H₂ Evolution on Transition-Metal Electrocatalysts. *ACS Catalysis* *4*, 3742–3748.
- [19] Peterson, A., and Nørskov, J. (2012) Activity Descriptors for CO₂ Electroreduction to Methane on Transition Metal Catalysts. *The Journal of Physical Chemistry Letters* *3*, 251–258.

- [20] Kuhl, K. P., Hatsukade, T., Cave, E. R., Abram, D. N., Kibsgaard, J., and Jaramillo, T. F. (2014) Electrocatalytic conversion of carbon dioxide to methane and methanol on transition metal surfaces. *Journal of the American Chemical Society* *136*, 14107–14113.
- [21] Chen, Y., Li, C. W., and Kanan, M. W. (2012) Aqueous CO₂ reduction at very low overpotential on oxide-derived Au nanoparticles. *Journal of the American Chemical Society* *134*, 19969–19972.
- [22] Dutta, A., Rahaman, M., Luedi, N. C., Mohos, M., and Broekmann, P. (2016) Morphology Matters: Tuning the Product Distribution of CO₂ Electroreduction on Oxide-Derived Cu Foam Catalysts. *ACS Catalysis* *6*, 3804–3814.
- [23] Ren, D., Deng, Y., Handoko, A. D., Chen, C. S., Malkhandi, S., and Yeo, B. S. (2015) Selective Electrochemical Reduction of Carbon Dioxide to Ethylene and Ethanol on Copper(I) oxide catalysts. *ACS Catalysis* *5*, 2814–2821.
- [24] others., et al. (2017) Tuning Sn-Catalysis for Electrochemical Reduction of CO₂ to CO via the Core/Shell Cu/SnO₂ Structure. *Journal of the American Chemical Society* *139*, 4290–4293.
- [25] Leonard, K. C., and Bard, A. J. (2013) Pattern recognition correlating materials properties of the elements to their kinetics for the hydrogen evolution reaction. *Journal of the American Chemical Society* *135*, 15885–15889.
- [26] Detweiler, Z. M., White, J. L., Bernasek, S. L., and Bocarsly, A. B. (2014) Anodized indium metal electrodes for enhanced carbon dioxide reduction in aqueous electrolyte. *Langmuir* *30*, 7593–7600.
- [27] Pander III, J. E., Baruch, M. F., and Bocarsly, A. B. (2016) Probing the Mechanism of Aqueous CO₂ Reduction on Post-Transition-Metal Electrodes using ATR-IR Spectroelectrochemistry. *ACS Catalysis* *6*, 7824–7833.
- [28] White, J. L., and Bocarsly, A. B. (2016) Enhanced Carbon Dioxide Reduction Activity on Indium-Based Nanoparticles. *Journal of The Electrochemical Society* *163*, H410–H416.

- [29] Ding, C., Li, A., Lu, S.-M., Zhang, H., and Li, C. (2016) In Situ Electrodeposited Indium Nanocrystals for Efficient CO₂ Reduction to CO with Low Overpotential. *ACS Catalysis* 6, 6438–6443.
- [30] Pan, Y.-X., You, Y., Xin, S., Li, Y., Fu, G., Cui, Z., Men, Y.-L., Cao, F.-F., Yu, S.-H., and Goodenough, J. B. (2017) Photocatalytic CO₂ Reduction by Carbon-Coated Indium-Oxide Nanobelts. *Journal of the American Chemical Society* 139, 4123–4129.
- [31] Park, H. S., Leonard, K. C., and Bard, A. J. (2013) Surface interrogation scanning electrochemical microscopy (SI-SECM) of photoelectrochemistry at a W/Mo-BiVO₄ semiconductor electrode: quantification of hydroxyl radicals during water oxidation. *The Journal of Physical Chemistry C* 117, 12093–12102.
- [32] Leonard, K. C., and Bard, A. J. (2013) The study of multireactional electrochemical interfaces via a tip generation/substrate collection mode of scanning electrochemical microscopy: the hydrogen evolution reaction for Mn in acidic solution. *Journal of the American Chemical Society* 135, 15890–15896.
- [33] Barforoush, J. M., Jantz, D. T., Seuferling, T. E., Song, K. R., Cummings, L. C., and Leonard, K. C. (2017) Microwave-assisted synthesis of a nanoamorphous (Ni_{0.8}, Fe_{0.2}) oxide oxygen-evolving electrocatalyst containing only “fast” sites. *Journal of Materials Chemistry A* 5, 11661–11670.
- [34] Arroyo-Currás, N., and Bard, A. J. (2015) Iridium Oxidation as Observed by Surface Interrogation Scanning Electrochemical Microscopy. *The Journal of Physical Chemistry C* 119, 8147–8154.
- [35] Rodríguez-López, J., Alpuche-Avilés, M. A., and Bard, A. J. (2008) Interrogation of surfaces for the quantification of adsorbed species on electrodes: oxygen on gold and platinum in neutral Media. *Journal of the American Chemical Society* 130, 16985–16995.
- [36] Alam, M., and Cameron, D. (2000) Optical and electrical properties of transparent conductive ITO thin films deposited by sol-gel process. *Thin Solid Films* 377, 455–459.

- [37] Barforoush, J. M., McDonald, T. D., Desai, T. A., Widrig, D., Bayer, C., Brown, M. K., Cummings, L. C., and Leonard, K. C. (2016) Intelligent Scanning Electrochemical Microscopy Tip and Substrate Control Utilizing Fuzzy Logic. *Electrochimica Acta* 190, 713–719.
- [38] Bard, A. J., and Faulkner, L. R. *Electrochemical Methods: Fundamentals and Applications*, 2nd ed.; Wiley, New York, 2001.

Chapter 3

Enhanced Electrocatalytic CO₂ Conversion in Pressure-Tunable CO₂-Expanded Electrolytes

3.1 Abstract

Electrochemical CO₂ conversion to fuels and chemicals could improve industrial sustainability, as the process is readily powered by renewable energy sources. However, limited CO₂ solubility in conventional liquid phases starves active electrocatalysts of substrate and results in low conversion rates. Here, we show that multimolar CO₂ concentrations can be achieved in an organic solvent containing supporting electrolyte at relatively mild CO₂ pressures (<5 MPa) and ambient temperature, a phenomenon driven by working with CO₂ near its critical temperature (31.1 C). We term such CO₂-rich, supporting electrolyte-containing solutions as CO₂-eXpanded Electrolytes (CXEs), as significant volumetric expansion of the liquid phase accompanies CO₂ dissolution. CXEs represent a continuum of pressure-tunable media characterized by various concentrations of dissolved CO₂ and supporting electrolyte that enable electrochemistry and electrocatalysis to be performed at high CO₂ concentrations. Cathodic polarization of a model polycrystalline gold electrocatalyst in CXE media enhances CO₂ to CO conversion rates by up to an order of magnitude compared to those attainable at near-ambient pressures. The observed enhancement in catalytic rates stems

from markedly increased CO₂ availability. At the highest CO₂ pressures measured (> 2.8 MPa), electrocatalysis is significantly attenuated, ascribable only in part to increased solution resistance and occurring despite modestly improved mass transport characteristics. Taken together, these studies reveal that pressure-tunable CXE media could improve the performance of many known electrocatalysts by alleviating substrate starvation. Simultaneously, the non-monotonic enhancement of CO₂ reduction with pressure suggests that pressure is a crucial variable in maximizing the efficiency of electrocatalytic CO₂ conversion.

3.2 Introduction

Carbon dioxide (CO₂) emissions from fossil fuel combustion, industrial processes, and human activities are accelerating at an unsustainable rate. Because of the serious risks associated with anthropogenic climate change¹, a variety of strategies are being considered to curtail CO₂ accumulation in the atmosphere.²⁻⁴ One of the most attractive strategies involves capture and conversion of CO₂ (as a C1 source) to valorized chemicals and fuels.⁵⁻⁷ However, this approach is challenging because CO₂ is a thermodynamically stable and kinetically inert molecule.^{8,9} Electrochemical CO₂ conversion is appealing as it can be readily powered by clean, renewable energy (e.g., solar, hydroelectric, wind)¹⁰⁻¹² and may be carried out at near-ambient temperatures, lower than those required by thermal conversion processes.^{13,14} However, the development of practically viable electrochemical CO₂ conversion systems remains elusive. Significant challenges still remain in the development of highly active, stable, and durable electrocatalysts. In addition, there are major unmet needs in designing reactor systems that can provide high CO₂ concentrations to the electrocatalytic surface such that practically viable conversion rates can be realized.¹⁵

Low CO₂ availability at the electrode surface plagues the development of new electrocatalytic CO₂ conversion systems, especially with water as solvent.¹⁶⁻²⁰ Water accommodates relatively low CO₂ concentration (34 mM) under near-ambient headspace pressures of CO₂ gas (e.g., bicarbonate buffered solution, 100 kPa of CO₂).¹⁶ Because of low substrate CO₂ availability, there is a ceiling on achievable steady-state CO₂ reduction rates.^{16,21} Further, the low CO₂ solubility and sluggish kinetics of CO₂ reduction,²² combined with high H⁺ availability, often contribute to direct H₂ evolution, leading to low Faradaic yields of carbon-containing products. A variety of strategies are

being pursued to alleviate CO₂ starvation at electrode surfaces. These include the development of structurally complex gas-diffusion electrodes for use in flow cells^{23,24} polymer electrolytes^{25,26} and ionic liquids²⁷ that leverage tailored electrode-contacting phases to favor high CO₂ availability. In some cases, these approaches rely on sensitive interfacial phenomena²⁸ and involve preparation of membrane-electrode assemblies. Alternatively, supercritical CO₂ (scCO₂) has been investigated for CO₂ reduction electrocatalysis.^{29,30} However, scCO₂ is a poor conductor and, even upon pairing with co-solvents, the solubility of supporting electrolytes is too low (≤ 35 mM) to facilitate high current densities and Faradaic efficiencies.³¹⁻³⁴ Furthermore, the high operating pressures needed to achieve supercritical conditions (> 7.38 MPa) pose practical challenges and increase costs. Development of new reaction media could help in overcoming these challenges by enabling (1) high CO₂ concentrations at modest pressures, (2) sufficient conductivity to engender rapid electron-transfer, (3) high mass transfer rates of CO₂ to the electrode surface, and (4) controlled proton (H⁺) concentrations that may disfavor parasitic hydrogen evolution. To address these needs, we now report the development and use of new CO₂-rich electrolytes for electrochemistry and electrocatalysis. Nonaqueous electrochemical studies³⁵ and molecular electrocatalysis of CO₂ reduction³⁶ are commonly conducted in acetonitrile solvent at near-ambient CO₂ pressure with the supporting electrolyte tetrabutylammonium hexafluorophosphate (TBAPF₆). However, it is known from the reported binary phase behavior of the CO₂/acetonitrile system that multimolar CO₂ concentrations can be attained at 298 K at relatively mild pressures (1.5-5 MPa).^{37,38} Here, we have exploited this phase behavior to achieve high liquid-phase CO₂ concentrations (up to ca. 15 M) in solutions containing TBAPF₆, such that the liquid phase retains sufficient conductivity for effective electrochemistry and electrocatalysis. Using a polycrystalline gold electrode, we observe up to an order of magnitude enhancement in the CO₂ conversion rate in these new media compare to that observed at near-ambient pressure. Our results suggest that these previously unexplored media enhance CO₂ conversion by alleviating the longstanding challenge of substrate starvation near an electrode-catalyst.

3.3 Experimental

3.3.1 General considerations

All manipulations were carried out in dry, N₂ filled gloveboxes (Vacuum Atmospheres Co., Hawthorne, CA) or under an Ar atmosphere in a glovebag (NPS Corp., Spilfyter) unless otherwise noted. All solvents were of commercial grade and dried over activated alumina using a PPT Glass Contour (Nashua, NH) solvent purification system prior to use, degassed and then stored over molecular sieves. All chemicals used were from major suppliers and used after extensive drying.

3.3.2 Vapor-liquid equilibrium (VLE) studies

Initial volumetric studies were conducted with a Jerguson view cell under isothermal conditions using a thermostatic water bath. In these experiments, changes in liquid volume were measured with a Digimatic Height Gauge (Mitutoyo). For quantitative measurements of [CO₂] in liquid phases, VLE studies were carried out in a custom-built apparatus reported by Ren and Scurto.³⁹ Briefly, an Isco 100 DM syringe pump held at constant temperature and pressure was used to transfer a known volume of CO₂ into a custom high-pressure view cell held at constant temperature through stainless steel lines held at constant temperature and pressure. The data were acquired with Labview 8.2 software and analyzed using data from the REFPROP database (v 8.0) in Microsoft Excel.

3.3.3 Electronic absorption spectroscopy

UV-visible spectroscopy experiments were carried out in a 50-mL stainless-steel reactor (Parr Instrument Co.) equipped with a pressure transducer and a high-pressure, 1-cm path length view cell equipped with sapphire windows. The homogeneous mixture in the reactor was circulated with a micro circulation pump (Micropump Co., U.S.A.) and measurements taken at various CO₂ pressures with a USB 2000+ UV-vis spectrometer with DH-2000 deuterium-halogen light source (Ocean Optics Inc., Dunedin, Florida).

3.3.4 Electrochemical experiments

All electrochemical experiments were conducted in a 50-mL reactor (Parr Instrument Co.) equipped with a custom-machined lid outfitted with gas-tight electrical leads as well as a tem-

perature probe and pressure transducer (sensitivity ± 50 kPa). The temperature and pressure remained stable across the time course of all experiments (temperature 25 ± 0.05 °C, \pm pressure 14 kPa). The supporting electrolyte used was 0.4 M tetra(n-butylammonium) hexafluorophosphate (TBAPF₆; Oakwood Chemical Co.) prior to expansion. Measurements were made with a Gamry Reference 3000 Potentiostat/Galvanostat using a standard three-electrode configuration. In all pressurized electrochemical experiments, by virtue of the construction of our high-pressure cell, ferrocene was included as an internal standard. No noticeable shift in the position of the internal standard relative to the reference electrode was observed over the time course of bulk electrolysis experiments (Figures 3.11 and 3.12).

Experiments to interrogate CO₂ reduction were carried with either a 200 μ m diameter gold microelectrode ($A = 0.0003$ cm²) or with a coil of 0.1mm gold wire ($A = 1.16$ cm²) (Alfa Aesar, 99.95%). Gold working electrodes were cleaned between experiments by soaking in hydrogen peroxide (52%) for one hour then rinsed with acetone and dried.

Experiments to examine the electrochemical properties of metallocenes were conducted with the basal plane of highly oriented pyrolytic graphite (HOPG) (GraphiteStore.com, Buffalo Grove, Ill.; $A = 0.09$ cm²). A copper wire (Alfa Aesar, 99.9%, 1.5mm diameter) immersed in electrolyte was used as a pseudo-reference in these experiments and stored in a separate, fritted chamber (Vycor frit, Bioanalytical Systems, Inc.) from the working solution. The counter electrode in all experiments was a platinum wire (Kurt J. Lesker, Jefferson Hills, PA; 99.99%, 0.5 mm diameter). Electrolyte containing ferrocene was loaded into the electrochemical reactor under an argon atmosphere in a glovebag. Prior to experiments, the reactor was purged three times by repeated pressurization and depressurization cycles (ca. 800 kPa to 200 kPa) to exclude trace water and oxygen from the system. To achieve liquid expansion, the reactor was brought to the required pressure, stirred only until equilibrium was established, and then closed off from the gas supply. Electrolyte was quiescent during all electrochemical measurements.

3.3.5 Sample preparation for gas chromatography

Following electrolysis, gas contained within both the expanded liquid and reactor headspace was collected by expansion of the headspace into an evacuated steel cylinder. At low pressures (<0.5 MPa), a 40 mL vessel was used and at high pressures a 1 L vessel was used. The connection

of the larger volume reverses the expansion of the liquid due to the drop in pressure to near-ambient (typically 100-900 kPa) pressures. This method allows for a gas sample to be taken that is representative of all gas present in the system. The pressure and temperature of the system were allowed to equilibrate before closing the connection and removing the cylinder for analysis.

3.3.6 Product detection by gas chromatography

Analysis of gas samples was performed with a Shimadzu GC-2014 Custom-GC gas chromatograph with a thermal conductivity detector and dual flame-ionization detectors. A custom set of 8 columns and timed valves enable quantitative analysis of the following gases: hydrogen, nitrogen, oxygen, carbon dioxide, carbon monoxide, methane, ethane, ethylene, and ethyne. Argon serves as the carrier gas. The instrument was calibrated prior to experimental runs with a standard checkout gas mixture (Agilent 5190-0519) to obtain qualitative information regarding detection of H₂ and CO. Calibration curves over a range of 100–10,000 ppm for H₂ and 90–9,000 ppm for CO were constructed with prepared mixtures of H₂ or CO in N₂ to enable quantitative measurements. Quantification was accomplished using gas handling that accounts for sample dilution during post-electrolysis gas collection. These methods were carried out assuming that all gases involved behave as ideal gases. This is a reasonable assumption, as the pressure of the system at all times during these manipulations was < 900 kPa. Analysis of the liquid phase was achieved by injection of a sample of the electrolyte following electrolysis into an Agilent 6890 Gas Chromatograph fitted with a CP-Wax 58 (FFAP) CB column. The sample was filtered over silica to remove excess electrolyte and then analysis carried out with the FID detector on the instrument.

3.4 Results and Discussion

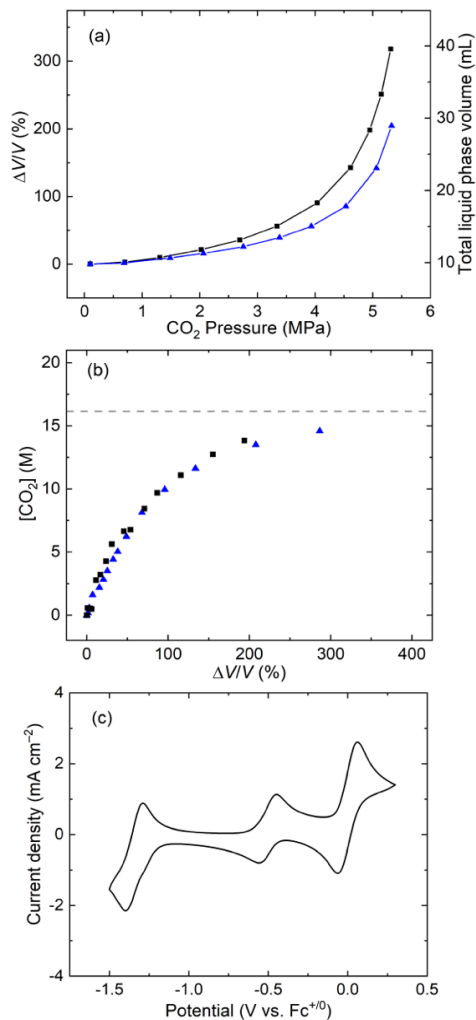


Figure 3.1. CO_2 expansion of electrolytes. (a) Change in volume of a 10 mL sample of MeCN (black) and MeCN initially containing 0.4 M TBAPF₆ (blue) upon CO_2 pressurization. (b) Increasing CO_2 concentration as the volume expands with increasing pressure. MeCN (black) and MeCN initially containing 0.4 M TBAPF₆ (blue). The CO_2 concentration in the expanded liquid asymptotically approaches the concentration of liquid CO_2 (gray dashed line). (c) Cyclic voltammetry of metallocene complexes in CO_2 -expanded electrolyte solution (3.18 MPa CO_2). 0.4 M TBAPF₆ present in acetonitrile prior to expansion. Redox couples of ferrocene ($E_{p,1/2} = 0$ V), decamethylferrocene ($E_{p,1/2} = -0.5$ V) and cobaltocene ($E_{p,1/2} = -1.34$ V) shown. Working electrode was the basal plane of highly-oriented pyrolytic graphite (HOPG, 0.09 cm²).

At the relatively mild pressures mentioned above (1.5-5 MPa), the mild critical properties of CO₂ (T_c = 304.1 K; P_c = 7.38 MPa) drive an exponential increase in liquid-phase CO₂ solubility with pressure in organic solvents such as acetonitrile, resulting in high CO₂ concentrations as well as volumetric expansion of the liquid phase by nearly threefold at 5 MPa.^{40–42} And, while the pressure-tunable properties of these media have been exploited in chemocatalysis in a variety of ways,^{43,44} the enhanced CO₂ solubility in such media has not been previously harnessed to enhance organic electrocatalysis of CO₂ conversion. In order to develop an electrochemical system that leverages non-linear increases in liquid phase CO₂ concentration with pressure, we first set out to determine if acetonitrile containing supporting electrolyte remains homogeneous upon isothermal (298 K) volumetric expansion with CO₂. We confirmed that TBAPF₆ at an initial concentration of 0.4 M in acetonitrile remains dissolved up to CO₂ pressures of 5.3 MPa, corresponding to a volumetric expansion of ca. 300 percent (Figures 1a and 1b).

Thus, acetonitrile can simultaneously support high concentrations of liquid-phase CO₂ and supporting electrolyte. Related quantitative electronic absorption measurements with Re(CO)₃(bpy)NCMePF₆ as a soluble chromophore confirm both the homogeneity and volumetric expansion characteristics of this electrolyte system. (See ESI for details.) We term this continuum of pressure-tunable CO₂-eXpanded Electrolytes as “CXEs,” as these solutions support enhanced CO₂ concentrations and transport properties for performing electroanalytical and electrocatalytic studies. Quantitative vapor-liquid equilibrium (VLE) data provide a direct measure of the concentration of dissolved CO₂ as a function of pressure, and reveal that CXEs manifest a similar relationship between liquid-phase CO₂ mole fraction and pressure (Figure 1b) as CO₂-expanded acetonitrile.³⁹ In accord with the notion that near-critical CO₂ can readily dissolve in acetonitrile, but not in the TBAPF₆, CXEs can be considered to be a pseudo-binary CO₂/acetonitrile system because of the relatively small concentrations of the supporting electrolyte in the liquid phase and virtually no electrolyte in the gas phase. Appealingly, the liquid-phase CO₂ concentration in CXEs reaches approximately 12 M at 5 MPa, approaching that of neat liquid CO₂ (16.1 M; dashed line in Figure 1b) at identical pressure and temperature.⁴¹ In contrast, aqueous systems at ambient temperature can only support CO₂ concentrations of ca. 0.8 M at ca. 5 MPa CO₂ pressure.⁴⁵

These phase behavior studies provide reliable knowledge of the preferred operating conditions for performing electrochemical reactions in CXEs and thereby guide reactor design. A high-pressure

reaction vessel (Parr Instrument Co.) was fitted with a custom cap featuring ports for multiple electrodes that enable electrochemical experiments to be carried out. Additional ports for gas transfer, and a mechanical stirrer were also included (see ESI for details). We first measured the approximate thermodynamic potentials in CXEs for common redox reagents. Specifically, we adopted the 1e⁻ ferrocenium/ferrocene redox couple (denoted hereafter as Fc^{+ / 0}) as our reference potential, in line with most electrochemical work in acetonitrile.^{46,47} Using cyclic voltammetry, we measured the midpoint potentials for the cobaltocenium/cobaltocene couple at -1.34 V vs. Fc^{+ / 0} and for the decamethylferrocene/decamethylferrocenium couple at -0.5 V vs. Fc^{+ / 0} at 3.18 MPa (Figure 1c). These results compare well with literature values for the reversible potentials of these metallocenes in acetonitrile (-1.33 V and -0.48 V, respectively), demonstrating that the CO₂-expanded acetonitrile medium behaves similarly to common organic solvents.⁴⁸ Scan rate-dependent studies of the voltammetry confirm that both the oxidized and reduced forms of these compounds are dissolved and freely diffusing in the liquid phase; these results are confirmed by in situ UV-visible spectra collected on ferrocene in CXEs (see ESI for details).³⁴ Cyclic voltammetry carried out with solutions containing cobaltocene, decamethylferrocene, and ferrocene across the 0-5 MPa range indicates that the midpoint potentials of the other metallocenes with respect to the ferrocenium\ferrocene couple are essentially invariant (see ESI). While we did observe a slight

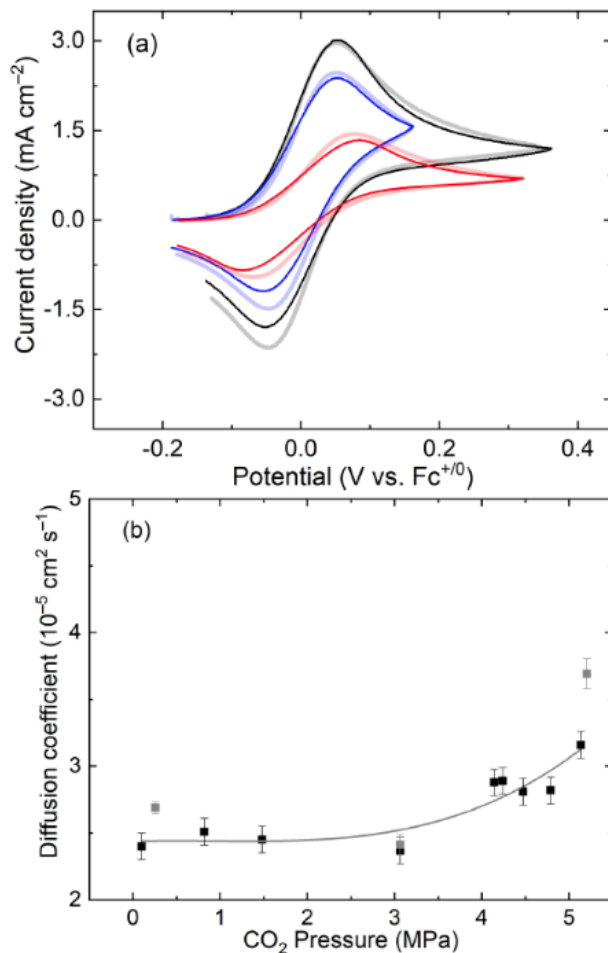


Figure 3.2. Cyclic voltammetry of the $\text{Fc}^{+/0}$ redox couple and extracted experimental diffusivities as a function of CO_2 pressure in CXEs. (a) Experimental (solid dark lines) and simulated (transparent shade lines) cyclic voltammetry of ferrocene conducted under various CO_2 pressures at 25 °C. Black: 0.79 MPa of CO_2 . Blue: 3.2 MPa of CO_2 . Red: 5.2 MPa CO_2 . Working electrode was the basal plane of highly-oriented pyrolytic graphite (HOPG, 0.09 cm²). Scan rate 100 mV/s. (b) Diffusion coefficients of ferrocene as obtained from the cyclic voltammetry data as a function of CO_2 pressure. Error bars were calculated directly from experimental data for gray points, and from variance in low-pressure curve fits for black points. Black: Obtained from simulation of voltammetry. Gray: Determined experimentally via double-step chronoamperometry. The gray line is only intended to guide the eye.

inhibition in the electron-transfer rate kinetics (as estimated from the peak-to-peak separations, ΔE_p), CXE media are still able to support fast electron transfer even at the highest pressures. This is notable, because the liquid phase concentration of CO_2 at 5 MPa is ca. 12 M. In line with these findings, measurement of the solution resistance as a function of pressure at our graphite working electrode show an increase at the highest pressures (see ESI), consistent with significant dissolution of CO_2 . However, these studies also confirm that the TBAPF₆ remains dissociated in the electrolyte and continues to function as an effective ionic conductor at our higher pressures. An advantage of utilizing gas-expanded liquid media in chemocatalysis is improved mass transfer rates in comparison to neat organic solvents.⁴⁰ Therefore, we anticipated that CXEs might engender enhanced diffusion rates to/from the electrode surface. To investigate this possibility, we performed voltammetry on the $\text{Fc}^{+/0}$ redox couple as a function of CO_2 pressure, and simulated the experimental current-voltage curves using COMSOL Multiphysics simulation software (see the SI for details). Diffusion coefficients were extracted from simulations of the experimental data, which were optimized by holding concentration and scan rate constant and numerically optimizing the simulated curves over the full data set. The experimental and simulated voltammograms show good agreement (Figure 2a), confirming that the conventional equations that govern organic electrochemistry are valid in CXE media.^{49,50} Importantly, we find that the diffusion coefficient of ferrocene (shown in Figure 2b) is pressure-tunable in CXEs. Specifically, the diffusivity of ferrocene increases from $2.4 \times 10^{-5} \text{ cm}^2 \text{ s}^{-1}$ in pure acetonitrile (in agreement with prior work^{51,52}) to $3.16 \times 10^{-5} \text{ cm}^2 \text{ s}^{-1}$ in CXE at 5.1 MPa CO_2 pressure (Figure 2b). Direct determination of diffusion coefficients from double-step chronoamperometry experiments follow the same pressure-dependent trend as the simulated values.⁵³ This increase in diffusivity, in accord with prior computational modeling,³⁶ can be rationalized by the decreased liquid-phase viscosity caused by dissolution of the gas-like CO_2 molecules at near-critical pressures.^{54,55} Thus, in addition to increasing enhanced CO_2 availability, the use of CXEs can modestly augment the rate of substrate delivery to the electrode-catalyst surface. With these fundamental characterizations in hand, we moved to investigate CO_2 electroreduction in CXEs as a function of CO_2 pressure. Polycrystalline gold was chosen as the electrode material for this study, as it is known to selectively produce CO from CO_2 under a variety of conditions, including with acetonitrile as solvent⁵⁶ Cyclic voltammetry carried out on a polycrystalline gold microelectrode ($A = 0.031 \text{ mm}^2$) in contact with acetonitrile solution containing 0.4

M TBAPF₆ under a headspace CO₂ pressure of 300 kPa (ca. 3atm) shows onset of an irreversible catalytic response near -2.5 V vs. Fc^{+ / 0}, consistent with prior results (Figure 3a). Notably, we observe a plateau in the voltammogram, indicative of significant CO₂ depletion at the electrode surface and onset of a diffusion-limited regime at ca. -2.74 V.³⁴ Under CXE conditions, we observe enhancement of the catalytic current as the CO₂ pressure is increased, reaching a maximum at ca. 3.2 MPa. The voltammogram shape is typical for a robust catalytic response, with little hysteresis on the return, anodic sweep. This suggests enhanced replenishment of substrate near the electrode due to the increased CO₂ concentration in the liquid phase. Consistent with this hypothesis, the current does not exhibit a plateau region as observed at near-ambient pressures, providing further evidence that diffusion limitations are alleviated in CXEs. Indeed, this response is indicative of an increased rate of catalysis as the electrode is polarized to increasing driving force, much like that observed for H⁺ reduction to H₂ in acidic water.⁵⁷ The current-voltage profile is also consistent with insignificant electrode poisoning or product inhibition on the voltammetric timescale. For a typical electrocatalytic process, the catalytic current is expected to increase linearly with substrate concentration up to a maximum, plateauing value.⁵⁸ However, we observe a maximum in the electrocatalytic current with increasing CO₂ pressures. Interestingly, the CO₂ conversion rate (i.e., current density) decreases at CO₂ pressures beyond ca. 3.2 MPa, trending back toward the modest values measured at near-ambient CO₂ pressures (Figure 3b). However, the voltammetric responses

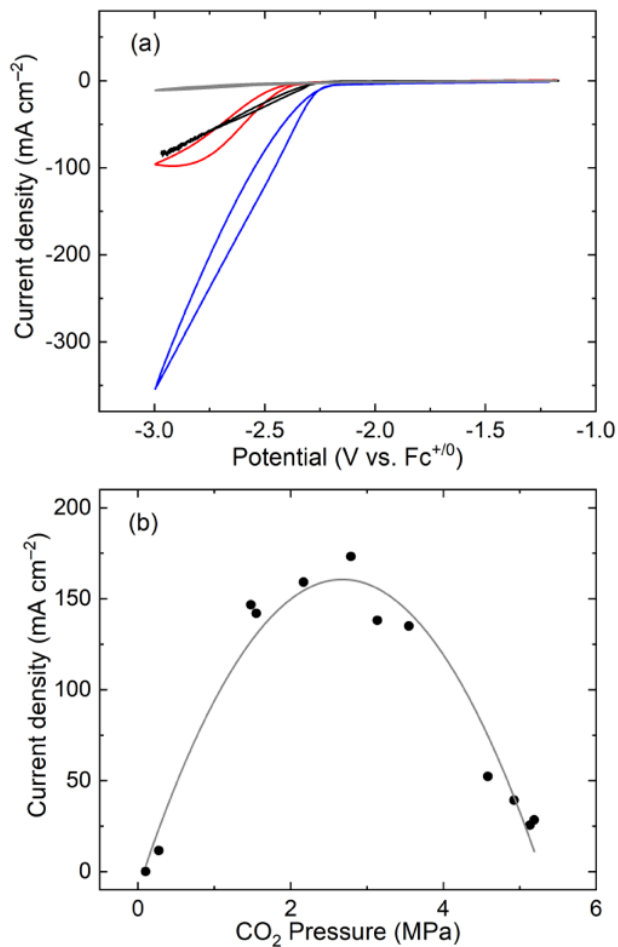


Figure 3.3. Electrochemical current response as a function of potential and pressure in CXE media. (a) Cyclic voltammetry conducted under varying pressures of CO₂ (Red: 0.3 MPa; Blue: 3.2 MPa; Black: 5.2 MPa; Gray: Control under 0.3 MPa of Ar gas). Au disk microelectrode; A = 0.031 mm²; scan rate: 100 mV/s. (b) Steady-state currents with the same electrode at -2.5 V as a function of CO₂ pressure. Following initial agitation to achieve equilibrium CO₂ dissolution in the electrolyte phase, solution was quiescent during the cyclic voltammetry experiments. The gray line is parabolic and intended only to guide the eye.

obtained at the highest pressures (for example, 5.2 MPa) show a unique shape when compared to data obtained at 300 kPa (Figure 3a). Specifically, the response is very sharp, showing virtually no hysteresis—indicating a resistor-like behavior. Thus, although the current densities are similar, the nature of the factors controlling charge transfer at 5.2 MPa appears to be different than those observed at near-ambient pressures. Further, much like at 3.2 MPa, substrate mass-transport is not limiting, as no plateauing currents are observed. Consistent with the resistive appearance of the voltammetry at 5.2 MPa, measurement of the solution resistance with the gold working electrode shows an increase at the highest pressures (ca. 2600 Ω at 0.3 MPa vs. ca. 12,700 Ω at 5.1 MPa) (see ESI, Figure S6). Similar to the case of the graphite electrode, decreased polarity of the electrolyte due to the high liquid-phase concentration of CO₂ (11.7 M at 5.1 MPa) results in the measured increase in solution resistance. Thus, the interplay of (i) increased substrate CO₂ availability and (ii) decreased solvent polarity results in a non-monotonic dependence of catalytic rate on CO₂ concentration. Notably, the modest improvement in mass transport (*vide supra*) is not directly observed in catalytic performance, due to the interference of increased solution resistance.

Bulk electrolysis experiments with a gold coil working electrode ($A = 1.2 \text{ cm}^2$) were carried out to confirm the production of CO and examine the possibility of formation of other, unexpected reduction products (Figure 4a). Quantitative gas chromatography shows that CO is the major gaseous product with an estimated Faradaic efficiency of ca. 40 percent at 0.3 MPa CO₂ pressure and 80 percent at 3.2 MPa CO₂ pressure (Figure 3.4b, See ESI for details). H₂ was detected following electrolysis at 0.3 MPa, corresponding to a Faradaic efficiency of ca. 5 percent. Remarkably, no H₂ could be detected following electrolysis at the optimum pressure of 3.2 MPa (see ESI for details). In line with the reasonably high faradaic yield of CO, no liquid-phase products were detected by GC analysis. CO₂ reduction to CO is thus clearly enhanced by an order of magnitude at 3.2 MPa, in terms of steady-state current density (12 mA cm⁻² at 0.27 MPa vs. 138 mA cm⁻² at 3.2 MPa; $E_{\text{app}} = -2.5 \text{ V}$). The modest deficit of detected product CO (≤ 20 percent of

charge passed at 3.2 MPa) could arise from cyclic ferrocenium/ferrocene electron transfer occurring in our one-compartment reactor. In such a pathway, ferrocene oxidized at the counter electrode (anode) could migrate to the working electrode (cathode) and be promptly reduced under electrocatalytic conditions. However, we note that gold is commonly found to produce ca. 80 percent faradaic yield of CO with organic electrolytes.⁵⁵ Additionally, the primary anodic half-reaction occurring during electrolysis is likely not ferrocene oxidation, as the concentration of ferrocene in the working solution (≤ 3 mM) is insufficient to support the current densities measured. Thus, we anticipate that hexafluorophosphate anion or acetonitrile may be serving as sacrificial reductant. Mass balance dictates that cathodic CO production should initially generate an equivalent of O_2^- . Often, explicit inclusion of protic compounds provide equivalents of protons that serve to assist in co-generation of H_2O with CO.⁵⁹ Under our conditions, prior work suggests that omission of an acidic additive leads, initially, to formation of CO_3^{2-} .⁶⁰ However, tetrabutylammonium is known to undergo Hofmann degradation upon exposure to the strongly basic conditions present at the cathode. The net result of this reactivity is known to result in opportunistic scavenging of protons from tetrabutylammonium.⁶¹ Products of Hofmann degradation of TBAPF_6 under our conditions should thus include butene, tributylamine and bicarbonate. However, tributylamine and bicarbonate are not detected by GC analysis, suggesting that these species are likely unstable during prolonged electrolysis in CXEs. In accord with the voltammetry results, time-dependent measurements of CO production and Faradaic efficiency show that the system is stable over at least eight hours. At near-ambient CO_2 pressures, the rate of CO production is ca. $70 \mu\text{L/h}$ (volumes measured at ambient pressure); at 3.2 MPa, the rate of CO production increases by one order of magnitude to ca. $700 \mu\text{L/h}$. This result mirrors the one order of magnitude increase in the current density between 0.3 MPa and 3.2 MPa as measured in the voltammetry experiment (Figure 3b), and confirms that the minor variations observed across chronoamperometric experiments do not affect the yield of CO. At higher CO_2 pressures, the CO production rate markedly decreases to levels observed at near-ambient pressures. The resulting volcano-shaped profile (Figure 4c) reveals that the pressure-tunable properties of CXEs can be used to maximize the rate and efficiency of CO_2 electroreduction. As our findings suggest that use of very high pressures does not provide the highest catalytic turnover rate, energy costs may be saved by judicious selection of operational pressure in practical reactors. Moreover, the occurrence of maximum catalytic rates at relatively mild

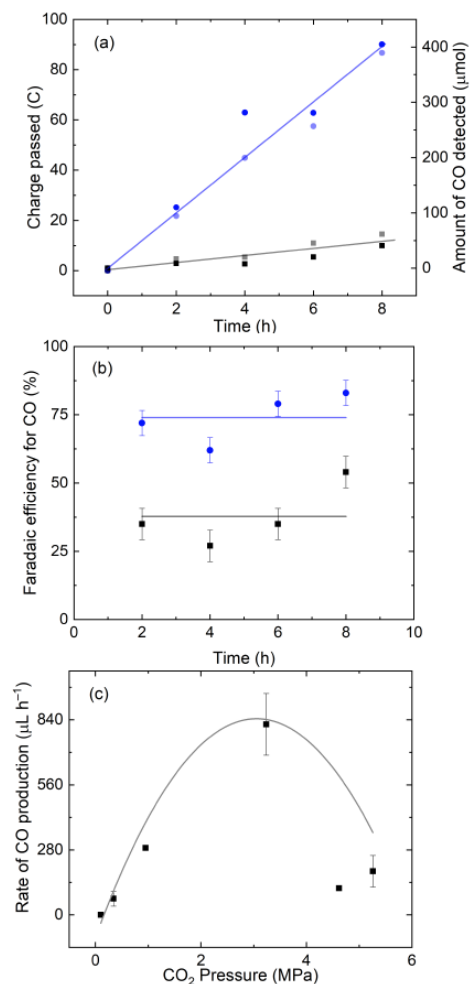


Figure 3.4. Enhancement of electrochemical CO₂ reduction in CXE media. (a) Plot of charge passed and CO detected by gas chromatography for different bulk electrolysis times, using a 1.2 cm² Au coil electrode. Dark circles represent charge passed in coulombs and light circles CO detected in μmol under 3.2 MPa CO₂ (blue) and 0.3 MPa CO₂ (black). (b) Faradaic efficiency following various bulk electrolysis times with respect to CO detected. Error bars are calculated based on replicate experiments across the full pressure range. Blue: 3.2 MPa CO₂. Black: 0.3 MPa CO₂. Lines shown are linear fits, assuming efficiency for CO production remains constant with time. (c) Pressure dependence of CO formation following bulk electrolysis for 8 h. Gray line is parabolic and intended only to guide the eye. The electrolysis experiments were performed at -2.5 V vs Fc^{+ / 0} without stirring.

pressure (3.2 MPa) should favor CXE process economics. The observation of an optimal, order-of-magnitude increase in the pressure-dependent catalytic CO₂ reduction rate was thus confirmed by measurements of both current flow and CO production. Significant increases in the liquid-phase CO₂ concentration result in a balance between (i) enhanced substrate CO₂ availability (enhancing performance) and (ii) decreased solvent polarity (diminishing performance) (see ESI, Figure S25). However, we note that measurements of solution resistance show significantly higher values for the gold electrodes than for the carbon electrodes. Thus, we anticipate that the nature of the interface between CXEs and solid electrodes is dependent upon the identity of the chosen electrode material. Thus, our future efforts are focused on understanding these electrode- and media-dependent effects in greater detail, including approaches based on modeling and use of impedance spectroscopy.

Conclusions

Here, we have demonstrated that forming CXEs with acetonitrile at modest CO₂ pressures (≤ 3.2 MPa) vastly improves substrate availability and results in up to an order of magnitude improvement in the rate of CO₂ conversion compared to those measured at near-ambient conditions. Modest improvements to mass transport rates can also be achieved through use of CXEs. Based on these findings, we anticipate that CXEs may not only unlock the potential of conventional electrocatalysts that may have been considered insufficiently active in prior studies, but also open opportunities in design of catalysts that can take advantage of high substrate concentrations. Such advances could help realize practically viable electrochemical processes for CO₂ conversion powered by renewable energy.

3.5 Acknowledgement of Contributions

Expansion Data was taken with help from Tyler Kerr. VLE data was taken by Tyler Kerr. Electrochemical experiments were performed with help from Tyler Kerr and David Sconyers. Gas chromatography was done by David Sconyers. UV-Vis data was taken by Hyun-Jinn Lee.

3.6 Supporting Information

3.6.1 Reactor Design for Studies Involving CO₂-Expanded Electrolytes

Our group has designed a high-pressure electrochemical reactor cell to conduct the electrochemistry experiments described in this report. The reaction vessel itself is composed of a 50-mL reactor (Parr) lined with a Teflon insert rated to a maximum pressure of 20.7 MPa and a maximum temperature of 350°C. A magnetically coupled drive (Parr Instrument Co.) is used to provide agitation in the solution to speed equilibration or enhance mass transport to the electrodes. A custom-machined reactor cap features seven threaded ports and an O-ring seal (PTFE, Parr) that makes contact at the periphery of the cap to the reactor body. During use, the reactor cap is clamped to the reactor with a split-ring cover clamp (Parr Instrument Co.). Seven threaded ports in the reactor cap interface four electrical connections, gas inlet and outlet valves, thermocouple and pressure transducer connections, and a sampling port with the inner volume of the reactor. An emergency pressure release valve is connected to the gas-sampling port, to avoid over-pressurization of the reactor during operation. The thermocouple extends below the liquid-gas interface to achieve accurate electrolyte temperature determination. Thermostatic control during experiments is achieved with a recirculating heater/chiller (Fisher Scientific). Reactor pressurization was carried out with high-pressure CO₂ gas from a commercial cylinder (Matheson, Research Grade CO₂, 99.999%, 5.52 MPa). A high-pressure two-stage manifold (Matheson) and needle valve (Swagelok) are used to control input gas pressure and flow rate. A check valve prevents solvent contamination of the gas cylinder. The electrical feedthroughs (CeramTec) for the electrode connections are rated to 27.6 MPa, and are composed of an inner conducting copper lead interfaced with an outer ceramic body. The electrodes are then attached to the copper leads using gold plated clips. (Figure 3.5 and 3.6)

Reactor Performance for Electrochemical Experiments

To confirm that the custom built reactor was suitable for electrochemical experiments a series of experiments was carried out. Figure 3.7 shows the pressure stability of the reactor over time, while Figure 3.8 shows the temperature stability of the reactor.

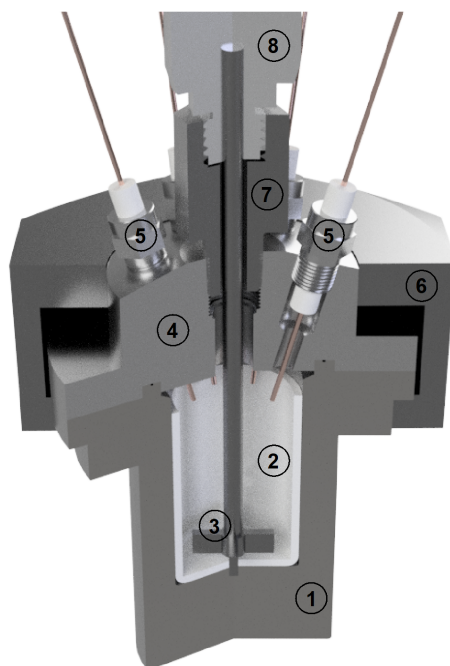


Figure 3.5. CAD drawing of reactor vessel. (1) 50 mL Parr reaction vessel. (2) Teflon liner. (3) Stir Rod. (4) Custom reactor cap with PTFE O-ring seal. (5) Ceramtec electrical feedthrough. (6) Split-ring clamp. (7) Magnetic drive adaptor. (8) Parr magnetic drive.

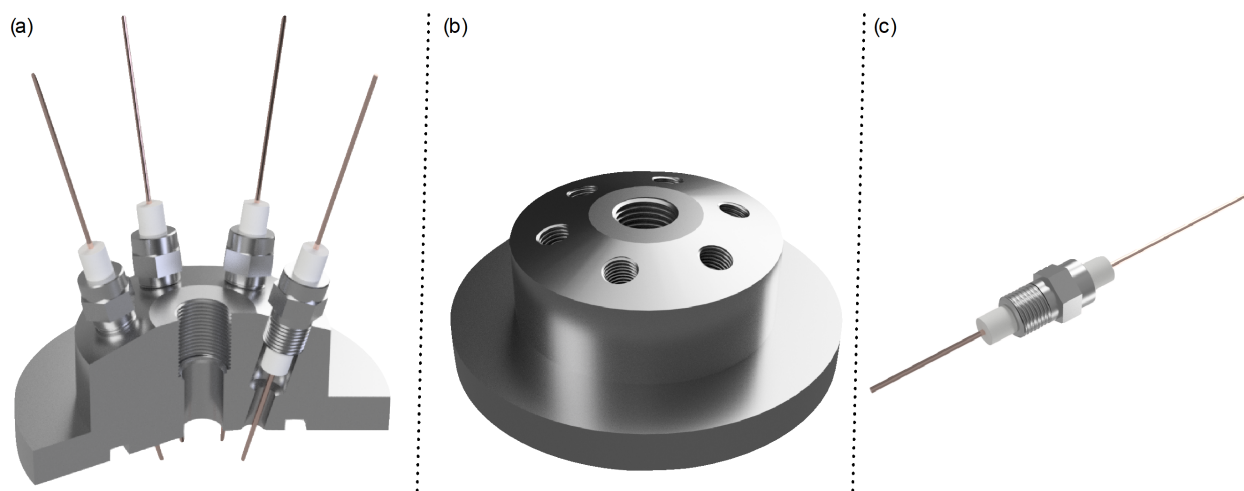


Figure 3.6. CAD drawings of cap assembly. (a) Assembled cap with feedthroughs. (b) Custom cap. (c) Ceramtec electrical feedthrough.

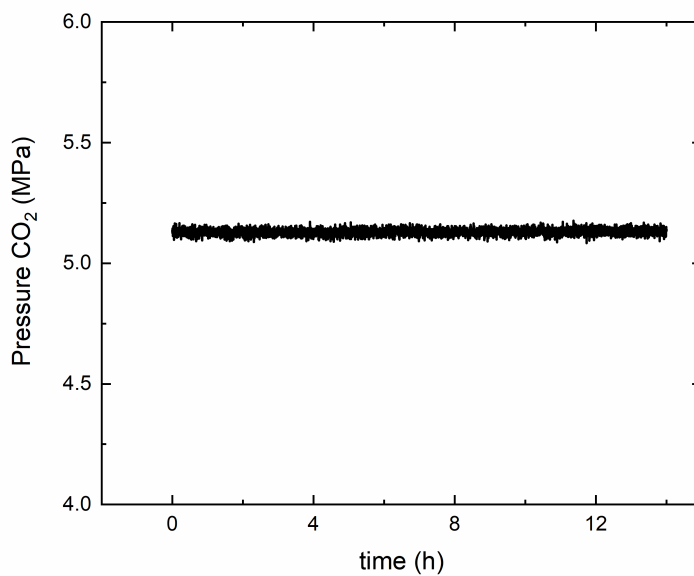


Figure 3.7. Pressure stability within reactor over time. Plot showing low pressure variance within the reactor (± 50 kPa) over a period of over twelve hours

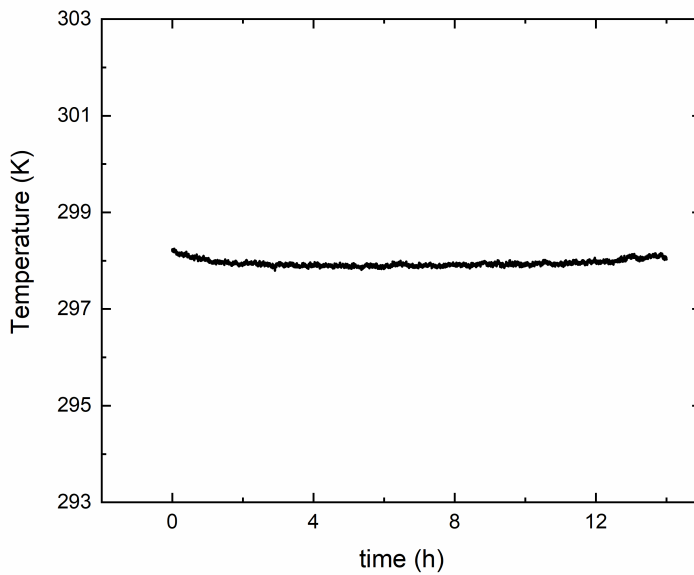


Figure 3.8. Temperature stability within reactor over time. Plot showing low temperature variance within the reactor (± 0.2 K) over a period of over twelve hours.

3.6.2 Supporting Electrochemical Experiments

As GXEs have not been previously characterized for electrochemistry, numerous supporting experiments were carried out to both characterize the system and ensure its suitability for electrochemical experiments.

Figures 3.9 and 3.10 show data from a series of experiments designed to test the electrical conductivity of the system. For a carbon electrode ($A=0.09\text{ cm}^2$) a slight increase of resistance is observed. In contrast, the resistance of the system to gold increases at an exponential rate. The precise mechanism for this startling change in resistance, particularly in light of the carbon data, is unknown. It is possible that the adsorption of CO_2 on gold creates an insulating surface. Further research is necessary to understand this phenomenon more fully.

Figures 3.11, 3.12, 3.13 and 3.14 show data to confirm that the electrochemical properties for a series of model metallocene compounds do not change with the expansion of the acetonitrile base solvent. Figures 3.11 and 3.12 show that the midpoint potentials do not change. Figures 3.13 and 3.14 show that the current dependence upon scan rate for decamethyl ferrocene is also unaffected by expansion. The lack of change suggests that the electrochemical properties of the acetonitrile are still dominant in GXEs.

The necessity of excluding water from the system forces reliance upon a pseudoreference electrode. In Figure 3.15 the potential of the ferrocene couple against the pseudoreference electrode is shown to be essentially invariant, proving the stability and suitability of the reference for electrocatalytic experiments.

The increase in the catalysis for the optimum pressure is shown in Figure 3.16 where the blue chronoamperometry curve at 3.2 MPa of CO_2 is much greater than the curves at both ambient and 5.1 MPa CO_2 . The individual curves for the unexpanded and optimum pressure in Figure 3.16 are shown in Figures 3.19 and 3.20.

In addition to the product detection chronoamperometry experiments, to confirm that cyclic voltammetry was not being overly affected by transient effects a series of chronoamperograms were taken at varying potentials at the main pressures. In Figure 3.17 the steady state current is plotted against the transient CV current and shows good agreement. In Figure 3.18 a representative set of these chronoamperograms is shown.

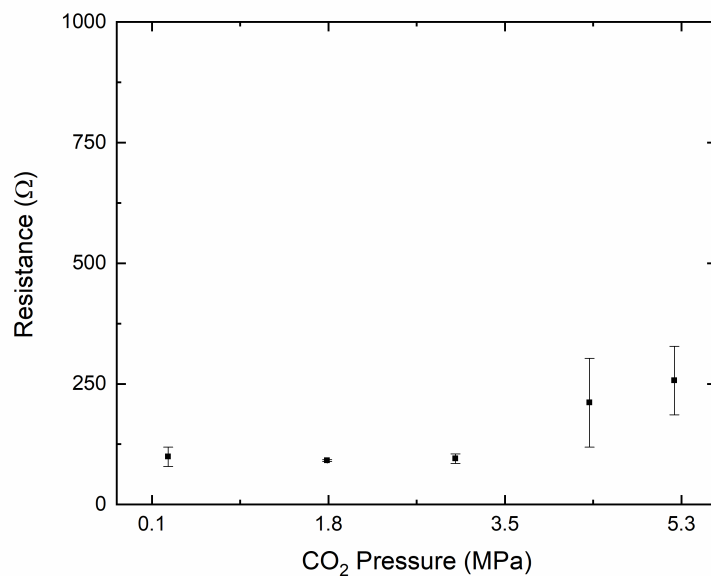


Figure 3.9. Measurements of solution resistance as a function of pressure on carbon. Data were collected with a commercial script provided with the potentiostat; this script relies on controlled-potential electrochemical impedance spectroscopy (EIS) to determine the solution resistance by interpreting collected data using a model circuit. The data points shown are average values collected on an HOPG working electrode ($A = 0.09 \text{ cm}^2$) across quadruplicate measurements at four different potentials (-0.2 V , -0.5 V , -0.9 V and -1.2 V vs. $\text{Fc}^{+/0}$). Thus each data point and error represents sixteen unique measurements. Error bars are shown as $\pm 1\sigma$

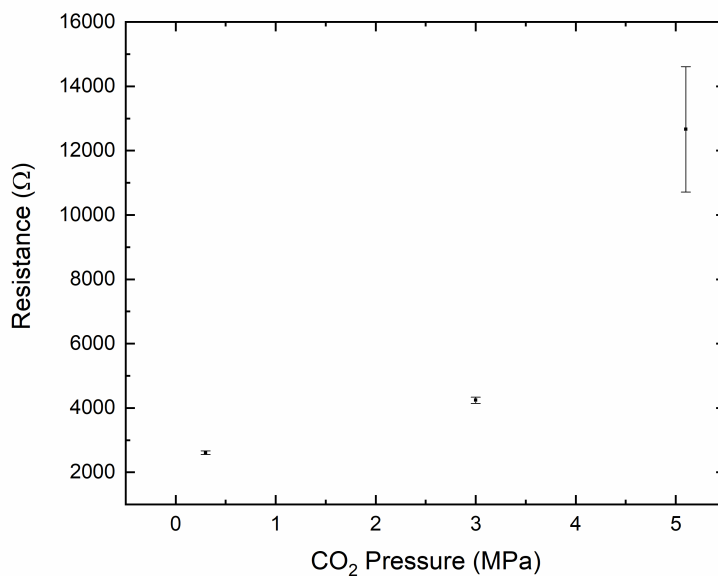


Figure 3.10. Measurements of solution resistance as a function of pressure on gold. Data were collected with a commercial script provided with the potentiostat; this script relies on controlled-potential electrochemical impedance spectroscopy (EIS) to determine the solution resistance by interpreting collected data using a model circuit. The data points shown are average values collected on an gold working microelectrode ($A = 0.031 \text{ mm}^2$) across quadruplicate measurements at four different potentials (-0.2 V , -0.5 V , -0.9 V and -1.2 V vs. $\text{Fc}^{+/0}$). Thus each data point and error represents sixteen unique measurements. Error bars are shown as $\pm 1\sigma$

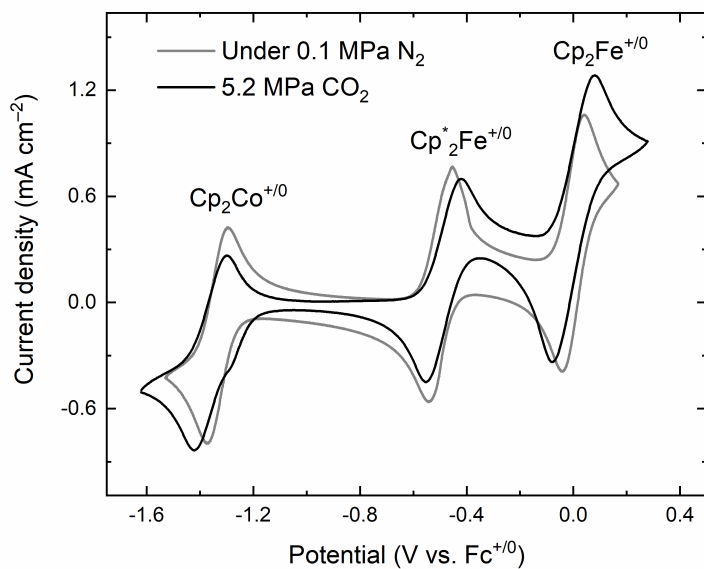


Figure 3.11. Cyclic voltammetry of metallocenes at ambient and high pressures. Cyclic voltammetry of the ferrocenium/ferrocene ($\Delta E_p, \text{atm} = 82 \text{ mV}$, $\Delta E_p, 5.2 \text{ MPa} = 159 \text{ mV}$), decamethylferrocenium/decamethylferrocene ($\Delta E_p, \text{atm} = 91 \text{ mV}$, $\Delta E_p, 5.2 \text{ MPa} = 130 \text{ mV}$) and cobaltocenium/cobaltocene ($\Delta E_p, \text{atm} = 76 \text{ mV}$, $\Delta E_p, 5.2 \text{ MPa} = 122 \text{ mV}$) quasi-reversible redox couples under ambient pressure of N₂ in a glovebox (gray) and at 5.2 MPa in the high pressure cell (black). HOPG working electrode (0.09 cm²), 100 mV/s scan rate.

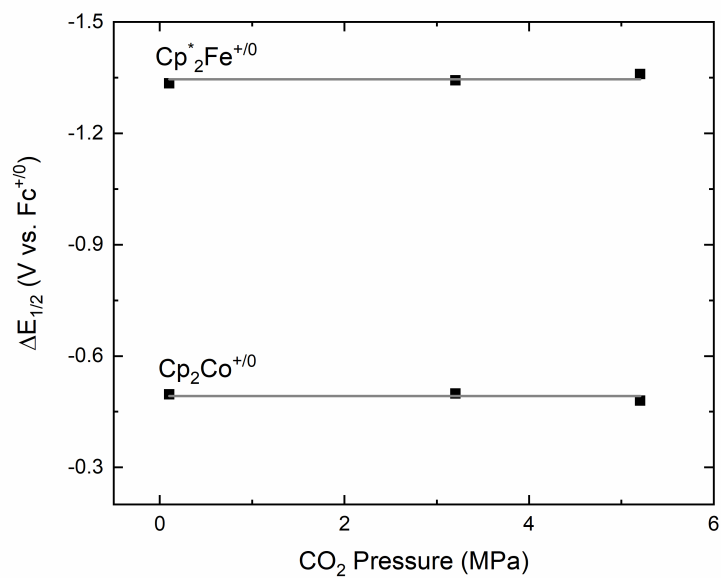


Figure 3.12. Pressure dependence of the relative midpoint potentials of metallocenes. Plot of the deviation in the midpoint potentials of cobaltocene and decamethylferrocene as a function of CO₂ pressure. Note there is no distinguishable difference even at the highest pressures, suggesting the medium's behavior is still dictated primarily by the properties of acetonitrile.

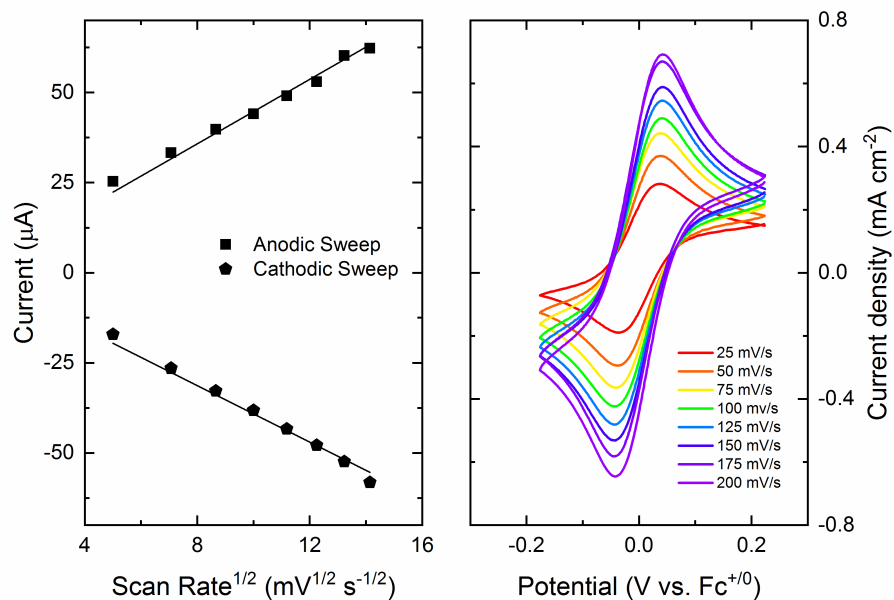


Figure 3.13. Current dependence on scan rate at elevated pressure with Cp₂Fe. Plot demonstrating diffusional behavior of ferrocene in CO₂ expanded electrolyte via application of the Randles-Sevcik equation on variable scan rate data. Linear fits of the observed current versus the square root of scan rate are forced through zero. Reactor was initially charged with 2 mM ferrocene and 0.4 M TBAPF₆ before being pressurized to 3.7 MPa CO₂. HOPG working electrode (0.09 cm²).

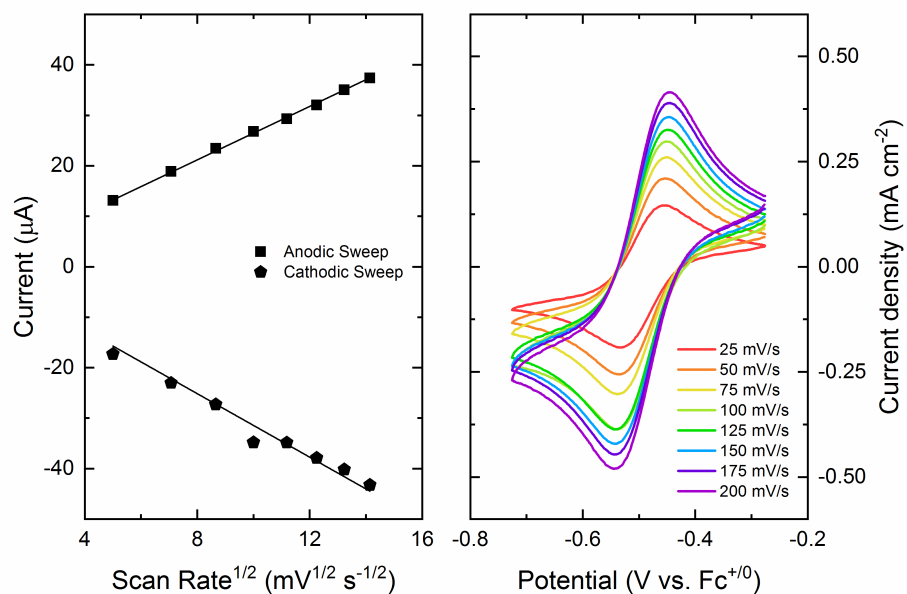


Figure 3.14. Current dependence on scan rate at elevated pressure with Cp*2Fe. Plot demonstrating diffusional behavior of ferrocene in CO₂ expanded electrolyte via application of the Randles-Sevcik equation on variable scan rate data. Linear fits of the observed current versus the square root of scan rate are forced through zero. Reactor was initially charged with 2 mM decaethylferrocene and 0.4 M TBAPF₆ before being pressurized to 3.7 MPa CO₂. HOPG working electrode (0.09 cm²).

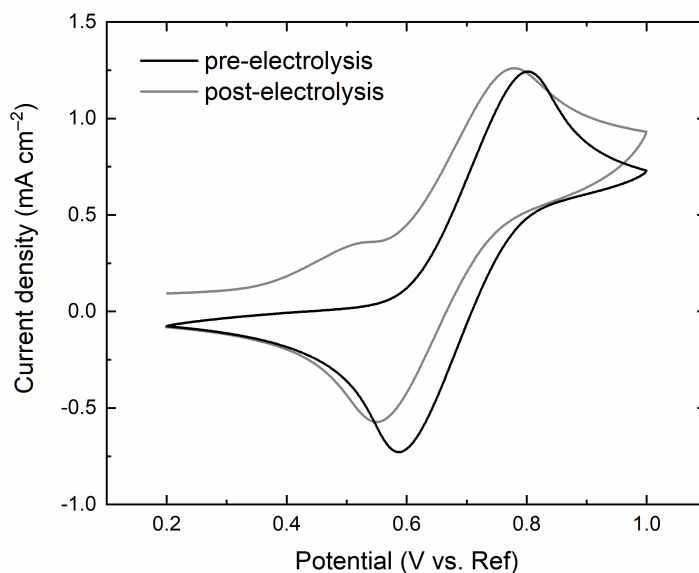


Figure 3.15. Potential of ferrocene internal standard before and after electrolysis. Cyclic voltammetry of the ferrocenium/ferrocene redox couple at 3.2 MPa CO₂, both before (black) and after (gray) 14 h of polarization at -2.5 V vs. Fc^{+ / 0}. The redox couple is originally +694 mV versus reference, and after electrolysis there is a minor 30 mV shift to +664 mV vs. reference.

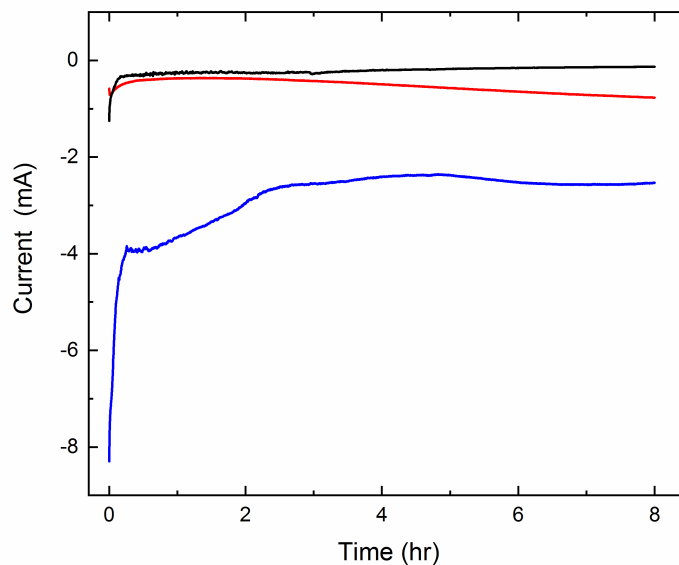


Figure 3.16. Current response as a function of pressure in CXE media. Chronoamperometry performed under variable pressures of CO₂. Black: 0.24 MPa of CO₂. Red: 5.1 MPa CO₂. Blue: 3.2 MPa. 1.16 cm² Au coil electrode, potential held at -2.5 V vs. Fc^{+ / 0}.

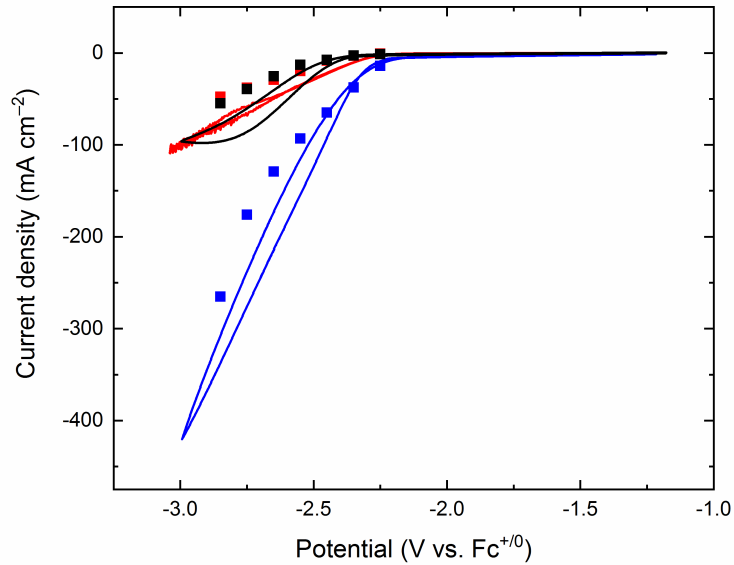


Figure 3.17. Steady-state current response as a function of pressure in CXE media. Cyclic voltammetry conducted under variable pressure of CO₂. Blue: 3.2 MPa of CO₂. Red: 5.2 MPa CO₂. Black: 0.3 MPa CO₂. 200 μm Au disk electrode, scan rate 100 mV/s for CVs. Squares are the steady-state currents for the electrode at a given potential after 100 seconds of polarization.

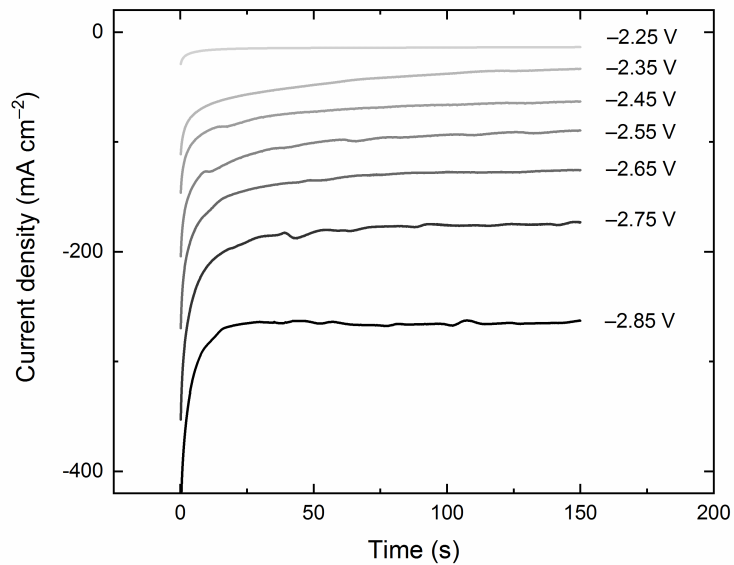


Figure 3.18. Representative current response as a function of potential in CXE media. Chronoamperometry performed at various potentials under 3.2 MPa of CO₂. Potentials reported in V vs. Fc^{+ / 0}. 200 μm Au disk electrode

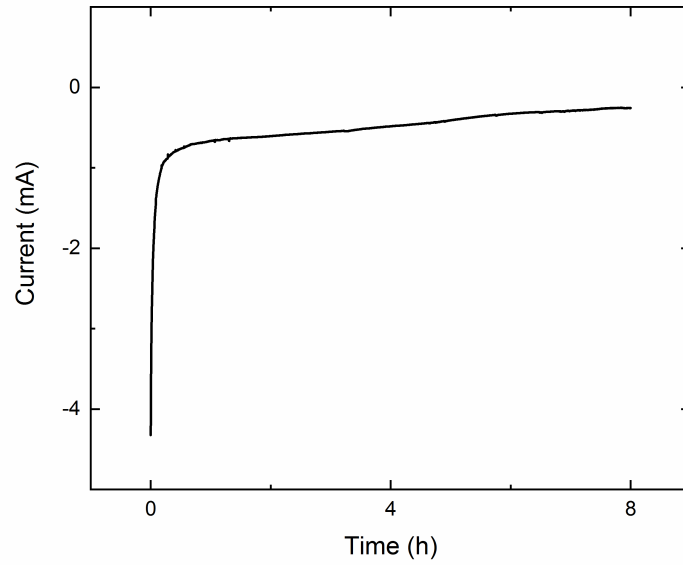


Figure 3.19. Current response with time in nonexpanded media. Chronoamperometry performed for 8 hours under 0.24 MPa of CO_2 . 1.16 cm^2 Au coil electrode, potential held at -2.5 V vs. $\text{Fc}^{+/0}$.

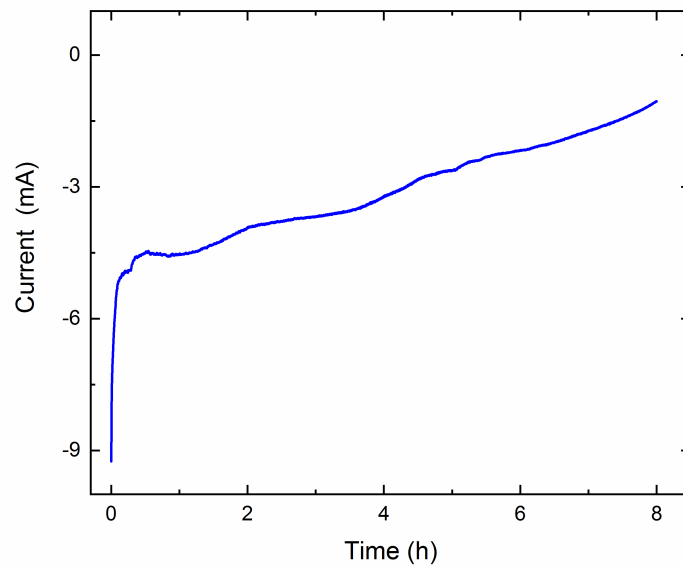


Figure 3.20. Current response with time at elevated pressure. Chronoamperometry performed for 8 hours under 3.2 MPa of CO_2 . 1.16 cm^2 Au coil electrode, potential held at -2.5 V vs. $\text{Fc}^{+/0}$.

3.6.3 Electronic Absorbance Spectroscopy Supporting Experiments

To confirm the expansion data, as well as set up future experiments with homogeneous catalysts, UV-Vis experiments were conducted with $[\text{Re}(\text{CO})_3(\text{bpy})\text{MeCN}][\text{PF}_6]$. In Figure 3.21 the baseline UV-Vis spectrum in unexpanded acetonitrile was taken to establish extinction coefficients for the complex. Figures 3.22 and 3.23 show a series of UV-Vis spectra for the complex at increasing pressures of CO_2 . Using the extinction coefficient calculated from Figure 3.21 the concentration of the Re catalyst was calculated at various pressures. In Figures 3.24 and 3.25 the concentrations are plotted with the expansion data. The excellent correlation confirms that the expansion data was accurate.

Figures 3.26, 3.27, and 3.28 show the same series of UV-Vis experiments but with ferrocene instead of the Re catalyst.

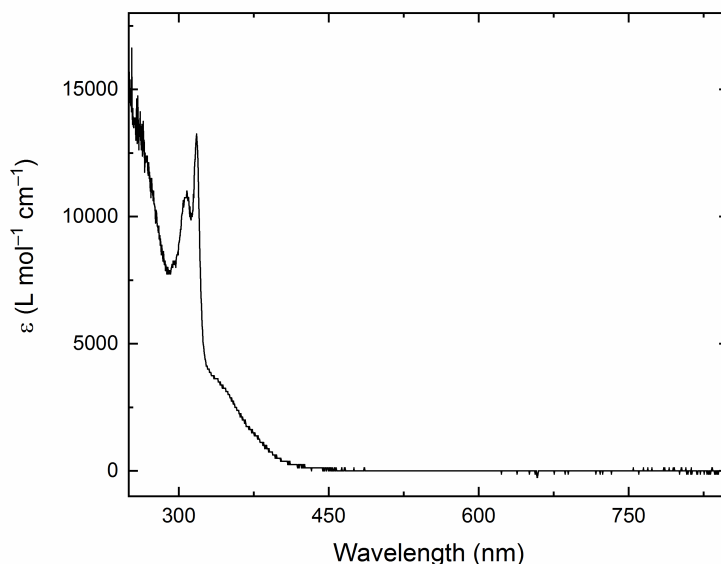


Figure 3.21. Electronic absorbance spectrum of $[\text{Re}(\text{CO})_3(\text{bpy})\text{MeCN}][\text{PF}_6]$. UV-visible spectrum taken in the absence of CO_2 to determine the extinction coefficient of the complex's absorption bands. $80 \mu\text{M}$ $[\text{Re}(\text{CO})_3(\text{bpy})\text{MeCN}][\text{PF}_6]$, 0.4 M TBAPF₆ in MeCN.

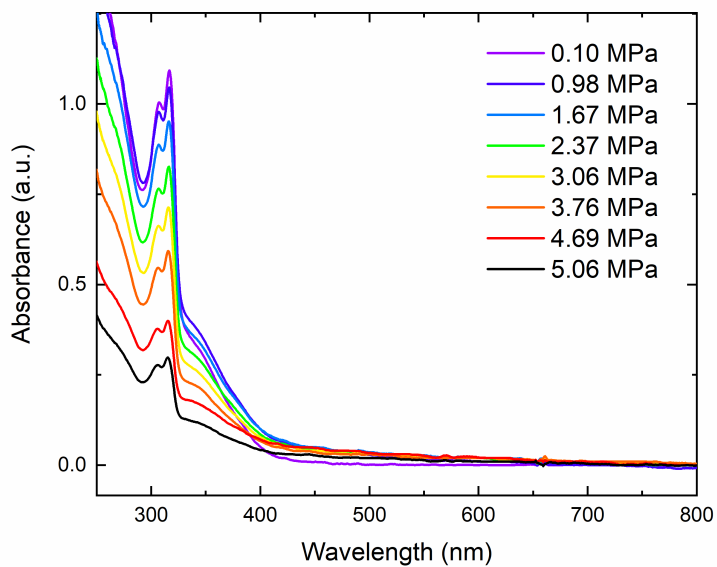


Figure 3.22. Charge transfer band of $[\text{Re}(\text{CO})_3(\text{bpy})\text{MeCN}][\text{PF}_6]$ in MeCN. UV-visible spectroscopy performed initially with $80 \mu\text{M}$ $[\text{Re}(\text{CO})_3(\text{bpy})\text{MeCN}][\text{PF}_6]$ in MeCN at progressively increasing pressures of CO_2 . Reduction in the absorption value corresponds to dilution of the metal complex taking place during volume expansion at higher pressures. Features present include $\pi - \pi^*$ (ca. 320 nm) bands and a broad MLCT band (ca. 350 nm).

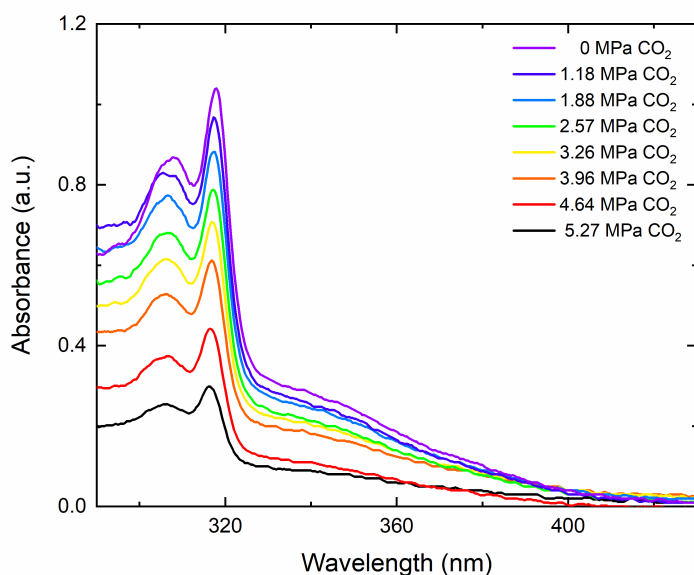


Figure 3.23. Charge transfer band of $[\text{Re}(\text{CO})_3(\text{bpy})\text{MeCN}][\text{PF}_6]$ in electrolyte. UV-visible spectroscopy performed initially with $80 \mu\text{M}$ $[\text{Re}(\text{CO})_3(\text{bpy})\text{MeCN}][\text{PF}_6]$ and 0.4 M TBAPF₆ in MeCN at progressively increasing pressures of CO₂. Reduction in the absorption value corresponds to dilution of the metal complex taking place during volume expansion at higher pressures.

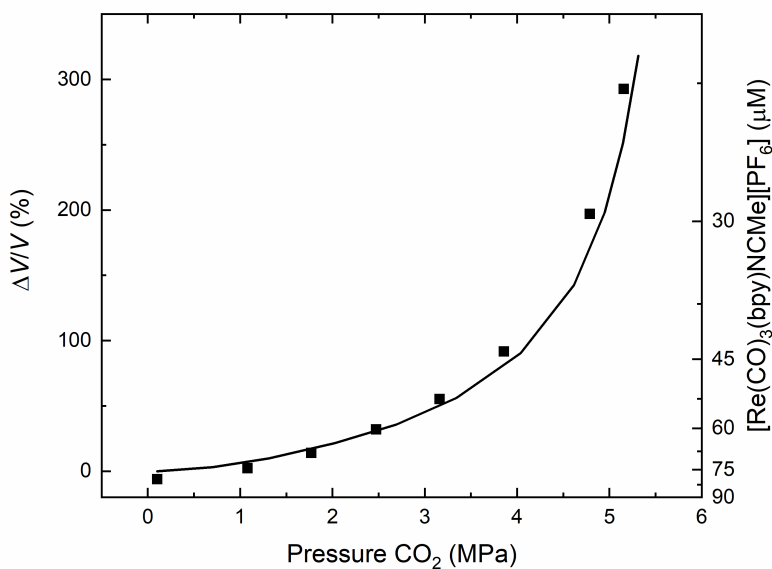


Figure 3.24. $[\text{Re}]$ concentration change with volume expansion. Relationship between volumetric expansion and dissolved complex concentration with increasing pressure of CO₂. Black line: Volumetric expansion curve of MeCN. Black squares: Concentration of rhenium complex was initially $80 \mu\text{M}$ $[\text{Re}(\text{CO})_3(\text{bpy})\text{MeCN}][\text{PF}_6]$, and determined from the absorption of the $[\text{Re}]$ species at 316 nm .

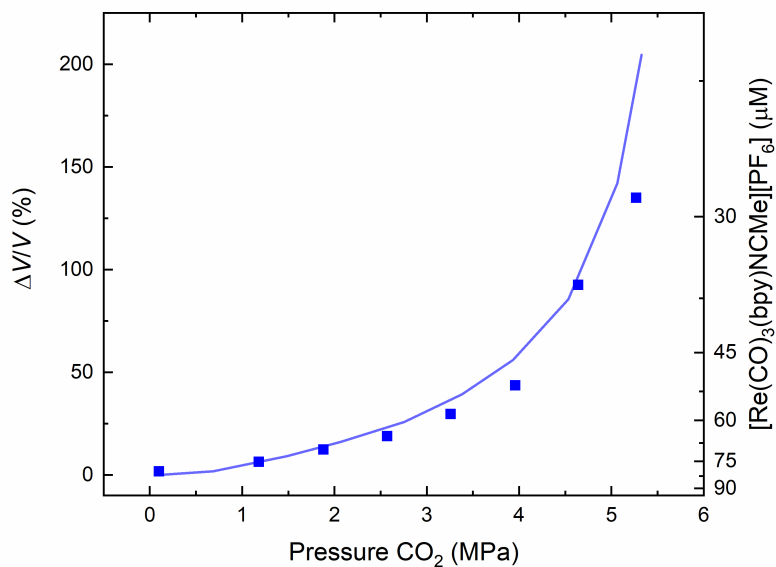


Figure 3.25. [Re] concentration change with volume expansion in electrolyte. Relationship between volumetric expansion and dissolved complex concentration with increasing pressure of CO₂. Blue line: Volumetric expansion curve of MeCN initially supporting 0.4 M TBAPF₆. Blue squares: Concentration of rhenium complex in electrolyte, initially 80 μM [Re(CO)₃(bpy)MeCN][PF₆] and 0.4 M TBAPF₆, and determined from the absorption of the [Re] species at 316 nm.

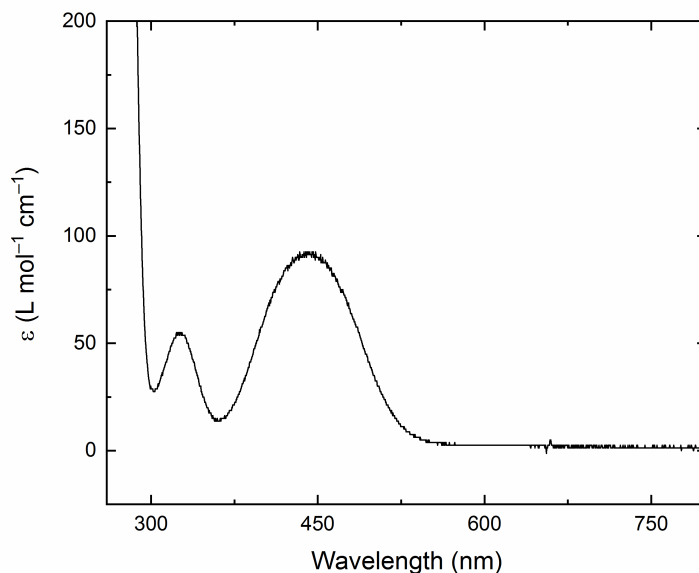


Figure 3.26. Electronic absorption spectrum of ferrocene. UV-visible spectrum taken in the absence of CO₂ to determine the extinction coefficient of the complex's different absorption bands. 8 mM ferrocene, 0.4 M TBAPF₆ in MeCN.

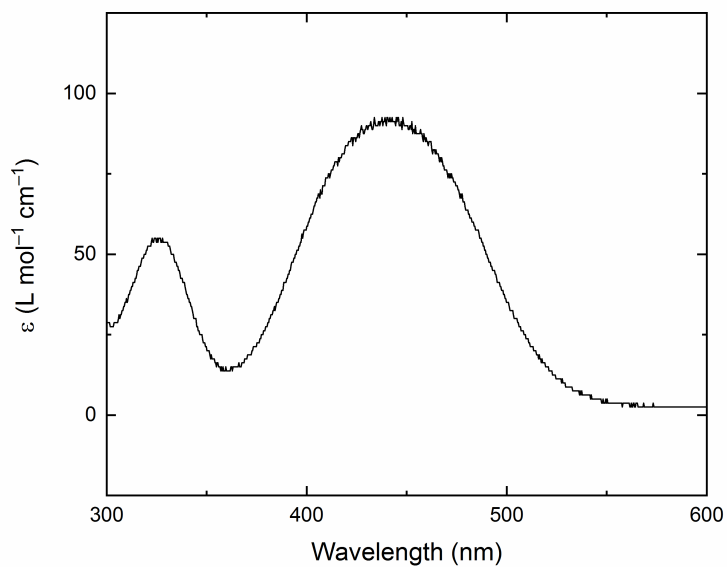


Figure 3.27. d-d band of ferrocene. UV-visible spectrum of ferrocene showing the extinction coefficient of a d-d band of interest. 8 mM ferrocene, 0.4 M TBAPF₆ in MeCN.

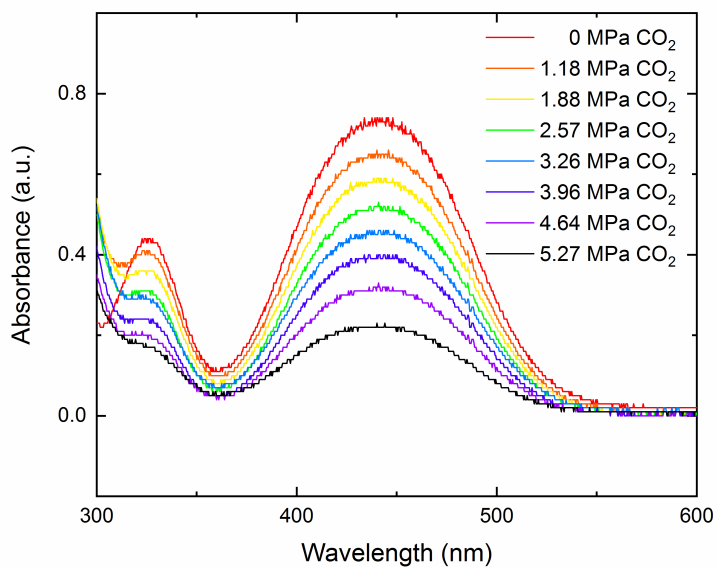


Figure 3.28. Response of d-d band with increasing CO₂ pressure. UV-visible spectroscopy performed initially with 8 mM ferrocene and 0.4 M TBAPF₆ in MeCN at progressively increasing pressures of CO₂. Reduction in the absorption value corresponds to dilution of the metal complex taking place during volume expansion at higher pressures.

3.6.4 Gas Chromatography Supporting Figures

The quantitative analysis with error bars of the products from the electroreduction are shown in Figures 3.29 and 3.30. It is especially important to note that the product amounts formed match the increase in current that the CV data shows. The types of products found are also important. Despite efforts to keep the solution air and water free, it appears that some stray water entered the system which lead to the production of hydrogen at near ambient pressures of CO_2 . This parasitic production of hydrogen is not present at high pressures of CO_2 .

The GC readouts from the headspace gasses at representative pressures are shown in Figures 3.31 through 3.36. Figures 3.37 and 3.38 show readouts from the electrolyte. No product peaks are present which confirms that gold does not change its products at high pressures of CO_2 . The final two GC readouts show the high purity CO_2 used in all experiments.

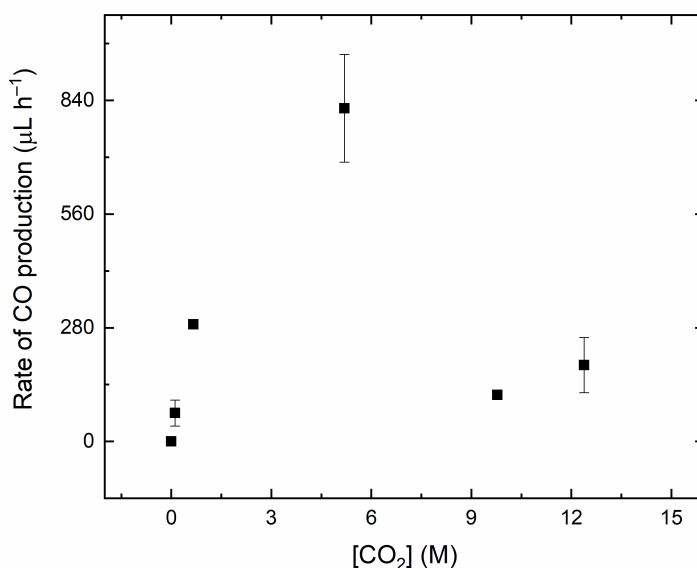


Figure 3.29. Production of CO as a function of CO_2 pressure. Mirroring the figure in the main text, this is a plot of the observed rates of CO production, determined from gas chromatography, as a function of CO_2 pressure. Error bars are calculated from the standard deviation of replicate measurements.

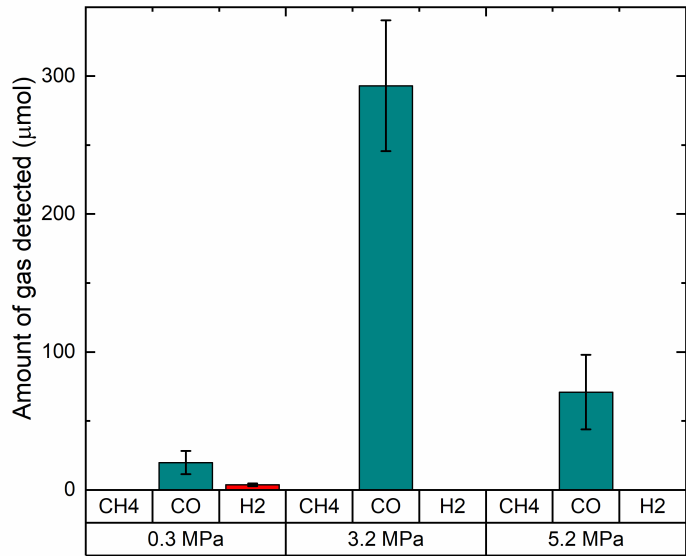


Figure 3.30. Quantification of detected carbon monoxide at various pressures. Bar plot depicting the average quantity of gas products generated at different pressures following 8 h bulk electrolysis at -2.5 V vs. $\text{Fc}^{+/0}$. 1.16 cm^2 Au coil electrode used. Trace amounts of methane (nmol quantities) were detected in all experiments from an impurity in the CO_2 gas supply.

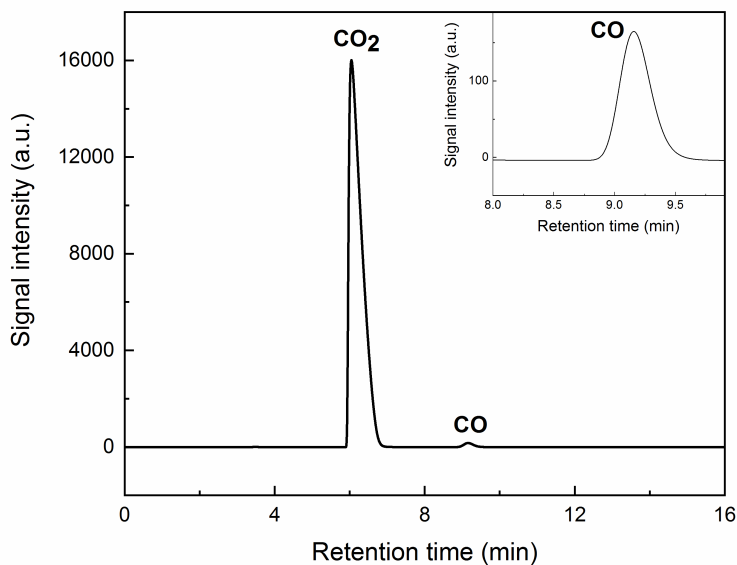


Figure 3.31. FID gas chromatogram of near-ambient pressure electrolysis headspace. Gas chromatogram of headspace gas from an 8 h electrolysis at -2.5 V vs. $\text{Fc}^{+/0}$ on Au wire, 0.4 MPa CO_2 , FID with methanizer. Inset shows a detailed view of CO signal. No other products were detected by the methanizer-equipped FID. Peak intensities are large enough that valve changes are not visible.

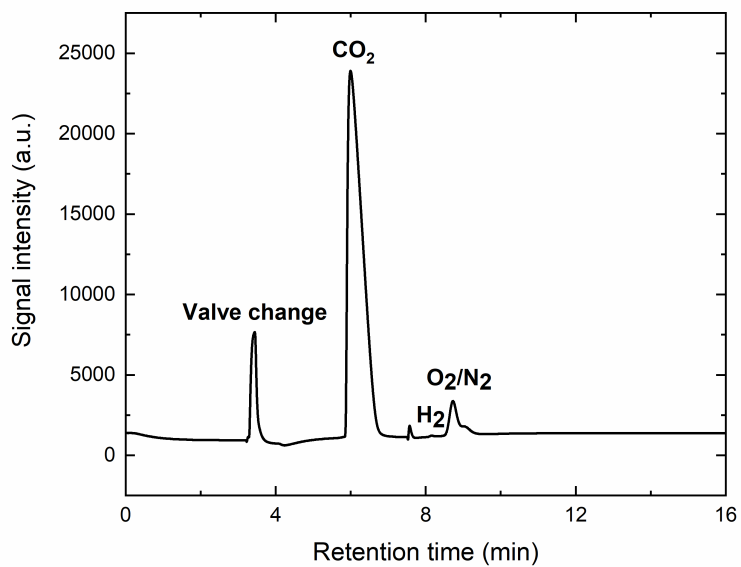


Figure 3.32. TCD gas chromatogram of near-ambient pressure electrolysis headspace. Gas chromatogram of headspace gas from an 8 h electrolysis at -2.5 V vs. $\text{Fc}^{+/0}$ on Au wire at 0.4 MPa CO_2 , TCD. No other products were detected by the TCD.

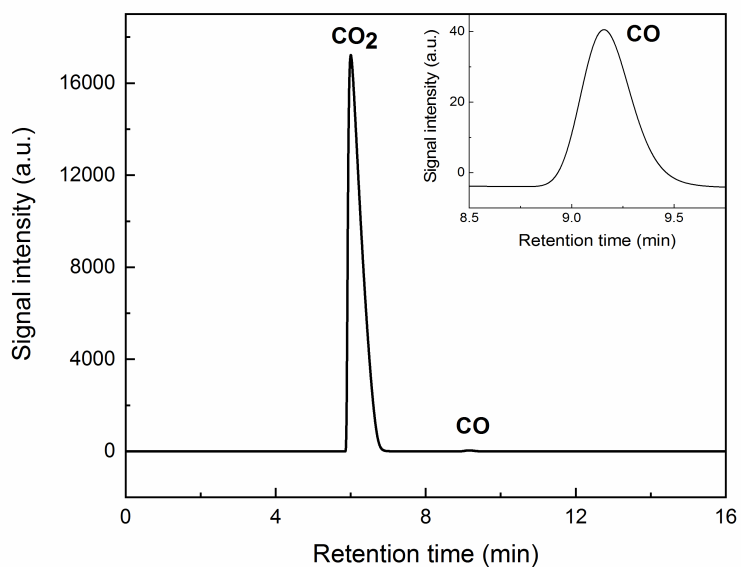


Figure 3.33. FID gas chromatogram of mid pressure electrolysis headspace. Gas chromatogram of headspace gas from an 8 h electrolysis at -2.5 V vs. $\text{Fc}^{+/0}$ on Au wire at 3.2 MPa CO_2 , FID with methanizer. Inset shows a detailed view of CO signal. Peak intensities are large enough that valve changes are not visible.

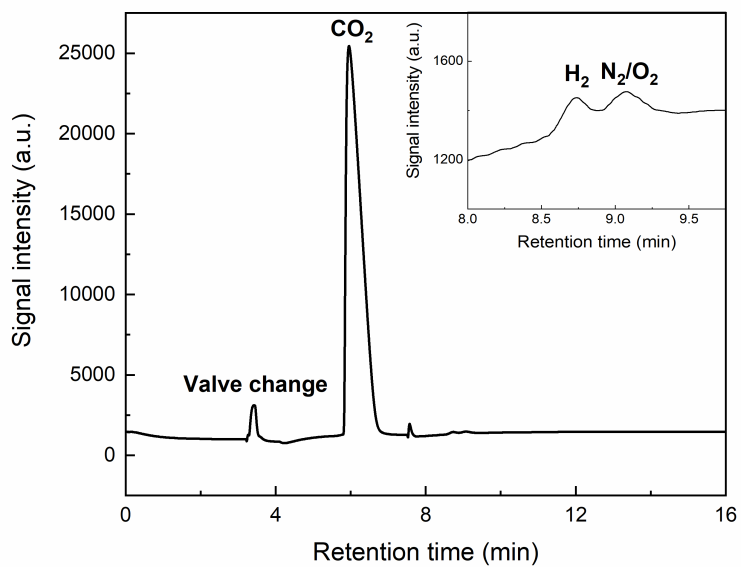


Figure 3.34. TCD gas chromatogram of mid pressure electrolysis headspace. Gas chromatogram of headspace gas from an 8 h electrolysis at -2.5 V vs. $\text{Fc}^{+/0}$ on Au wire at 3.2 MPa CO_2 , TCD. Inset shows a detailed view of H_2 and N_2/O_2 signals. No other products were detected by the TCD.

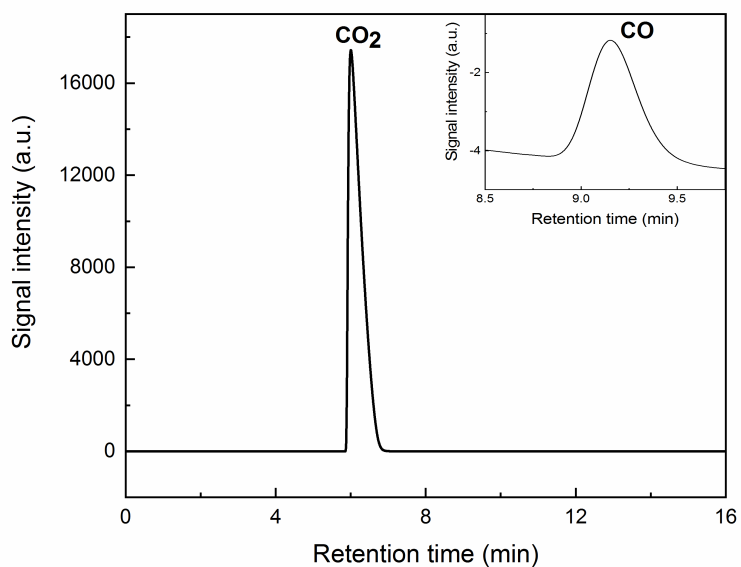


Figure 3.35. FID gas chromatogram of high pressure electrolysis headspace. Gas chromatogram of headspace gas from an 8 h electrolysis at -2.5 V vs. $\text{Fc}^{+/0}$ on Au wire at 5.2 MPa CO_2 , FID with methanizer. Inset shows a detailed view of CO signal. Peak intensities are large enough that valve changes are not visible.

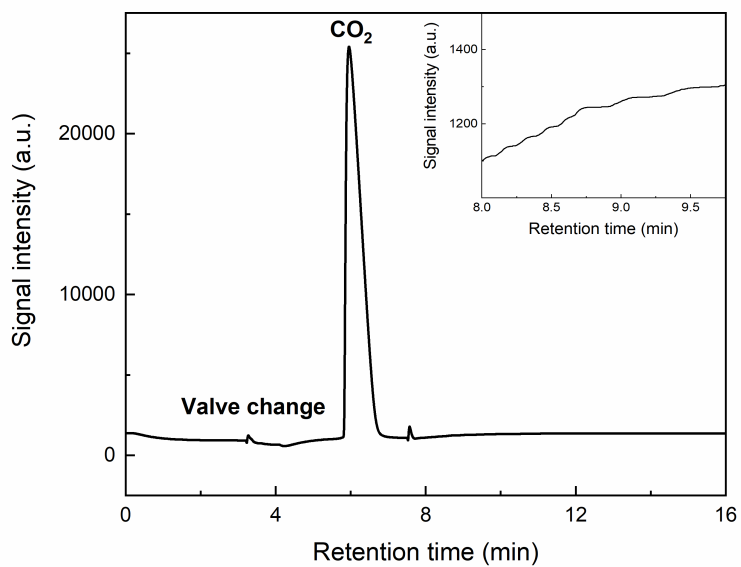


Figure 3.36. TCD gas chromatogram of high pressure electrolysis headspace. Gas chromatogram of headspace gas from an 8 h electrolysis at -2.5 V vs. $\text{Fc}^{+/0}$ on Au wire at 5.2 MPa CO_2 , TCD. Inset shows absence of an H_2 signal. No other products were detected by the TCD.

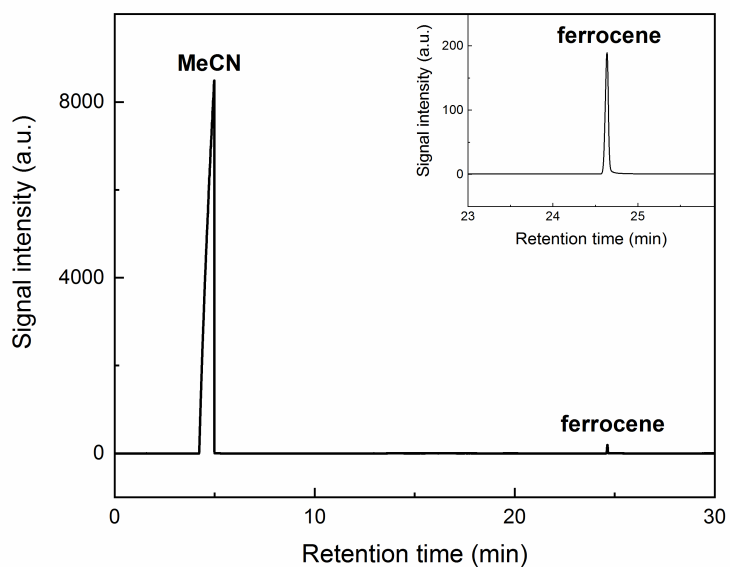


Figure 3.37. FID gas chromatogram of electrolyte liquid. Gas chromatogram of liquid sampled from electrolyte solution, FID. Inset shows a detailed view of the only signal observed, associated with the electrolyte itself. Peak intensities are large enough that valve changes are not visible.

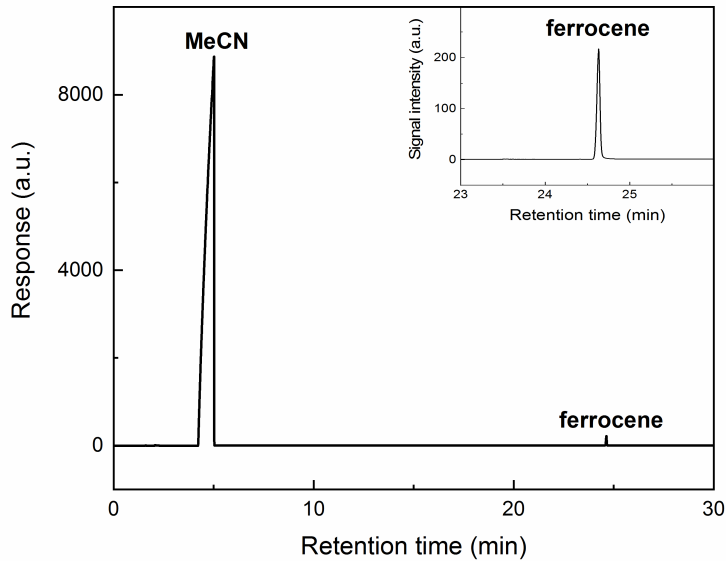


Figure 3.38. FID gas chromatogram of liquid from mid pressure electrolysis. Gas chromatogram of liquid sampled from an 8 h electrolysis on Au wire at -2.5 V vs. $\text{Fc}^{+/0}$, 3.2 MPa CO_2 , FID. Inset shows a detailed view of the only signal observed, associated with the electrolyte itself. Peak intensities are large enough that valve changes are not visible.

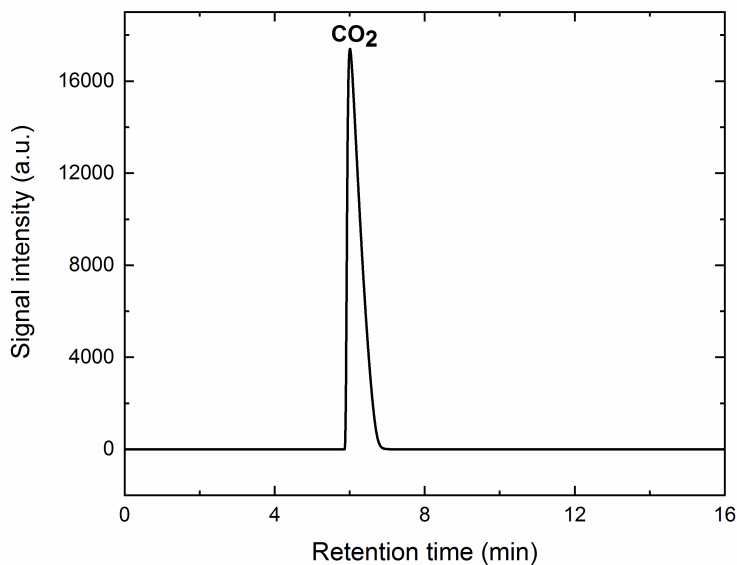


Figure 3.39. FID gas chromatogram of CO_2 gas. Control gas chromatogram of high purity CO_2 gas used in all other experiments, FID with methanizer. Besides trace amounts of methane impurity, no other gases were detected. Peak intensities are large enough that valve changes are not visible.

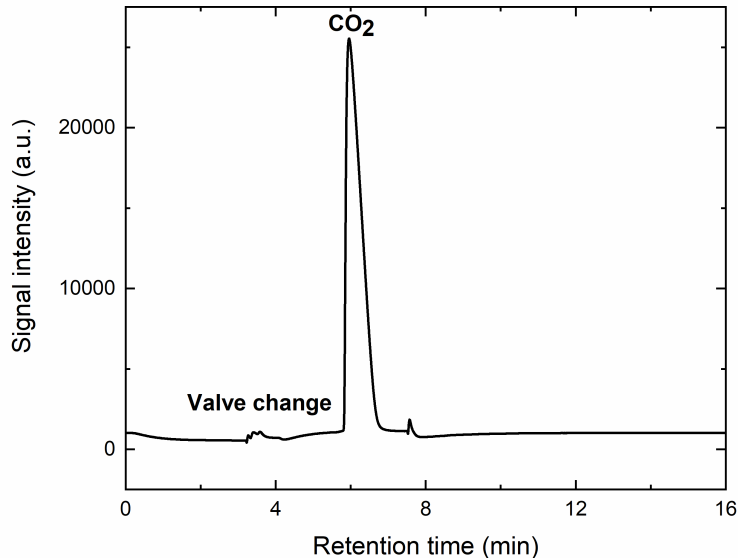


Figure 3.40. TCD gas chromatogram of CO₂ gas. Control gas chromatogram of high purity CO₂ gas used in all other experiments, TCD. Aside from the response at ca. 5 min retention time, no other signals were observed.

3.6.5 COMSOL Modeling

COMSOL (COMSOL Multiphysics v. 5.3) simulations were performed to compute the diffusion coefficient of ferrocene as a function of CO₂ pressure. The COMSOL geometry utilizes a 2D axial-symmetric domain scaled to the electrode size (100 μm radius) and reactor dimensions (3 cm radius, 4 cm height). To create the simulation mesh, a free triangular grid with COMSOL’s built-in “normal” element size was used for the bulk of the reactor, with a “finer” mesh used for a total area of 1 cm² around the electroactive surface. To create a fine mesh around the electrode surface, an edge grid was incorporated into the overall pattern with a minimum element of size of 2×10^{-5} cm² and a maximum element size of 2×10^{-4} cm². The current at the electrode surface was simulated via the COMSOL Electroanalysis module. This module computes the concentration of the oxidized and reduced species in solution and the current on the electroactive boundary as a function of applied potential by coupling the Butler-Volmer equation with Fick’s Second Law of Diffusion. Simulations assumed an electron-transfer rate constant of 1 cm s⁻¹ and a transfer coefficient, α , of 0.5 for the ferrocenium/ferrocene redox reactions. The bulk concentration of

ferrocene was determined using the volumetric expansion data obtained for the electrolyte media at the relevant pressures. The diffusion coefficients were then determined by minimizing the total error between the experimental voltammograms and the simulated data.

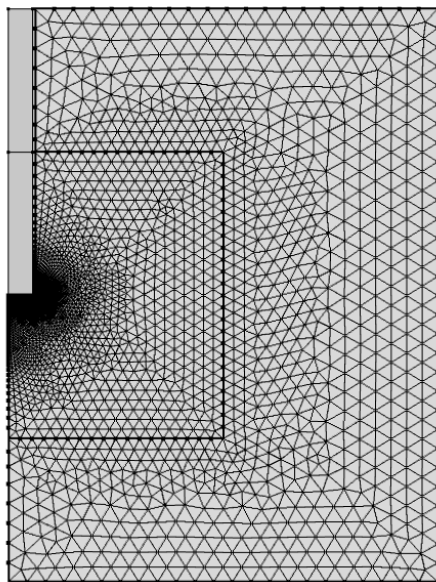


Figure 3.41. Reactor mesh for COMSOL Cp_2Fe diffusion simulations.

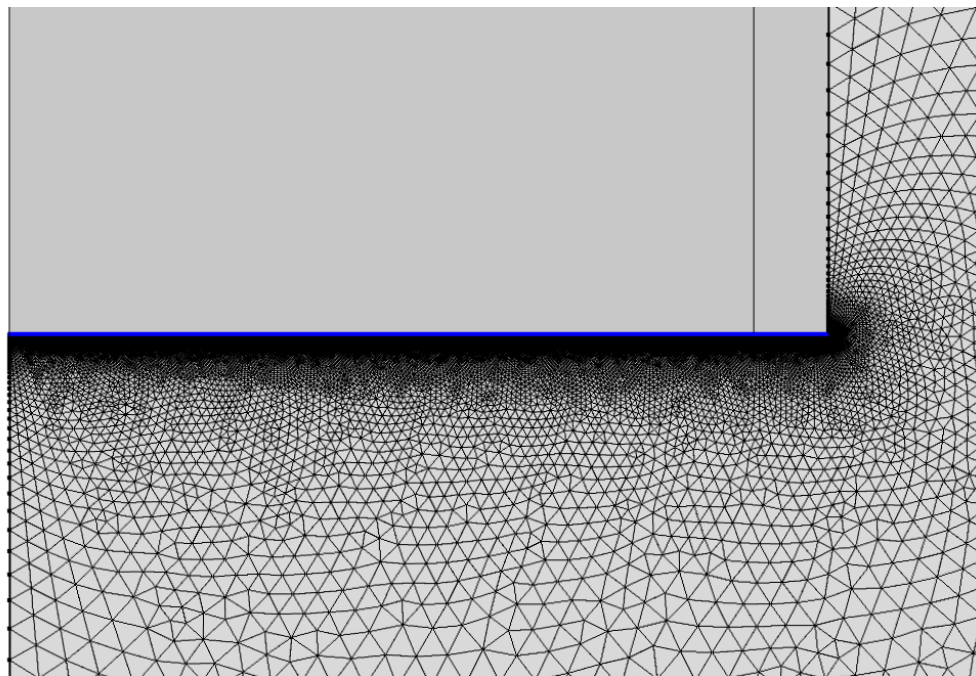


Figure 3.42. Reactor mesh near surface for COMSOL Cp_2Fe diffusion simulations. Outer rectangle of electrode is modeled as an insulating sheath to capture the electrode shape.

References

- [1] others,, et al. (2013) Assessing “dangerous climate change”: required reduction of carbon emissions to protect young people, future generations and nature. *PloS one* 8, e81648.
- [2] Sanz-Perez, E. S., Murdock, C. R., Didas, S. A., and Jones, C. W. (2016) Direct capture of CO₂ from ambient air. *Chemical reviews* 116, 11840–11876.
- [3] Lackner, K. S. (2003) A guide to CO₂ sequestration. *Science* 300, 1677–1678.
- [4] Aresta, M., Dibenedetto, A., and Angelini, A. (2013) The changing paradigm in CO₂ utilization. *Journal of CO₂ Utilization* 3, 65–73.
- [5] Artz, J., Muller, T. E., Thenert, K., Kleinekorte, J., Meys, R., Sternberg, A., Bardow, A., and Leitner, W. (2017) Sustainable conversion of carbon dioxide: an integrated review of catalysis and life cycle assessment. *Chemical reviews* 118, 434–504.
- [6] Yuan, Z., Eden, M. R., and Gani, R. (2015) Toward the development and deployment of large-scale carbon dioxide capture and conversion processes. *Industrial & Engineering Chemistry Research* 55, 3383–3419.
- [7] Song, C. (2006) Global challenges and strategies for control, conversion and utilization of CO₂ for sustainable development involving energy, catalysis, adsorption and chemical processing. *Catalysis today* 115, 2–32.
- [8] Centi, G., Quadrelli, E. A., and Perathoner, S. (2013) Catalysis for CO₂ conversion: a key technology for rapid introduction of renewable energy in the value chain of chemical industries. *Energy & Environmental Science* 6, 1711–1731.

- [9] others., et al. (2013) Frontiers, opportunities, and challenges in biochemical and chemical catalysis of CO₂ fixation. *Chemical reviews* 113, 6621–6658.
- [10] Benson, E. E., Kubiak, C. P., Sathrum, A. J., and Smieja, J. M. (2009) Electrocatalytic and homogeneous approaches to conversion of CO₂ to liquid fuels. *Chemical Society Reviews* 38, 89–99.
- [11] Li, K., Peng, B., and Peng, T. (2016) Recent advances in heterogeneous photocatalytic CO₂ conversion to solar fuels. *ACS Catalysis* 6, 7485–7527.
- [12] Kumar, B., Brian, J. P., Atla, V., Kumari, S., Bertram, K. A., White, R. T., and Spurgeon, J. M. (2016) New trends in the development of heterogeneous catalysts for electrochemical CO₂ reduction. *Catalysis Today* 270, 19–30.
- [13] Hawecker, J., Lehn, J.-M., and Ziessel, R. (1983) Efficient photochemical reduction of CO₂ to CO by visible light irradiation of systems containing Re (bipy)(CO)₃X or Ru (bipy)₃2+–Co²⁺ combinations as homogeneous catalysts. *Journal of the Chemical Society, Chemical Communications* 536–538.
- [14] Grills, D. C., Matsubara, Y., Kuwahara, Y., Golisz, S. R., Kurtz, D. A., and Mello, B. A. (2014) Electrocatalytic CO₂ reduction with a homogeneous catalyst in ionic liquid: high catalytic activity at low overpotential. *The journal of physical chemistry letters* 5, 2033–2038.
- [15] others., et al. (2013) Electrochemical conversion of CO₂ to useful chemicals: current status, remaining challenges, and future opportunities. *Current Opinion in Chemical Engineering* 2, 191–199.
- [16] Chen, Y., Lewis, N. S., and Xiang, C. (2015) Operational constraints and strategies for systems to effect the sustainable, solar-driven reduction of atmospheric CO₂. *Energy & Environmental Science* 8, 3663–3674.
- [17] Mariano, R. G., McKelvey, K., White, H. S., and Kanan, M. W. (2017) Selective increase in CO₂ electroreduction activity at grain-boundary surface terminations. *Science* 358, 1187–1192.

- [18] Kuhl, K. P., Cave, E. R., Abram, D. N., and Jaramillo, T. F. (2012) New insights into the electrochemical reduction of carbon dioxide on metallic copper surfaces. *Energy & Environmental Science* 5, 7050–7059.
- [19] Paris, A. R., and Bocarsly, A. B. (2017) Ni–Al Films on Glassy Carbon Electrodes Generate an Array of Oxygenated Organics from CO₂. *ACS Catalysis* 7, 6815–6820.
- [20] Tatin, A., Comminges, C., Kokoh, B., Costentin, C., Robert, M., and Savéant, J.-M. (2016) Efficient electrolyzer for CO₂ splitting in neutral water using earth-abundant materials. *Proceedings of the National Academy of Sciences* 113, 5526–5529.
- [21] Hori, Y. i. *Modern aspects of electrochemistry*; Springer, 2008; pp 89–189.
- [22] Reda, T., Plugge, C. M., Abram, N. J., and Hirst, J. (2008) Reversible interconversion of carbon dioxide and formate by an electroactive enzyme. *Proceedings of the National Academy of Sciences* 105, 10654–10658.
- [23] Whipple, D. T., Finke, E. C., and Kenis, P. J. (2010) Microfluidic reactor for the electrochemical reduction of carbon dioxide: the effect of pH. *Electrochemical and Solid-State Letters* 13, B109–B111.
- [24] Verma, S., Hamasaki, Y., Kim, C., Huang, W., Lu, S., Jhong, H.-R. M., Gewirth, A. A., Fujigaya, T., Nakashima, N., and Kenis, P. J. (2017) Insights into the Low Overpotential Electroreduction of CO₂ to CO on a Supported Gold Catalyst in an Alkaline Flow Electrolyzer. *ACS Energy Letters* 3, 193–198.
- [25] Merino-Garcia, I., Alvarez-Guerra, E., Albo, J., and Irabien, A. (2016) Electrochemical membrane reactors for the utilisation of carbon dioxide. *Chemical Engineering Journal* 305, 104–120.
- [26] Endrődi, B., Bencsik, G., Darvas, F., Jones, R., Rajeshwar, K., and Janáky, C. (2017) Continuous-flow electroreduction of carbon dioxide. *Progress in Energy and Combustion Science* 62, 133–154.

- [27] Rosen, B. A., Salehi-Khojin, A., Thorson, M. R., Zhu, W., Whipple, D. T., Kenis, P. J., and Masel, R. I. (2011) Ionic liquid-mediated selective conversion of CO₂ to CO at low overpotentials. *Science* 1209786.
- [28] others., et al. (2016) Enhanced electrocatalytic CO₂ reduction via field-induced reagent concentration. *Nature* 537, 382.
- [29] Silvestri, G., Gambino, S., Filardo, G., Cuccia, C., and Guarino, E. (1981) Electrochemical processes in supercritical phases. *Angewandte Chemie International Edition in English* 20, 101–102.
- [30] Grills, D. C., and Fujita, E. (2010) New directions for the photocatalytic reduction of CO₂: Supramolecular, scCO₂ or biphasic ionic liquid- scCO₂ systems. *The Journal of Physical Chemistry Letters* 1, 2709–2718.
- [31] Abbott, A. P., and Eardley, C. A. (2000) Electrochemical reduction of CO₂ in a mixed supercritical fluid. *The Journal of Physical Chemistry B* 104, 775–779.
- [32] Melchaeva, O., Voyame, P., Bassetto, V. C., Prokein, M., Renner, M., Weidner, E., Petermann, M., and Battistel, A. (2017) Electrochemical Reduction of Protic Supercritical CO₂ on Copper Electrodes. *ChemSusChem* 10, 3660–3670.
- [33] Zhao, G., Jiang, T., Han, B., Li, Z., Zhang, J., Liu, Z., He, J., and Wu, W. (2004) Electrochemical reduction of supercritical carbon dioxide in ionic liquid 1-n-butyl-3-methylimidazolium hexafluorophosphate. *The Journal of supercritical fluids* 32, 287–291.
- [34] Toghiani, K. E., Mendez, M. A., and Voyame, P. (2014) Electrochemistry in supercritical fluids: a mini review. *Electrochemistry Communications* 44, 27–30.
- [35] others., et al. (2001) Fundamentals and applications. *Electrochemical Methods* 2, 482.
- [36] Fujita, E., Szalda, D. J., Creutz, C., and Sutin, N. (1988) Carbon dioxide activation: thermodynamics of carbon dioxide binding and the involvement of two cobalt centers in the reduction of carbon dioxide by a cobalt (I) macrocycle. *Journal of the American Chemical Society* 110, 4870–4871.

- [37] Jessop, P. G., and Subramaniam, B. (2007) Gas-expanded liquids. *Chemical reviews* 107, 2666–2694.
- [38] Kordikowski, A., Schenk, A., Van Nielen, R., and Peters, C. (1995) Volume expansions and vapor-liquid equilibria of binary mixtures of a variety of polar solvents and certain near-critical solvents. *The Journal of Supercritical Fluids* 8, 205–216.
- [39] Ren, W., and Scurto, A. M. (2007) High-pressure phase equilibria with compressed gases. *Review of scientific instruments* 78, 125104.
- [40] Todd, D. B., and Elgin, J. C. (1955) Phase equilibria in systems with ethylene above its critical temperature. *AIChE Journal* 1, 20–27.
- [41] Scurto, A., Hutchenson, K., and Subramaniam, B. Gas-expanded liquids: fundamentals and applications. Symposium A Quarterly Journal In Modern Foreign Literatures. 2009; pp 3–37.
- [42] Houndonougbo, Y., Jin, H., Rajagopalan, B., Wong, K., Kuczera, K., Subramaniam, B., and Laird, B. (2006) Phase equilibria in carbon dioxide expanded solvents: Experiments and molecular simulations. *The Journal of Physical Chemistry B* 110, 13195–13202.
- [43] Subramaniam, B. (2015) Perspectives on exploiting near-critical fluids for energy-efficient catalytic conversion of emerging feedstocks. *The Journal of Supercritical Fluids* 96, 96–102.
- [44] Hori, H., Koike, K., Suzuki, Y., Ishizuka, M., Tanaka, J., Takeuchi, K., and Sasaki, Y. (2002) High-pressure photocatalytic reduction of carbon dioxide using [fac-Re (bpy)(CO) 3P (OiPr) 3]+(bpy= 2, 2'-bipyridine). *Journal of Molecular Catalysis A: Chemical* 179, 1–9.
- [45] Duan, Z., and Sun, R. (2003) An improved model calculating CO₂ solubility in pure water and aqueous NaCl solutions from 273 to 533 K and from 0 to 2000 bar. *Chemical geology* 193, 257–271.
- [46] Gagne, R. R., Koval, C. A., and Lisensky, G. C. (1980) Ferrocene as an internal standard for electrochemical measurements. *Inorganic Chemistry* 19, 2854–2855.
- [47] Appel, A. M., and Helm, M. L. Determining the overpotential for a molecular electrocatalyst. 2014.

- [48] Connelly, N. G., and Geiger, W. E. (1996) Chemical redox agents for organometallic chemistry. *Chemical Reviews* 96, 877–910.
- [49] Randles, J. E. (1948) A cathode ray polarograph. Part II.—The current-voltage curves. *Transactions of the Faraday Society* 44, 327–338.
- [50] Ševčík, A. (1948) Oscillographic polarography with periodical triangular voltage. *Collection of Czechoslovak Chemical Communications* 13, 349–377.
- [51] Kadish, K., Ding, J., and Malinski, T. (1984) Resistance of nonaqueous solvent systems containing tetraalkylammonium salts. Evaluation of heterogeneous electron transfer rate constants for the ferrocene/ferrocenium couple. *Analytical chemistry* 56, 1741–1744.
- [52] Martin, R. D., and Unwin, P. R. (1997) Scanning electrochemical microscopy: theory and experiment for the positive feedback mode with unequal diffusion coefficients of the redox mediator couple. *Journal of Electroanalytical Chemistry* 439, 123–136.
- [53] Laitinen, H., and Kolthoff, I. (1939) A study of diffusion processes by electrolysis with microelectrodes. *Journal of the American Chemical Society* 61, 3344–3349.
- [54] Stejskal, E. O., and Tanner, J. E. (1965) Spin diffusion measurements: spin echoes in the presence of a time-dependent field gradient. *The journal of chemical physics* 42, 288–292.
- [55] Cohen, Y., Avram, L., and Frish, L. (2005) Diffusion NMR spectroscopy in supramolecular and combinatorial chemistry: an old parameter—new insights. *Angewandte Chemie International Edition* 44, 520–554.
- [56] Ikeda, S., Takagi, T., and Ito, K. (1987) Selective formation of formic acid, oxalic acid, and carbon monoxide by electrochemical reduction of carbon dioxide. *Bulletin of the Chemical Society of Japan* 60, 2517–2522.
- [57] Popczun, E. J., McKone, J. R., Read, C. G., Biacchi, A. J., Wiltrout, A. M., Lewis, N. S., and Schaak, R. E. (2013) Nanostructured nickel phosphide as an electrocatalyst for the hydrogen evolution reaction. *Journal of the American Chemical Society* 135, 9267–9270.

- [58] Savéant, J.-M. *Elements of molecular and biomolecular electrochemistry: an electrochemical approach to electron transfer chemistry*; John Wiley & Sons, 2006; Vol. 13.
- [59] Bourrez, M., Molton, F., Chardon-Noblat, S., and Deronzier, A. (2011) [Mn (bipyridyl)(CO)₃Br]: An abundant metal carbonyl complex as efficient electrocatalyst for CO₂ reduction. *Angewandte Chemie International Edition* 50, 9903–9906.
- [60] Hayashi, Y., Kita, S., Brunshwig, B. S., and Fujita, E. (2003) Involvement of a Binuclear Species with the Re- C (O) O- Re Moiety in CO₂ Reduction Catalyzed by Tricarbonyl Rhenium (I) Complexes with Diimine Ligands: Strikingly Slow Formation of the Re- Re and Re- C (O) O- Re Species from Re (dmb)(CO)₃S (dmb= 4, 4 '-Dimethyl-2, 2 '-bipyridine, S= Solvent). *Journal of the American Chemical Society* 125, 11976–11987.
- [61] Bolinger, C. M., Sullivan, B. P., Conrad, D., Gilbert, J. A., Story, N., and Meyer, T. J. (1985) Electrocatalytic reduction of CO₂ based on polypyridyl complexes of rhodium and ruthenium. *Journal of the Chemical Society, Chemical Communications* 796–797.

Chapter 4

Insights Into the Pressure Dependent Reaction Rates for the Electrochemical Reduction of CO₂ in CO₂ Expanded Electrolytes

Abstract

Electrochemical CO₂ reduction has been limited by the solubility of CO₂ in conventional aqueous solvents. CO₂ Expanded Electrolytes (CXEs) have the ability to tunably solvate multi-molar amounts of CO₂. By utilizing this tunability to generate cyclic voltammograms at widely separated concentrations of CO₂ it was found that on multiple catalysts the catalytic rate has an optimal concentrations of CO₂ (3.1 MPa), beyond which the rate decreases. Using COMSOL modeling of CO₂ electrochemical reduction on gold we show that the maximum value for catalysis is a result of a decrease in the rate of an elementary reaction step at high concentrations of CO₂. This insight into the relationship between CO₂ concentration and catalytic rate will guide the future development of electrochemical CO₂ reduction systems.

4.1 Introduction

The development of new methods to capture and convert CO₂ into value-added fuels and chemicals is a grand challenge in sustainability science due to the need to mitigate anthropogenic climate change and utilize new carbon feedstocks.¹⁻⁴ Of the many ways to convert CO₂, the electrochemical reduction of CO₂ is a promising method because it operates at low temperatures and can be powered by carbon free renewable energy such as solar or wind.⁵⁻⁷ Even though several large-scale electrolysis technologies have been commercialized (e.g, the production of chlorine via the chloral alkali process and the extraction of metals via electrowinning), the large scale industrial adoption of electrochemical reduction of CO₂ has some major obstacles which thus far have stymied any adoption.⁸ A major roadblock for electrocatalytic CO₂ conversion is the poor solubility of CO₂ in conventional aqueous solvents.⁹ At ambient pressure, the solubility CO₂ in aqueous electrolytes is only 0.034 M, which causes low CO₂ conversion rates. Per Henry’s Law, it is possible to linearly increase CO₂ concentration in such media by simply increasing the head-space pressure.¹⁰ However, even at elevated pressures, the CO₂ concentration is still too low in aqueous solvents to achieve industrial relevant reactions rates.¹¹

Major inroads have been made in CO₂ conversion rates by improving mass transfer through the utilization of gas diffusion electrodes.¹²⁻¹⁶ Gas-diffusion electrodes allow for CO₂ reduction to be operated at current densities ca. ten times higher than those achieved using planar metal electrodes.¹⁵ Another approach to increase the rate of reaction is to engineer the catalyst surface to increasing surface area and number of catalytically active sites. Many techniques have been used to accomplish this. For example, *in-situ* reduced Au oxide derived catalysts have also shown great promise.¹⁷ The reduced surfaces show higher porosity, which leads to greater surface area and more exposed active sites. Other nanostructuring techniques have also been utilized to increase catalytic rates of CO₂ reduction by increasing surface area, exposing specific crystal facets,¹⁸ increasing edge sites,¹⁹⁻²¹ and grain boundary engineering.²²

However, with all of these systems, the low concentration of CO₂ still limits the reaction rates. To circumvent this problem, our groups recently have shown that in organic electrolytes, liquid-phase CO₂ concentration is non-linear with CO₂ head-space pressure.²³ In this system, we have observed multi-molar liquid-phase CO₂ concentrations approaching the concentration of pure liquid-

CO₂. During pressurization of these organic electrolytes, the electrolyte volume will increase with CO₂ pressure, hence we have termed these high-pressure organic electrolytes as CO₂-eXpanded Electrolytes (CXEs). In our previous report, we have shown that at multi-molar CO₂ concentrations the supporting electrolyte (tetrabutylammonium hexafluorophosphate) remains in solution and fast outer-sphere electron-transfers (e.g., ferrocene/ferrocenium) are supported in this media across a wide range of CO₂ concentrations. Most interestingly, we observed a non-monotonic trend between the rate of electrochemical reduction of CO₂ to CO on polycrystalline Au and CO₂ pressure in the CXE media. Specifically, we observed a maximum CO₂ reduction rate at a CO₂ pressure of 3.1 MPa. At pressures exceeding this optimum, the electrochemical CO₂ activity decreases to values similar to that of ambient pressure CO₂ reduction.

Here, we have set out to perform a micro-kinetic modelling study to understand the competing factors that give rise to this optimum in electrocatalytic activity. Understanding the mechanism and rate-determining steps for the electrochemical reduction of CO₂ under elevated CO₂ pressure is vital to the development of new catalysts and to the eventual industrial relevance of this technology.^{24,25}

4.2 Materials and Methods

Electrochemical data was collected in a custom pressure cell as previously described.²³ Briefly, a custom cap with threaded electrical feedthroughs was mated to a 50 mL Parr reactor to create the body of the cell. Pressure from a commercially supplied CO₂ bottle (Matheson, Research Grade) was used to pressurize the vessel. Electrochemical data was collected using a Gamry Reference 3000 Potentiostat/Galvanostat. Cyclic voltammogram data for CO₂ reduction on a gold microelectrode (0.000314 cm²) were used as published in Shaughnessy²³. Cyclic voltammograms on copper were collected using a 0.0177 cm² disk electrode (Alfa Aesar, 99.9%)

COMSOL (COMSOL Multiphysics v. 5.3) simulations were used to model the CO₂ electroreduction on the gold microelectrode. The simulated reactor geometry was created as a 2D axial-symmetric domain with the electrode size (100 μm radius), insulating sheath size (10 μm width) and reactor dimensions (1 cm radius, 2 cm height). A mesh with a free triangular mesh using COMSOL’s built-in “normal” element size was used for the bulk of the reactor, with an “extremely fine” mesh used for the area near the electrode (1.5mm x 2.5mm). An edge mesh was incorporated

with a maximum mesh element of 2×10^{-5} cm and a minimum mesh element of 2×10^{-6} cm for maximum resolution near the electrode. The current was simulated in the COMSOL Electroanalysis module. This module simulates the concentration of the oxidized and reduced species in solution and the current on the electro-active boundary as a function of applied potential by coupling the Butler-Volmer Equation with Fick's Law of Diffusion. The COMSOL Surface Reactions physics in the Chemical Reaction Engineering Module was used to model the CO_2 reduction. The potential dependent nature of the first and third reaction steps was taken into account by incorporating the Butler-Volmer equation into the rate expression.

For all simulations the diffusion coefficients at various expansions were used as calculated by Laird and coworkers.²⁶ The exact potential applied in the experiment was used in the simulation. The concentration of CO_2 in the bulk solution at the various pressures was found using data from Shaughnessy et al.²³ The resistances at various pressures were found using electrochemical impedance spectroscopy.

4.3 Results and Discussion

Several physical properties of CXE's (much like the chemocatalysis analogs CO_2 -eXpanded Liquids) can be tuned by changing the CO_2 head-space pressure. Figure 4.1 shows the progressive changes in several key properties that affect electrocatalytic rates as a function of CO_2 pressure. First, Figure 4.1a shows the volumetric expansion of the electrolyte as a function of CO_2 pressure. The expansion of the electrolyte occurs as CO_2 dissolves into the liquid phase. CO_2 is extremely soluble in acetonitrile, and as the head-space pressure increases above ca. 3 MPa, the solvent contains such high concentrations of CO_2 that the liquid-phase volume expands exponentially up-to three times its initial state. The concomitant increase in liquid-phase CO_2 concentration (as measured using previously described techniques) is shown in Figure 4.1b.²³ We observed that the concentration obtained in the CXE far exceeds what is possible in aqueous electrolytes. For example, given that the Henry's law constant of CO_2 in water is $0.034 \text{ mol kg}^{-1} \text{ bar}^{-1}$, the concentration of CO_2 in water is 1.0 M at 3 MPa and 1.7 M at 5 MPa. Whereas, in the CXE the concentrations are 5 M and 13 M at 3 MPa and 5 MPa, respectively. In fact, in the CXE media, the liquid-phase molar concentration CO_2 approaches that of pure liquid CO_2 (15.1 M) at pressures

exceeding 5 MPa. Note, when the CO₂ head-space pressure reaches the condensation pressure of CO₂ at the reaction temperature, the system then becomes biphasic with a layer of liquid CO₂ above the expanded liquid.

In addition to the concentration increasing with CO₂ head-space pressure, the diffusion coefficient of CO₂ also increases with CO₂ pressure. Figure 4.1c shows the diffusion coefficient for CO₂ in acetonitrile, computationally determined by Laird and coworkers.²⁶ As the expansion of the electrolyte begins to rapidly rise, the electrolyte becomes more “gas like” with a drop in viscosity. This change drives an increase in the diffusion coefficient.

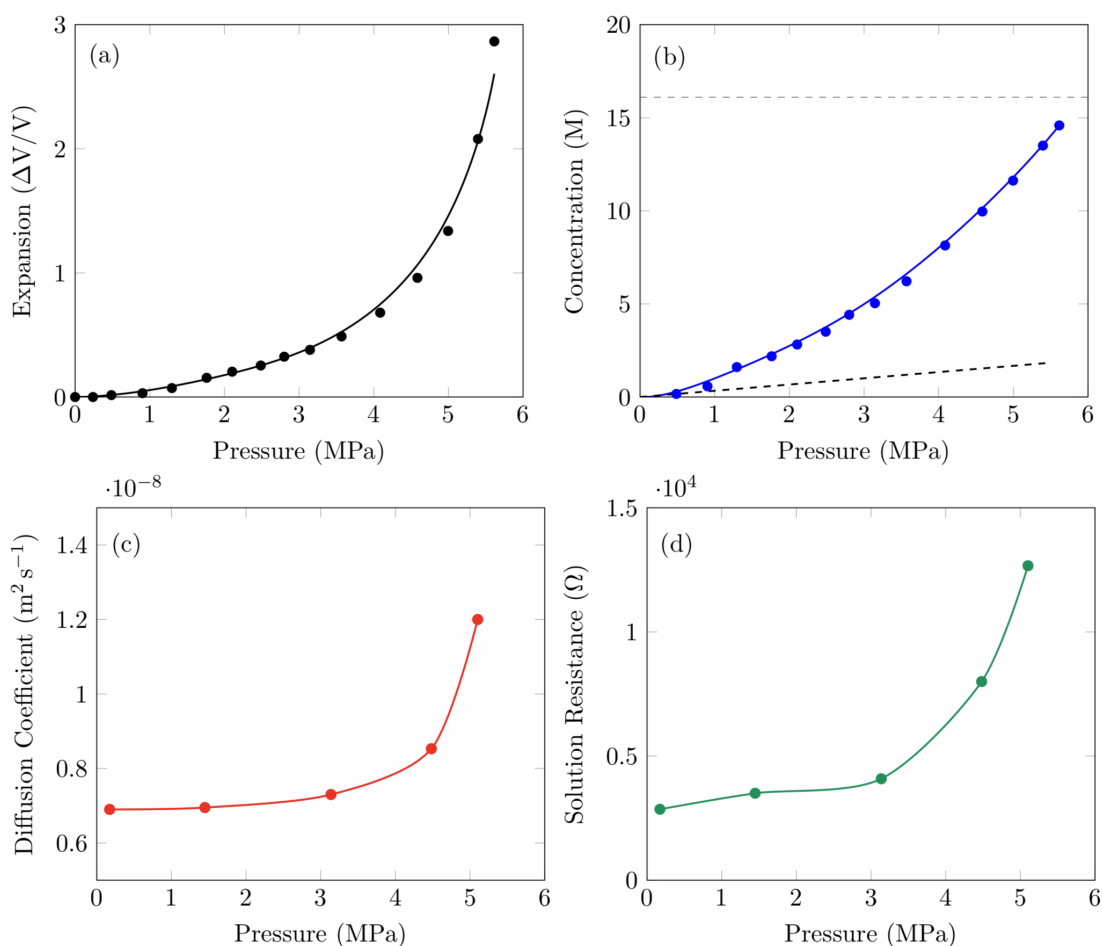


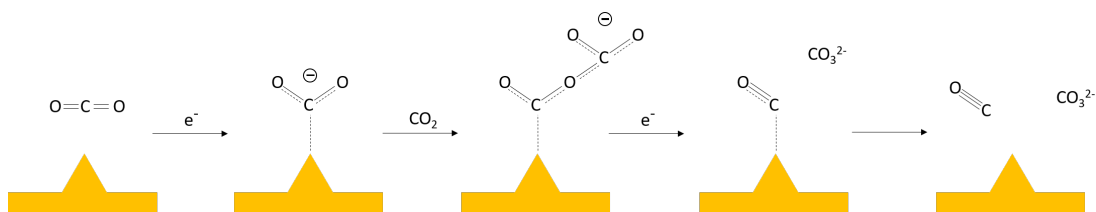
Figure 4.1. Pressure dependant properties of CO₂-eXpanded Electrolytes. (a) Volumetric Expansion, (b) CO₂ concentration, (c) Diffusion Coefficient of CO₂, (d) Solution resistance.

The increase in diffusion of CO₂ to the electrode surface and the increase in CO₂ concentration should provide an increase in the electrocatalytic rate of CO₂ conversion. However, in addition to these effects, we observed that the resistance of the system also increases as the head-space CO₂-

pressure increases as shown in 4.1d. The resistivity of the system at various pressures was measured by electrochemical impedance spectroscopy (SI Figs 4.10 - 4.12). This increase in resistance should have the opposite effect and inhibit the overall electron-transfer rates of electrochemical CO₂ reduction at high pressures.

Cyclic voltammograms for the electrochemical reduction of CO₂ as a function of CO₂-pressure for both polycrystalline gold and copper catalysts show that this non-monotonic relationship between CO₂ reduction activity and CO₂ pressure is a property of the acetonitrile-based CXE (Figure 4.2). For both electrode materials, we observed modest CO₂ reduction activity at near ambient CO₂ pressure(0.17 MPa). When the CO₂ pressure is increased to 3.13 MPa, there is dramatic increase in the measured current for electrochemical CO₂ reduction. When the pressure is increased further to 5.10 MPa, instead of the current increasing and then plateauing as catalytic sites became the limiting factor, there was a startling decrease in current at higher concentrations of CO₂. Catalytic current was seen to diminish to the same magnitude of current response found at near ambient pressures of CO₂. In addition, an apparent change in the onset potential was observed.

Deconvoluting the effects of each individual property changes is difficult. To accomplish this task we turned to COMSOL modeling. COMSOL modeling is typically used to model diffusion of species in complex environments. It also has the capability to model electrochemical reaction kinetics. To obtain an understanding of the system we decided to go beyond the typical one electron transfer approximation used in COMSOL to develop a micro-kinetic model which simulates each elementary reaction step in the electrocatalytic conversion of CO₂ to CO.



Scheme 4.1. Illustrative reaction mechanism for the electrochemical reduction of CO₂ on Au.

In the accepted mechanism for CO₂ reduction on polycrystalline gold in aprotic, nonaqueous media, the first step is the transfer of an electron to CO₂ to form CO₂ ·⁻ (Scheme 4.1).¹¹ This radical intermediate is stabilized by adsorption to the surface of the catalyst. A second CO₂ molecule then reacts with the adsorbed radical to form a OCOCO₂ ·⁻ species. A subsequent electron transfer then

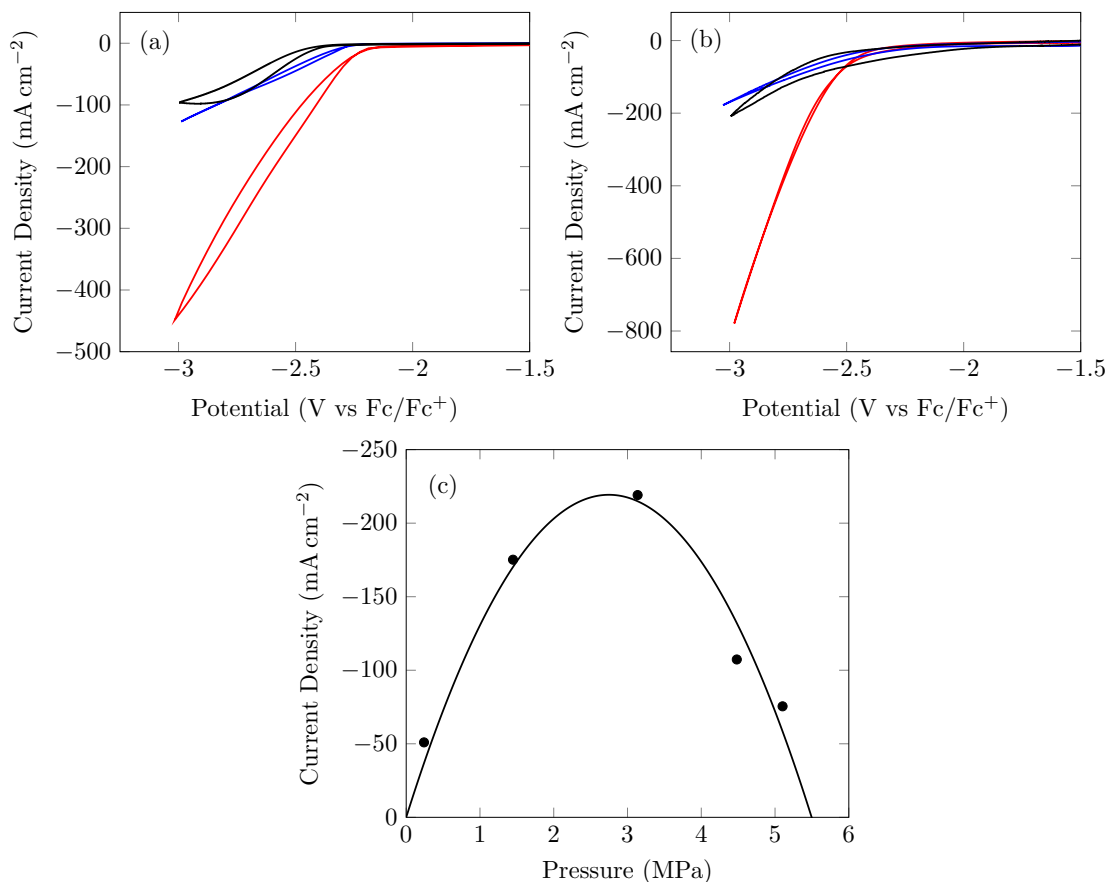


Figure 4.2. Pressure dependant cyclic voltammograms. (a) CO₂ reduction on polycrystalline Au, (b) CO₂ reduction on polycrystalline Cu, (c) Current density as a function of CO₂ pressure at -2.7 V.

forms free CO₃²⁻ and an adsorbed CO. With the desorption of this CO, the site is again available for catalysis. It should be noted, that this mechanism is not the traditional two-electron, two-proton transfer that typically occurs in aqueous electrolytes. Importantly, this model does not rely upon protons to be oxide acceptors. Thus, carbonate, which is a strong base under reaction conditions is free to produce protons via Hoffman degradation with the supporting TBAPF₆ electrolyte in a non rate determining step. However, because our reaction conditions attempt to be as devoid of proton as possible, this mechanism fully captures CO₂ reduction in the CXE media.

To perform the micro-kinetic model, we created a geometry in COMSOL that exactly mimics our experimental setup (SI. Figures 4.6 and 4.7). We simulated mass-transfer of CO₂ to and from the electrode surface using Fick's Diffusion. Our previous results on simulating outer-sphere 1-electron transfer show that Fick's Diffusion accurately captures mass-transfer of redox active species in the CXE environment. Table 4.1 shows the equations used to describe the reduction of CO₂ on

Table 4.1. Detailed mechanism for the electrochemical reduction of CO₂ on Au.

$\text{CO}_2 + \text{S}^* + \text{e}^- \xrightarrow{r_1} \text{CO}_2^{\bullet-}(\text{ads})$	$r_1 = k_1[\text{CO}_2][\text{S}^*]$	$k_1 = k_1^0 e^{-\alpha f(E-E^0)}$
$\text{CO}_2^{\bullet-}(\text{ads}) + \text{CO}_2 + \xrightarrow{r_2} \text{OCOCO}_2^{\bullet-}(\text{ads})$	$r_2 = k_2[\text{CO}_2^{\bullet-}(\text{ads})][\text{CO}_2]$	$k_2 = k_2$
$\text{OCOCO}_2^{\bullet-}(\text{ads}) + \text{e}^- \xrightarrow{r_3} \text{CO}(\text{ads}) + \text{CO}_3^{2-}$	$r_3 = k_3[\text{OCOCO}_2^{\bullet-}(\text{ads})]$	$k_3 = k_3^0 e^{-\alpha f(E-E^0)}$
$\text{CO}(\text{ads}) + \xrightarrow{r_4} \text{CO} + \text{S}^*$	$r_4 = k_4[\text{CO}]$	$k_4 = k_4$

Where k^0 = Electron transfer kinetic rate constant, α = The transfer coefficient, $f = F/RT$, $E =$ Applied Electrode Potential, $E^0 =$ Standard Potential

the electrode surface.

The rate of the first reaction step, electron transfer to and adsorption of CO₂ on the catalyst surface was taken to be first-order with respect to the concentration of CO₂ at the electrode surface and first-order with respect to the number of available sites, S* on the catalyst surface. Given the total site density, the model is able to calculate the number of available sites to calculate the rate of Reaction 1. The potential dependent nature of this reaction step taken into account by incorporating the irreversible Butler-Volmer equation into the rate expression, $k_1 = k_1^0 = e^{-\alpha f(E-E^0)}$, where k_1^0 is the electron-transfer rate constant, $\alpha = 0.3$ is the transfer coefficient, F is the Faraday constant, E is the potential of the electrode, E^0 is the reduction (set to -1.15V vs Fc/Fc⁺, C_{CO_2} is the concentration of CO₂ at the surface of the electrode, and SS is the concentration of surface sites.

The rate of the second reaction step, radical addition of the adsorbed CO₂·⁻ with CO₂ at the electrode surface to form OCOCO₂·⁻, is also taken to be first order in CO₂·⁻(ads) and first order in CO₂ concentration at the electrode surface. Here k_2 is the effective rate constant for Reaction 2 and is not potential dependent since it is not an electron-transfer reaction. The rate of the third reaction step, the electron transfer to the adsorbed OCOCO₂·⁻(ads) radical to form CO with the release of carbonate, and is taken to be first order in OCOCO₂·⁻(ads). Analogous to reaction 1, k_3 is dependent on the potential of the electrode per the irreversible Butler-Volmer reaction. Concluding the mechanism is the desorption of CO is which first order with respect to CO(ads).

Using this model, we can simulate the cyclic voltammetry data to regress the kinetic parameters for each reaction step as a function of CO₂ pressure. Here, we inputted into the model the known diffusion coefficients, concentrations of CO₂, scan rate, and resistances at each pressure. For each pressure we also used a transfer coefficient (α) of 0.3 and a site density of $1.2 \times 10^{-4} \text{ mol m}^{-2}$. We

then floated the k values for each reaction step as well as the E^0 for the first and third reaction steps. Using this method, we were able to obtain excellent fits of the voltammetry data for CO_2 pressures of 0.17, 1.44, 3.13, 4.48, and 5.10 MPa as shown in Figure 4.3. The known, as well as the regressed parameters are shown in Table 4.2

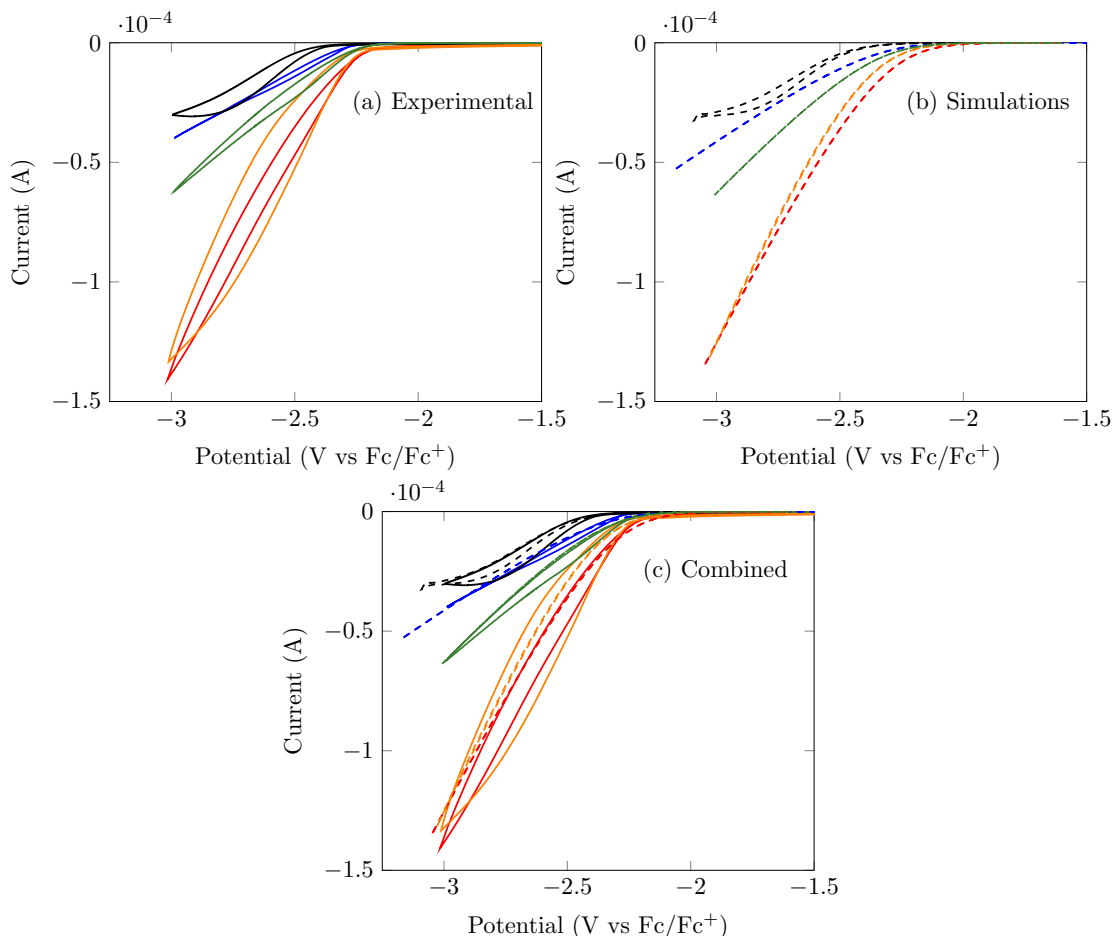


Figure 4.3. (Pressure dependant cyclic voltammograms for the electrochemical reduction of CO_2 on Au. (a) Experimental, (b) Simulated, (c) Combined. (Black 0.17 MPa, Orange 1.44 MPa, Red 3.13 MPa, Green 4.48 MPa, Blue 5.10 MPa

The model, incorporating all the known and regressed parameters, reveals several important points for future development of CO_2 electrochemical reduction systems. First, the obvious answer that the increasing resistance is the culprit for the decreased catalysis is not the whole story. The increased resistance is responsible for the decrease in the slope of the catalytic wave but is not responsible for the change in the onset potential to more negative potentials. (Supporting Fig 4.9) Secondly, as expected, the rate constants for the second, third, and fourth elementary reaction steps

Table 4.2. Input and regressed parameters for the COMSOL model.

Pressure Dependent Parameters (*Input Parameters †Regressed Parameters)				
Pressure	C_0 [M]*	D [m ² s ⁻¹]*	R_{sol} [Ω]*	k_1^0 [m ³ mol ⁻¹ s ⁻¹] [†]
0.17 MPa	0.08	6.9×10^{-9}	2856	2×10^{-8}
1.44 MPa	1.47	6.95×10^{-9}	3500	2×10^{-8}
3.13 MPa	5	7.3×10^{-9}	4085	2×10^{-8}
4.48 MPa	9.64	8.52×10^{-9}	8000	0.2×10^{-8}
5.10 MPa	13	12×10^{-9}	12666	0.1×10^{-8}
Parameters Constant for All Pressures				
$E_1^0 = -1.15$ V; $E_3^0 = -1.15$ V; $\alpha = 0.3$; $k_2 = 100$ m ³ mol ⁻¹ s ⁻¹ ; $k_3 = 8 \cdot 10^{-5}$ s ⁻¹ ; $k_4 = 500$ s ⁻¹ Site density 1.2×10^{-4} mol m ⁻²				

are constant over the pressure range tested. Also, the E_1^0 and E_2^0 do not change as the concentration of CO₂ due to CO₂ reduction gold catalyst being highly irreversible. Unexpectedly, the first rate constant (k_1^0) is not constant as a function of pressure, but in fact decreases with increasing CO₂ pressure. The order of magnitude drop (Fig. 4.4) in k_1^0 at high concentrations of CO₂ is the driver in the negative shift in the onset potential.

To show the sensitivity of the system to changes of the various individual kinetic rates, simulations across five orders of magnitude were carried out at 0.17, 3.13, and 5.10 MPa for all rate constants (Supporting Figure fgr:ks). It was found that k_1 changes the observed onset potential for all pressures. The effect of k_2 varies with the concentration of CO₂. At low concentrations the effect of k_2 is much more pronounced than at high concentrations where the overabundance of CO₂ at the electrode surface reduces the effect of any change in the rate constant. Changes in k_3 are unimportant at low concentrations of CO₂ when there are sites readily available. k_3 can become a limiting rate as the surface sites become more saturated with CO₂ at higher pressures. k_4 can only be a limiter in the process but cannot accelerate it.

Qualitatively, that a change in the reaction rate of the first reaction step will change the overall reaction rate is obvious. The first electron transfer to create the charged intermediate is thermodynamically the most difficult. Thus this step is considered to be the rate limiting step, so a decrease in this rate will impede the rest of the process. Why the rate should decrease however, is more nonintuitive.

We believe that the change in the environment at the surface of the electrode that occurs when the polar acetonitrile in solution becomes displaced by the increase in concentration of nonpolar CO₂ is the reason for this decrease. As the amount of CO₂ near the surface of the electrode increases, the decrease in the polarity means that the transition state when the charged intermediate forms is

less supported by the partial charges. When the amount of acetonitrile near the surface decreases to a certain point, the transition is no longer adequately supported. This makes the transition more difficult which is then reflected in the rate constant.

The major conclusion from this modelling work, is it definitely shows the optimum pressure at which to operate any heterogeneous electrocatalysts in an acetonitrile-based electrolyte—ca. 3 MPa, which is right at the onset of major electrolyte expansion. At pressures below this optimum, the increase in CO₂ pressure outweighs any inhibitions due to the larger solution resistance. However, once the electrolyte begins to expand significantly (i.e. at pressures above 3 MPa), the decrease in the electron-transfer rate constant, and the increase in solution resistance outweigh any benefits from the increase in CO₂ concentration (Figure 4.4).

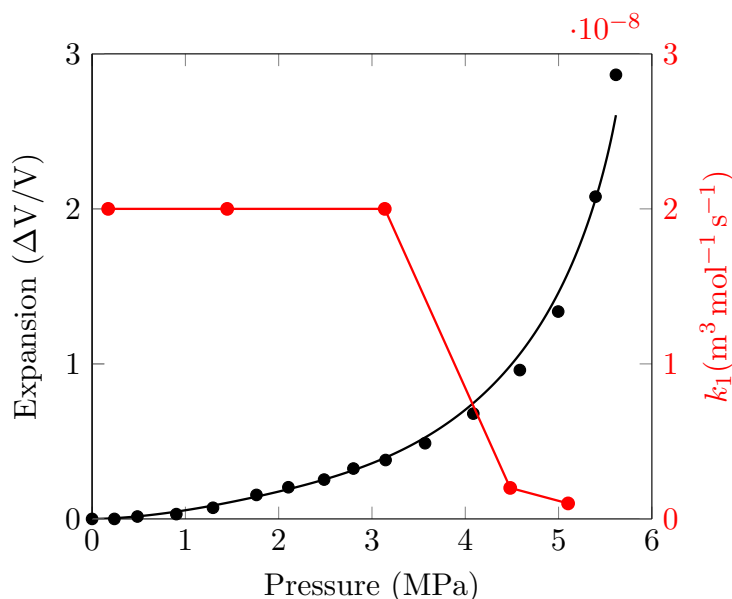


Figure 4.4. Relationship between volumetric expansion and k_1 as a function of CO₂ pressure

4.4 Conclusion

This is the first time that a rate constant for the electrochemical reduction of CO₂ on gold has been evaluated in a medium that has progressively changing polarity. These results raise the question of how to best tune the effective rate constant by changing the polarity of the solvent. It is possible that with a different solvent the decrease in rate constant could be pushed out to higher concentrations of CO₂. This would enable even higher rates of reaction.

The existence of an optimum CO_2 concentration to avoid a decrease in k_1^0 while ensuring the largest supply of CO_2 to the surface possible, regardless of the reason, has important implications for designing electrochemical CO_2 reduction systems. This inflection point means that there is an upper limit to the amount of CO_2 desirable in solution for maximum catalytic rates. This indicates that operating electrochemical reduction catalysts in liquid CO_2 , quite aside from any concerns about resistivity, would be contraindicated for optimal rates of reaction. Moreover, we have shown that this optimum pressure (3.13 MPa) is quite mild compared to many industrial processes, making the use of CXEs for electrochemical CO_2 reduction in organic media an important area to investigate further.

4.5 Supporting Information

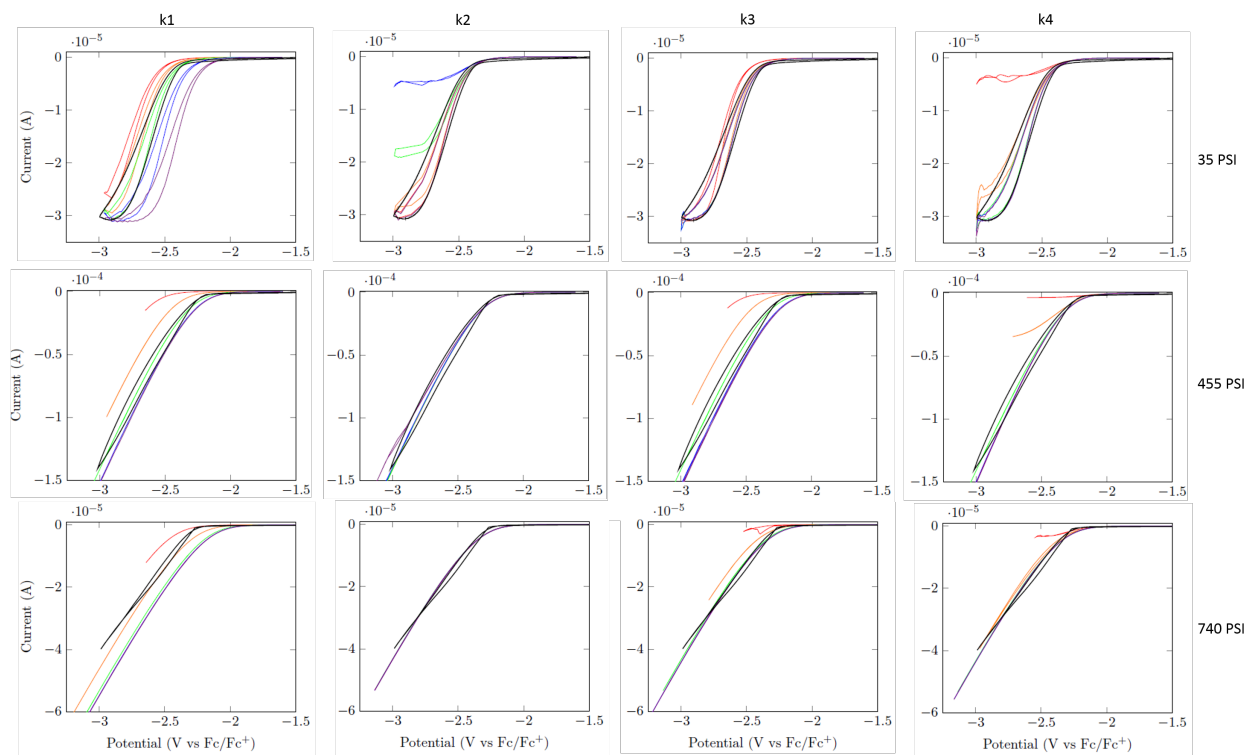


Figure 4.5. Model sensitivity for the elementary rates of reaction over five orders of magnitude. (**k1:** Red: 2×10^{-10} Orange: 2×10^{-9} , Green: 2×10^{-8} Blue: 2×10^{-7} Violet: $2 \times 10^{-6} \text{ mol}^{-1} \text{ s}^{-1} \text{ m}^3$)(**k2:** Red: 1×10^3 Orange: 1×10^2 Green: 1×10^1 , Blue: 1 Violet: $1 \times 10^{-1} \text{ mol}^{-1} \text{ s}^{-1} \text{ m}^3$)(**k3:** Red: 8×10^{-7} Orange: 8×10^{-6} Green: 8×10^{-5} Blue: 8×10^{-4} Violet: $8 \times 10^{-3} \text{ s}^{-1}$)(**k4:** Red: 5 Orange: 5×10^1 Green: 5×10^2 Blue: 5×10^1 Violet: $5 \times 10^4 \text{ s}^{-1}$) Black: Experimental for all cases

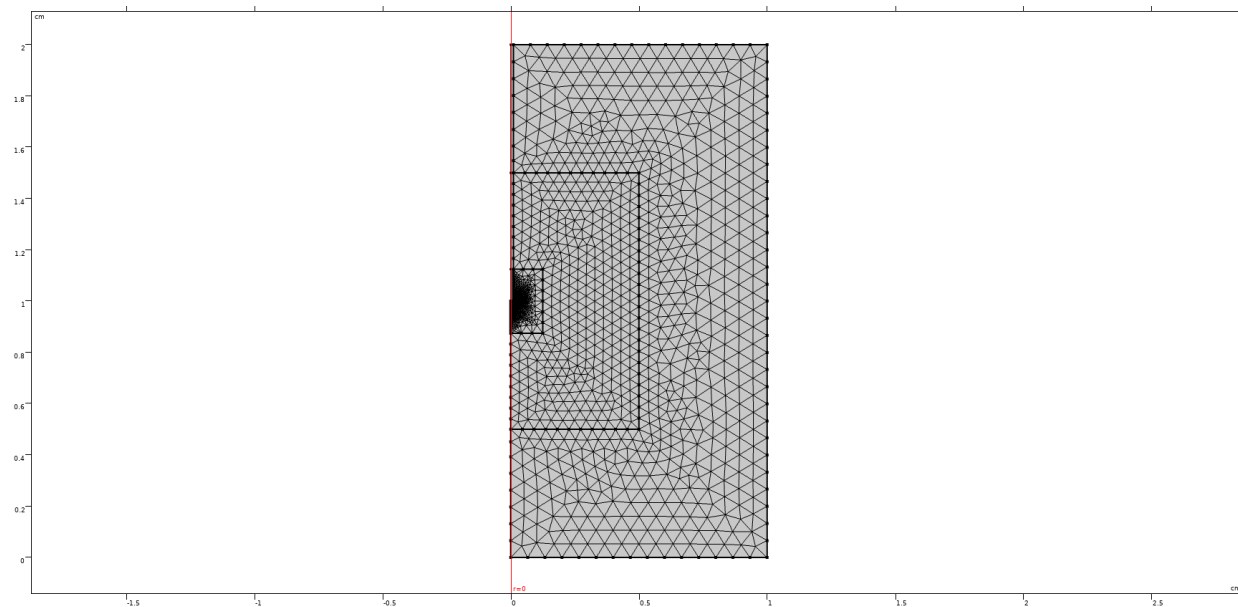


Figure 4.6. Comsol mesh reproducing the geometry of the reactor for CO₂ reduction simulations

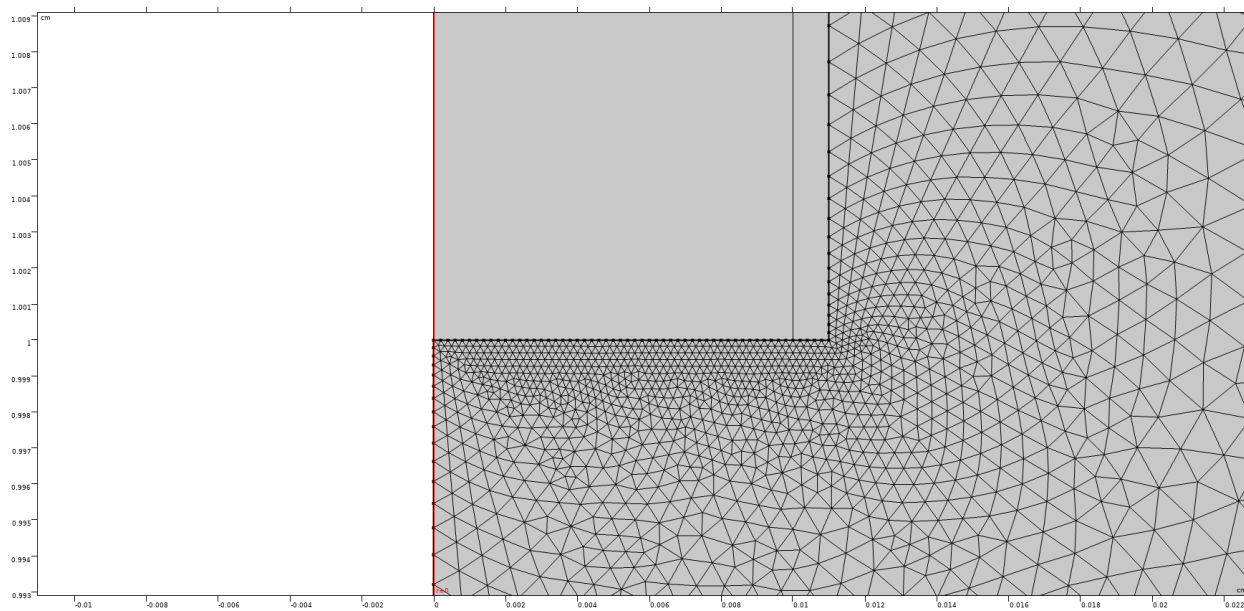


Figure 4.7. Comsol mesh reproducing the geometry of the reactor for CO₂ reduction simulations zoomed into the area around the electrode

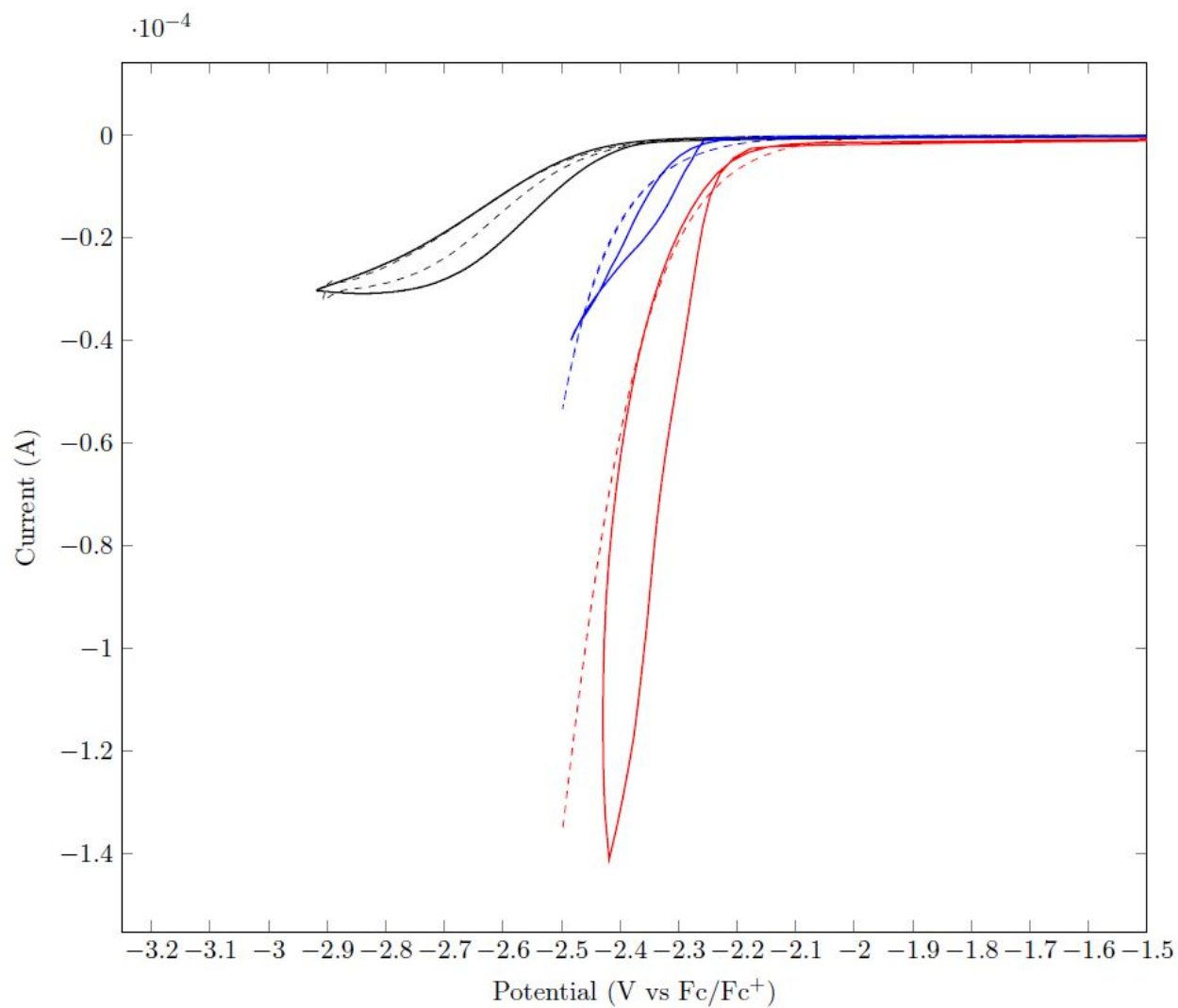


Figure 4.8. Cyclic voltammograms for CO₂ reduction on gold in CXEs corrected for resistance. (Red: 3.13 Mpa, Blue: 5.10 MPa, Black: 0.17 MPa, Solid: Experimental with IR correction, Dashed: Simulated with IR correction)

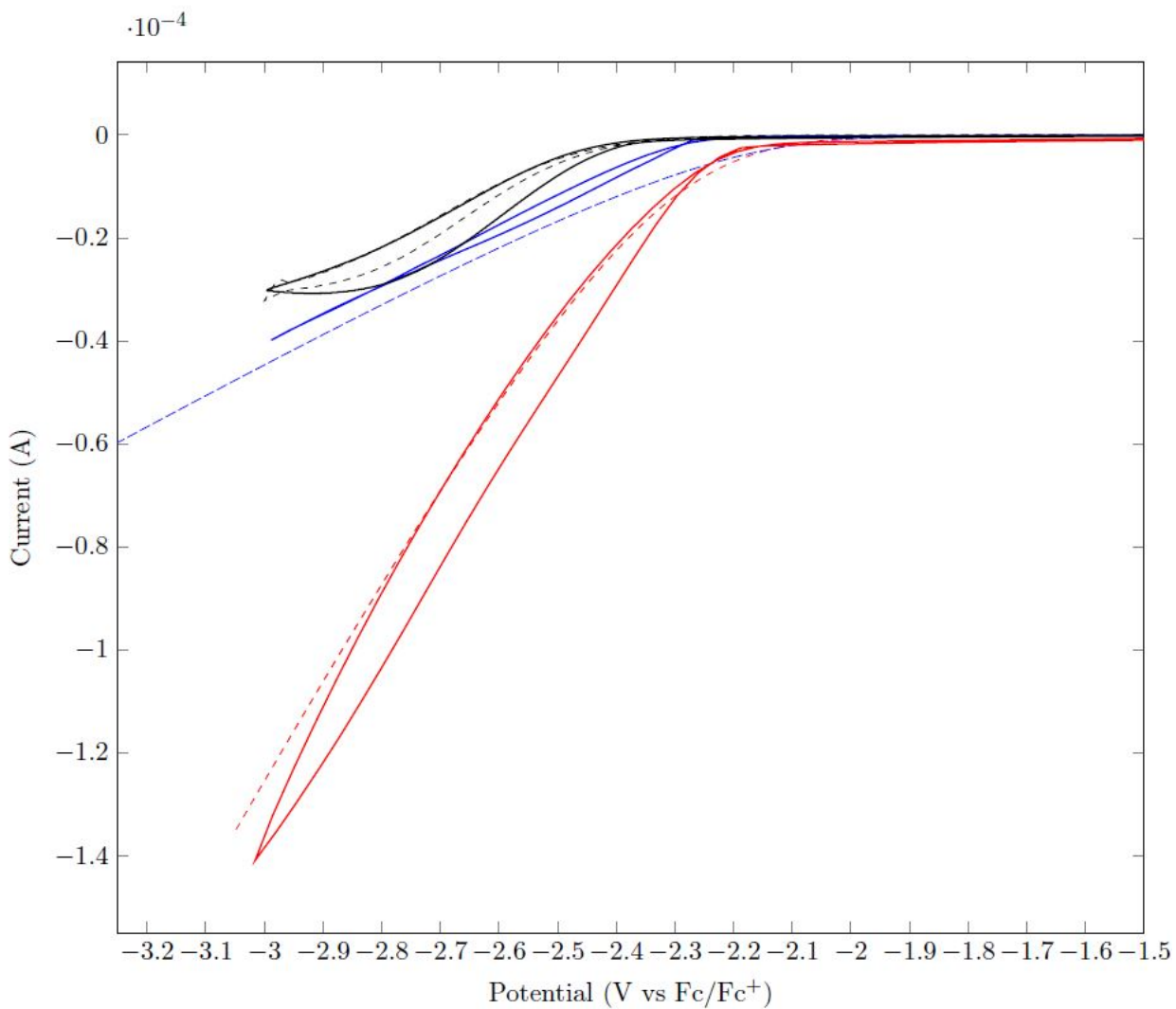


Figure 4.9. Utilizing the calculated k_1 for atmospheric $[\text{CO}_2]$ for all pressures (Red: Simulated 3.13 Mpa, Orange: Simulated 0.17 MPa, Green: Simulated 5.10 MPa, Black: Experimental at all presures)

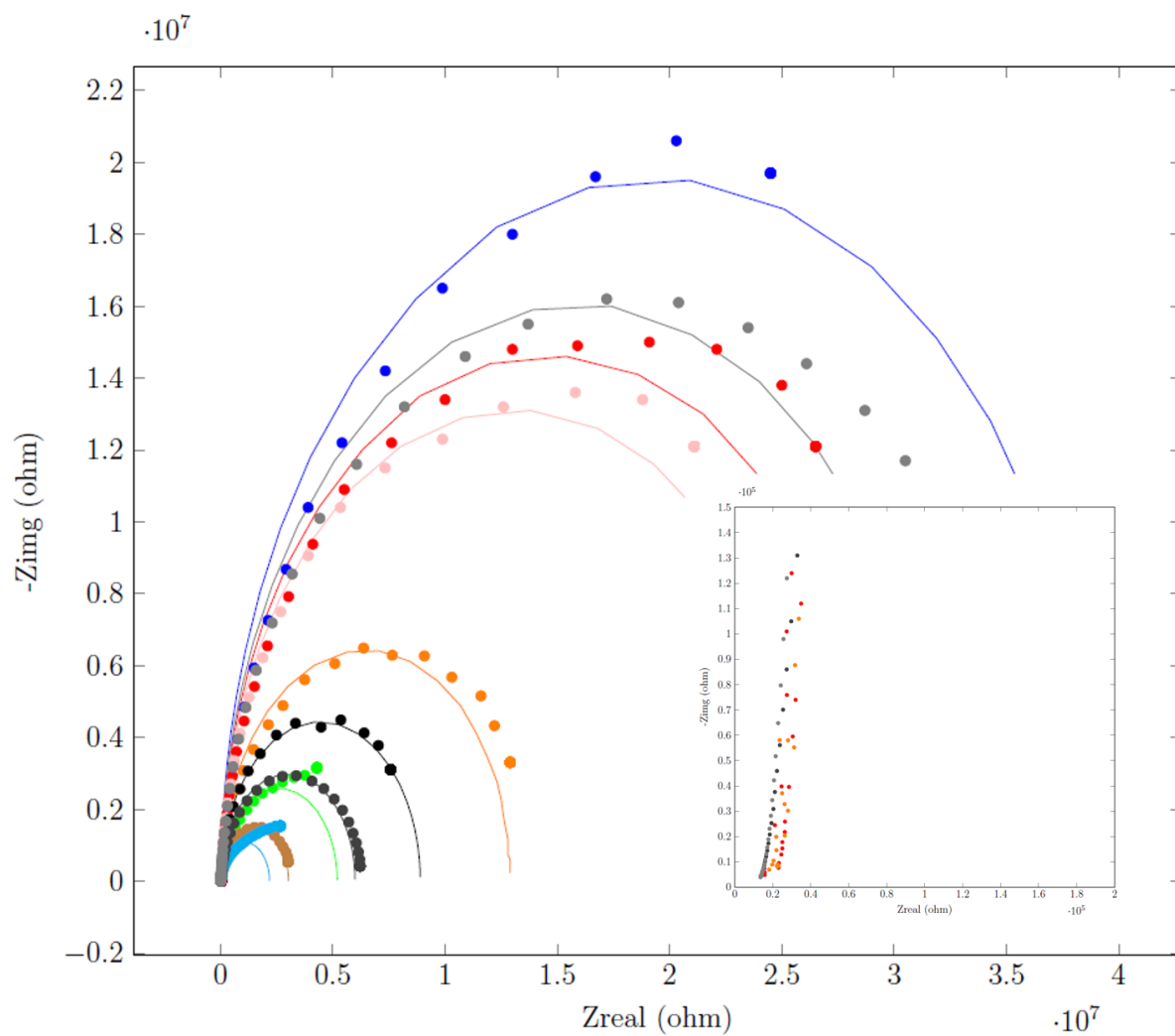


Figure 4.10. EIS data and fits for 5.10 MPa CO₂ on 200 μm diameter Au disk electrode. Insert is a zoom of region critical for finding solution resistance.

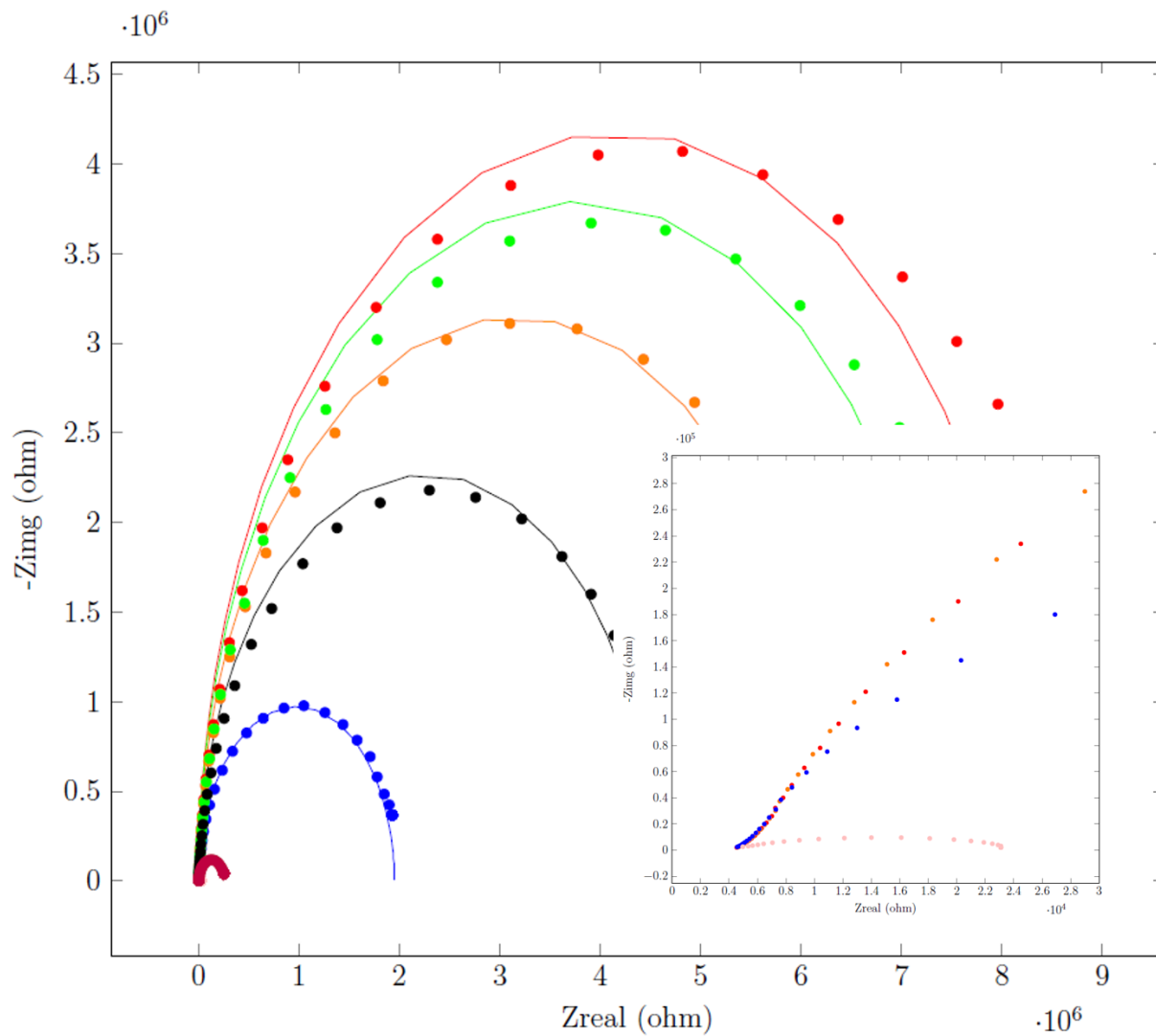


Figure 4.11. EIS data and fits for 3.13 MPa CO₂ on 200 μm diameter Au disk electrode. Insert is a zoom of region critical for finding solution resistance.

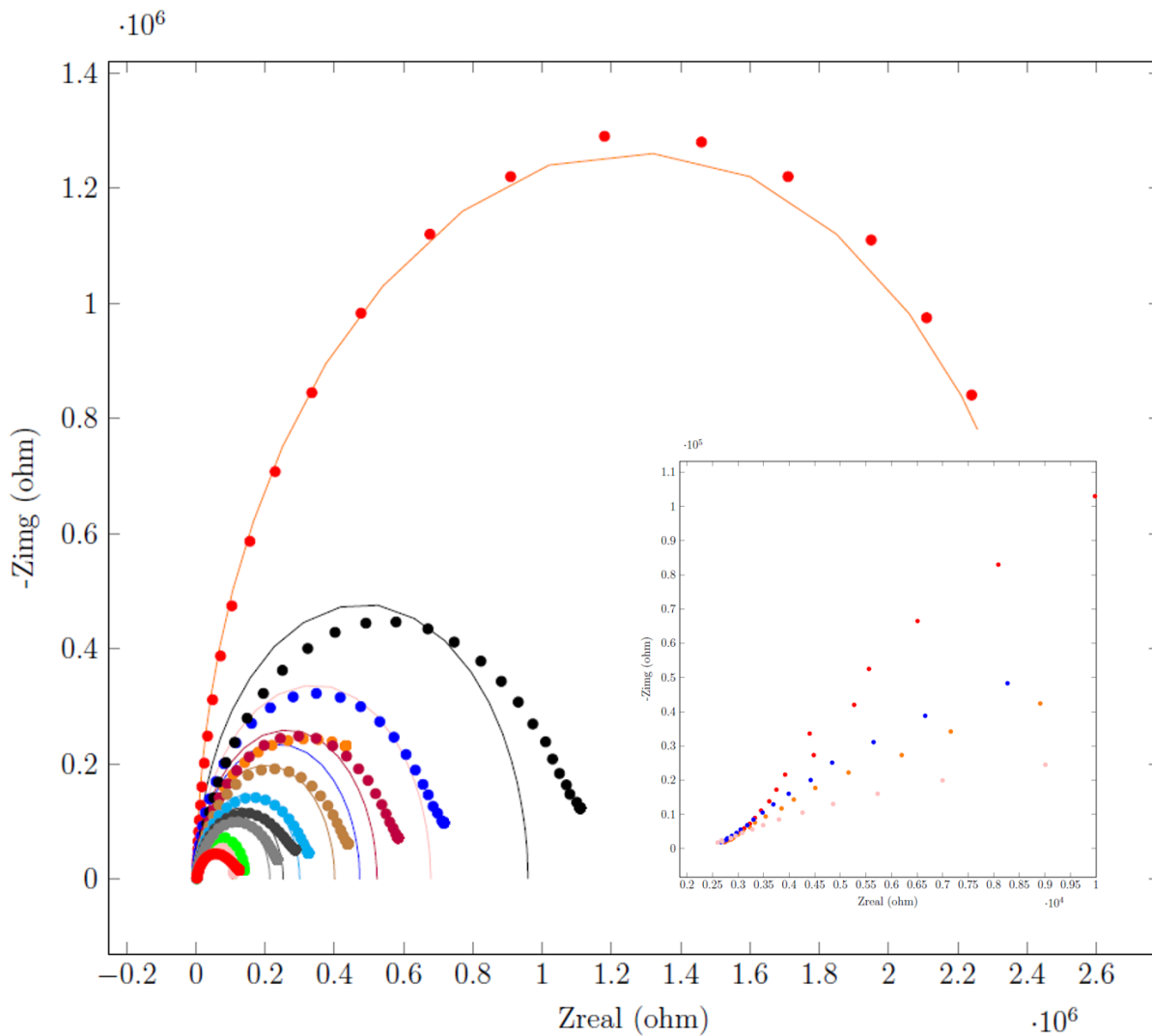


Figure 4.12. EIS data and fits for 0.17 MPa CO₂ on 200 μm diameter Au disk electrode. Insert is a zoom of region critical for finding solution resistance.

References

- [1] Appel, A. M. et al. (2013) Frontiers, Opportunities, and Challenges in Biochemical and Chemical Catalysis of CO₂ Fixation. *Chemical Reviews* 113, 6621–6658, PMID: 23767781.
- [2] Montoya, J. H., Seitz, L. C., Chakhranont, P., Vojvodic, A., Jaramillo, T. F., and Nørskov, J. K. (2017) Materials for solar fuels and chemicals. *Nature materials* 16, 70.
- [3] Fiorani, G., Guo, W., and Kleij, A. W. (2015) Sustainable conversion of carbon dioxide: the advent of organocatalysis. *Green Chemistry* 17, 1375–1389.
- [4] DuBois, D. L. (2014) Development of molecular electrocatalysts for energy storage. *Inorganic chemistry* 53, 3935–3960.
- [5] Whipple, D. T., and Kenis, P. J. A. (2010) Prospects of CO₂ Utilization via Direct Heterogeneous Electrochemical Reduction. *The Journal of Physical Chemistry Letters* 1, 3451–3458.
- [6] Zhu, D. D., Liu, J. L., and Qiao, S. Z. (2016) Recent advances in inorganic heterogeneous electrocatalysts for reduction of carbon dioxide. *Advanced materials* 28, 3423–3452.
- [7] Costentin, C., Robert, M., and Saveant, J.-M. (2013) Catalysis of the electrochemical reduction of carbon dioxide. *Chemical Society Reviews* 42, 2423–2436.
- [8] Qiao, J., Liu, Y., Hong, F., and Zhang, J. (2014) A review of catalysts for the electroreduction of carbon dioxide to produce low-carbon fuels. *Chemical Society Reviews* 43, 631–675.
- [9] Chen, Y., Lewis, N. S., and Xiang, C. (2015) Operational constraints and strategies for systems to effect the sustainable, solar-driven reduction of atmospheric CO₂. *Energy & Environmental Science* 8, 3663–3674.

- [10] Duan, Z., and Sun, R. (2003) An improved model calculating CO₂ solubility in pure water and aqueous NaCl solutions from 273 to 533 K and from 0 to 2000 bar. *Chemical geology* 193, 257–271.
- [11] Hori, Y. i. *Modern aspects of electrochemistry*; Springer, 2008; pp 89–189.
- [12] Whipple, D. T., Finke, E. C., and Kenis, P. J. (2010) Microfluidic reactor for the electrochemical reduction of carbon dioxide: the effect of pH. *Electrochemical and Solid-State Letters* 13, B109–B111.
- [13] Verma, S., Hamasaki, Y., Kim, C., Huang, W., Lu, S., Jhong, H.-R. M., Gewirth, A. A., Fujigaya, T., Nakashima, N., and Kenis, P. J. (2017) Insights into the Low Overpotential Electroreduction of CO₂ to CO on a Supported Gold Catalyst in an Alkaline Flow Electrolyzer. *ACS Energy Letters* 3, 193–198.
- [14] Cook, R. L., MacDuff, R. C., and Sammells, A. F. (1990) High rate gas phase CO₂ reduction to ethylene and methane using gas diffusion electrodes. *Journal of The Electrochemical Society* 137, 607–608.
- [15] Furuya, N., Yamazaki, T., and Shibata, M. (1997) High performance Ru-Pd catalysts for CO₂ reduction at gas-diffusion electrodes. *Journal of Electroanalytical Chemistry* 431, 39–41.
- [16] Endrődi, B., Bencsik, G., Darvas, F., Jones, R., Rajeshwar, K., and Janáky, C. (2017) Continuous-flow electroreduction of carbon dioxide. *Progress in Energy and Combustion Science* 62, 133–154.
- [17] Chen, Y., Li, C. W., and Kanan, M. W. (2012) Aqueous CO₂ Reduction at Very Low Overpotential on Oxide-Derived Au Nanoparticles. *Journal of the American Chemical Society* 134, 19969–19972, PMID: 23171134.
- [18] Lee, H.-E., Yang, K. D., Yoon, S. M., Ahn, H.-Y., Lee, Y. Y., Chang, H., Jeong, D. H., Lee, Y.-S., Kim, M. Y., and Nam, K. T. (2015) Concave rhombic dodecahedral Au nanocatalyst with multiple high-index facets for CO₂ reduction. *ACS nano* 9, 8384–8393.

- [19] Mistry, H., Reske, R., Zeng, Z., Zhao, Z.-J., Greeley, J., Strasser, P., and Cuenya, B. R. (2014) Exceptional size-dependent activity enhancement in the electroreduction of CO₂ over Au nanoparticles. *Journal of the American Chemical Society* *136*, 16473–16476.
- [20] Mostafa, S., Behafarid, F., Croy, J. R., Ono, L. K., Li, L., Yang, J. C., Frenkel, A. I., and Cuenya, B. R. (2010) Shape-dependent catalytic properties of Pt nanoparticles. *Journal of the american chemical society* *132*, 15714–15719.
- [21] Zhu, W., Zhang, Y.-J., Zhang, H., Lv, H., Li, Q., Michalsky, R., Peterson, A. A., and Sun, S. (2014) Active and selective conversion of CO₂ to CO on ultrathin Au nanowires. *Journal of the American Chemical Society* *136*, 16132–16135.
- [22] Feng, X., Jiang, K., Fan, S., and Kanan, M. W. (2015) Grain-boundary-dependent CO₂ electroreduction activity. *Journal of the American Chemical Society* *137*, 4606–4609.
- [23] Shaughnessy, C. I., Sconyers, D. J., Kerr, T. A., Lee, H.-J., Subramaniam, B., Leonard, K. C., and Blakemore, J. D. (2018) Enhanced Electrocatalytic CO₂ Conversion in Pressure-Tunable CO₂ Expanded Electrolytes. *Unpublished*
- [24] Montoya, J. H., Shi, C., Chan, K., and Nørskov, J. K. (2015) Theoretical insights into a CO dimerization mechanism in CO₂ electroreduction. *The journal of physical chemistry letters* *6*, 2032–2037.
- [25] Rosen, J., Hutchings, G. S., Lu, Q., Rivera, S., Zhou, Y., Vlachos, D. G., and Jiao, F. (2015) Mechanistic insights into the electrochemical reduction of CO₂ to CO on nanostructured Ag surfaces. *Acs Catalysis* *5*, 4293–4299.
- [26] Houndonougbo, Y., Laird, B. B., and Kuczera, K. (2007) Transport properties of CO₂-expanded acetonitrile from molecular dynamics simulations. *The Journal of chemical physics* *126*, 074507.

Chapter 5

Insights Into the Kinetics of $\text{Re}(\text{CO})_3(\text{bpy})\text{Cl}$ for the Electrochemical Reduction of CO_2 in CO_2 Expanded Electrolytes

5.1 Abstract

The kinetic understanding for electrochemical CO_2 reduction of homogeneous catalysts has been limited by the difficulty in adjusting the concentration of CO_2 in conventional aqueous solvents. CO_2 Expanded Electrolytes (CXEs) have the ability to tunably solvate multi-molar amounts of CO_2 . The kinetics of an extensively characterized homogeneous catalyst, $\text{Re}(\text{CO})_3(\text{bpy})\text{Cl}$, were investigated by utilizing this tunability to generate cyclic voltammograms at widely separated concentrations of CO_2 . The observed rates increased until a plateauing rate with increasing concentration of CO_2 . These rates match well with the Michealis-Menten model for enzymatic catalysis. Using the Michealis-Menten equation, the kinetic rate constant for electrochemical reduction was found. After the plateau a reduction in the catalytic rate was observed at the highest degree of expansion, consistent with what has previously been observed for heterogeneous catalysts. The use of CXEs to investigate the relationship between CO_2 concentration and catalytic rate will guide

the future development of electrochemical CO₂ reduction systems.

5.2 Introduction

The rising levels of CO₂ in the atmosphere and their concomitant effects on the environment have prompted considerable interest in methods to mitigate or reduce emissions. One method that seems promising is the electrochemical reduction of CO₂ to value added chemicals. This approach is attractive because it can operate at ambient temperatures and can readily be powered by renewable sources such as solar or wind. Unfortunately the industrial adoption of this technique is hampered by a, thus far, unsolved problem. For electrochemical conversion the CO₂ must be dissolved in a conductive media. In most solvents the solubility of CO₂ is too low to support high current densities. Recently it has been demonstrated that CO₂ eXpanded Electrolytes (CXEs) can overcome this limitation for heterogeneous catalysts.¹ We now demonstrate that it is possible to utilize CXEs to increase the CO₂ concentration available to a homogeneous catalyst in CXEs. In addition, we also show that the tunability of the CXE media allows an investigation into the intrinsic kinetics of CO₂ reduction with homogeneous catalysts.

The catalyst selected to show the increase in rate possible for homogeneous catalysts through using CXEs is Re(CO)₃(bpy)Cl. This catalyst was selected for this study due to the extensive studies carried out for both it and its derivatives in both photochemical and electrochemical reduction of CO₂.²⁻¹² Fairly stable in air, this family of catalysts are known to be selective for the conversion of CO₂ to CO. The extensive characterization of this catalyst gives a good baseline to evaluate the effectiveness of CXEs upon the catalysis for a homogeneous, molecular system. However, this catalyst has not previously been studied for electrocatalytic reduction of CO₂ at high concentrations of CO₂ due to the difficulty in increasing the concentration of CO₂ in conventional solvents. In line with other electrocatalysts, this difficulty in increasing CO₂ concentrations forces limited current density due to diffusion of the CO₂ from the bulk to the surface of the electrode.

In addition, the normal method to understand the kinetics of a catalyst through manipulating substrate concentration has been unavailable. Previously Smieja and Kubiak have worked on overcoming this limitation via electrochemical modeling software. They established the rate constant to be 1000 M⁻¹s⁻¹ for this catalyst in CO₂ saturated acetonitrile at ambient pressure.⁸ The

ability of CXEs to tunably increase CO₂ concentrations will contribute to overcoming the problem of diffusion to the surface of the electrode. In addition it will open a new pathway to understand catalysts for CO₂ reduction.

5.3 Experimental

5.3.1 Reactor

All experiments were carried out in a custom built high pressure electrochemical cell previously described in Shaughnessy et al.¹ Briefly, a custom cap was constructed for a 50 mL Parr reactor. Feedthroughs were threaded into the cap to allow electrical contact, and electrodes were attached to the feedthroughs by gold coated clips.

5.3.2 Materials

Re(CO)₃(bpy)Cl was synthesized via methods previously described by Lehn and coworkers.¹³ Tetrabutylammonium hexafluorophosphate (TBAPF₆) (Oakwood Chemical) was purified by recrystallization from ethanol. Acetonitrile was purified by a Pure Process Technology solvent system and stored over molecular sieves to exclude water. Electrochemical experiments were conducted with the basal plane of highly oriented pyrolytic graphite (HOPG) (GraphiteStore.com, Buffalo Grove, Ill.; A = 0.09 cm²). A copper wire (Alfa Aesar, 99.9%, 1.5mm diameter) immersed in electrolyte was used as a pseudo-reference in these experiments and stored in a separate, fritted chamber (Vycor frit, Bioanalytical Systems, Inc.) from the working solution. The counter electrode in all experiments was a platinum wire (Kurt J. Lesker, Jefferson Hills, PA; 99.99%, 0.5 mm diameter).

5.3.3 Electrochemical reaction procedures

Electrolyte containing Re(CO)₃(bpy)Cl and ferrocene was loaded into the electrochemical reactor under an argon atmosphere in a glovebag. Prior to experiments, the reactor was purged three times by repeated pressurization and depressurization cycles (ca. 800 kPa to 200 kPa) to exclude trace water and oxygen from the system. To achieve CO₂ equilibrium, the reactor was brought to the required pressure, stirred only until equilibrium was established, and then closed off from the gas supply. Electrolyte solution was quiescent during all electrochemical measurements. Reactor

pressurization was carried out with high-pressure CO₂ gas from a commercial cylinder (Matheson, Research Grade CO₂, 99.999%, 5.52 MPa).

5.3.4 Product detection by gas chromatography

Bulk electrolysis experiments were carried out with the rhenium catalyst over a five hour time period at a potential of -2 V vs. Fc⁺⁰, and across various pressures, in order to begin assaying the selectivity and efficiency of the system for CO₂ reduction to CO.

For product detection experiments following electrolysis, gas contained within both the expanded liquid and reactor headspace was collected by expansion of the headspace into an evacuated steel cylinder. At low pressures (<0.5 MPa), a 40 mL vessel was used and at high pressures a 1 L vessel was used. The connection of the larger volume reverses the expansion of the liquid due to the drop in pressure to near-ambient (typically 100-900 kPa) pressures. This method allows for a gas sample to be taken that is representative of all gas present in the system. The pressure and temperature of the system were allowed to equilibrate before closing the connection and removing the cylinder for analysis.

Analysis of gas samples was performed with a Shimadzu GC-2014 Custom-GC gas chromatograph with a thermal conductivity detector and dual flame-ionization detectors. A custom set of 8 columns and timed valves enable quantitative analysis of the following gases: hydrogen, nitrogen, oxygen, carbon dioxide, carbon monoxide, methane, ethane, ethylene, and ethyne. Argon serves as the carrier gas. The instrument was calibrated prior to experimental runs with a standard checkout gas mixture (Agilent 5190-0519) to obtain qualitative information regarding detection of H₂ and CO. Calibration curves over a range of 100–10,000 ppm for H₂ and 90–9,000 ppm for CO were constructed with prepared mixtures of H₂ or CO in N₂ to enable quantitative measurements. Quantification was accomplished using gas handling that accounts for sample dilution during post-electrolysis gas collection. These methods were carried out assuming that all gases involved behave as ideal gases. This is a reasonable assumption, as the pressure of the system at all times during these manipulations was < 900 kPa.

5.4 Results and Discussion

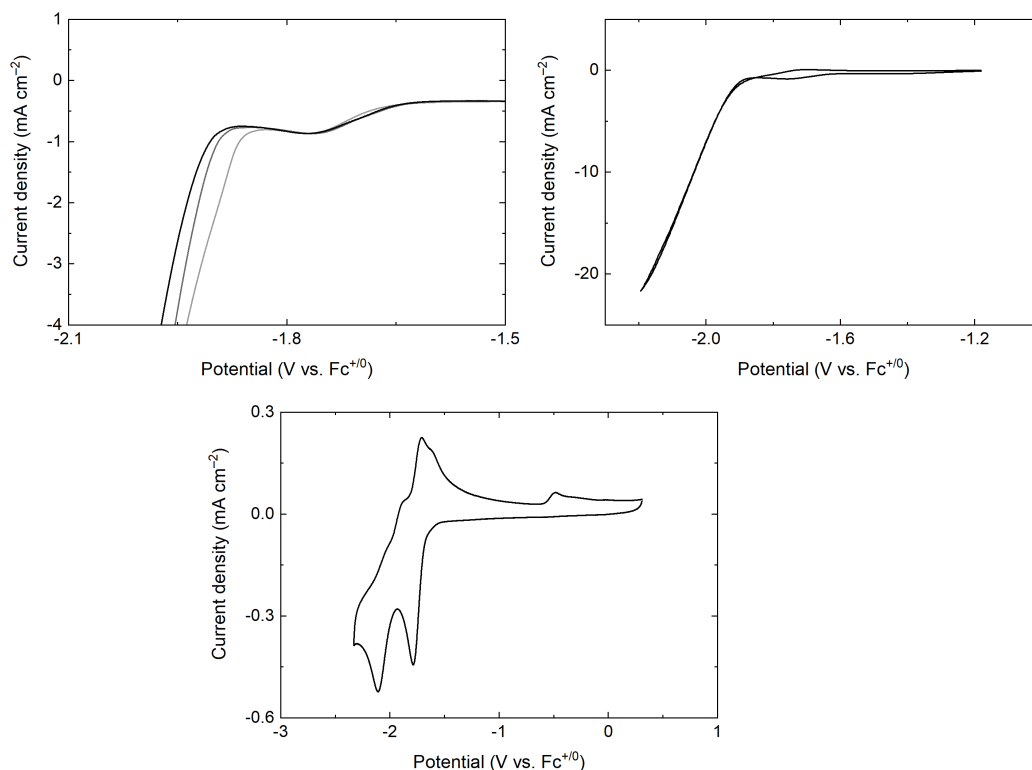


Figure 5.1. Cyclic voltammetry of the rhenium catalyst. (upper left) Forward sweep of cyclic voltammetry experiments performed on the rhenium system at various pressures (black 0.44 MPa, dark gray 0.61 MPa, light gray 0.79 MPa). The initial visible reduction event ($E_{p,c} = -1.75$ V) corresponds to a primarily ligand-centered reduction of the [Re] complex, after which the onset of catalysis is observed. A kinetic potential shift can be seen in the data, where with increasing pressure (and concomitantly concentration of CO_2), the onset potential of catalysis is moving toward more positive values. (upper right) Full range of the voltammetry at 0.44 MPa. (lower) Reversible electrochemistry of the rhenium catalyst in the absence of CO_2 , at ambient conditions inside a glovebox. All experiments were conducted with 2 mM [Re], $[\text{TBAPF}_6]_{\text{initial}} = 0.4$ M, and an HOPG working electrode ($A = 0.09$ cm^2) at a 100 mV/s scan rate.

The electrochemistry of the $\text{Re}(\text{CO})_3(\text{bpy})\text{Cl}$ complex agrees with that observed in the literature (Figure 5.1, lower panel). In a cyclic voltammetry experiment inside a glovebox, as the potential is swept cathodically, we pass through an initial, chemically reversible and electrochemically quasi-reversible wave. This has been attributed previously to the ligand-centered reduction of bipyridine. At more negative potentials, an irreversible reduction is observed, which has been assigned as metal-centered. The irreversibility of this event is due to the loss of chloride following reduction, and in the presence of CO_2 it is this second reduction from which catalytic current grows. Other minor

features may be observed in the voltammetry but are not of relevance to the catalysis investigated here.

Promisingly, voltammetry conducted on $\text{Re}(\text{CO})_3(\text{bpy})\text{Cl}$ at the increased pressures afforded by our reactor exhibit very high current densities relative to what is observed under ambient conditions with the same electrode (Figure 5.1, upper right panel). The quasi-reversible redox couple seen in control experiments is unperturbed by the presence of high concentrations of CO_2 , providing evidence that the catalyst appears to be behaving the same at high pressure as in more traditional experiments. Inspection of the data further reveals that there is a pressure dependence for the onset of catalysis, with higher concentrations of CO_2 leading to more positive onset potentials (Figure 5.1, upper left panel). This kinetic potential shift represents another distinct advantage of using CXEs for molecular electrocatalysis.

The conditions afforded by the use of CXE media (high substrate concentration) enable us for the first time to perform full analysis of the kinetics of $\text{Re}(\text{CO})_3(\text{bpy})\text{Cl}$. However, the absence of a plateauing feature in the catalytic wave observed in cyclic voltammetry makes quantifying the rate of the reaction difficult. To overcome this difficulty, Foot Of the Wave Analysis (FOWA) was used to find the reaction rate for $\text{Re}(\text{CO})_3(\text{bpy})\text{Cl}$ at various concentrations of CO_2 in the CXE. FOWA has extensively been used by Saveant and coworkers for benchmarking homogeneous catalysts.^{14–18} FOWA avoids many of the issues in electrocatalytic reduction of CO_2 that make kinetic analysis difficult. These issues include consumption of the CO_2 substrate, deactivation of catalyst, and product inhibition.¹⁵ FOWA avoids these issues by analyzing a cyclic voltammogram at the “foot” of the catalytic wave, the very first region where the catalyst shows activity. By analyzing this region the catalyst has not yet had enough time to create any problems for analysis.

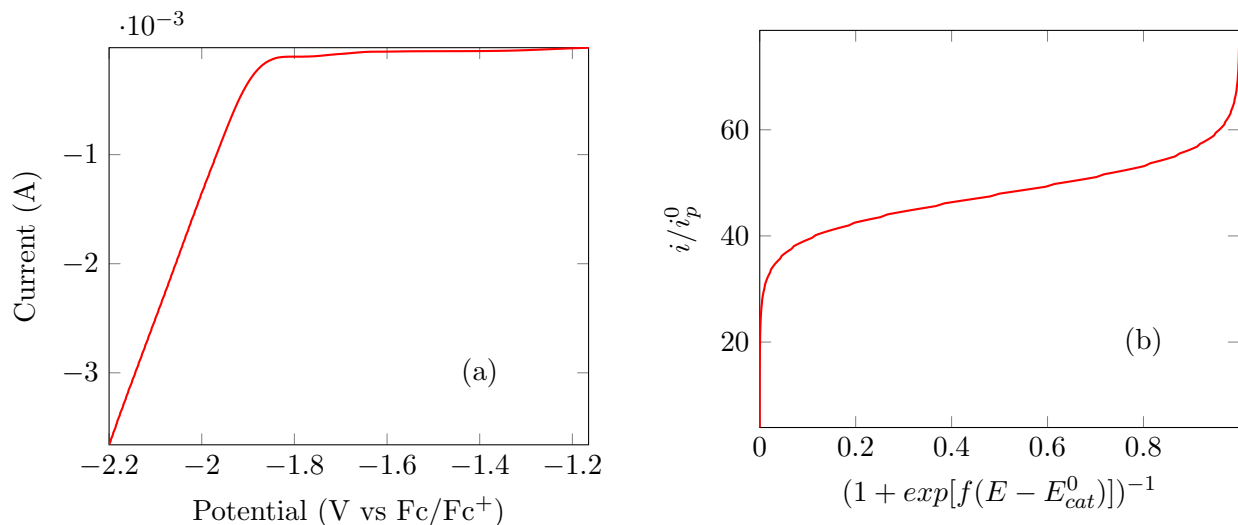


Figure 5.2. Representative $\text{Re}(\text{CO})_3(\text{bpy})\text{Cl}$ catalytic sweep at 3.13 MPa (a), Linearization of this sweep using FOWA (b)

The measurement of a kinetic rate constant at the foot of a catalytic wave by FOWA is accomplished by plotting i/i_p^0 against $(1 + \exp[f(E - E_{cat}^0)])^{-1}$ where i_p^0 is the peak current of the catalyst in the absence of substrate, $f = nF/RT$, and E_{cat}^0 is the standard catalyst potential.¹⁹ This produces a straight line, as shown in Figure 5.2, with a linear region slope of $2.24\sqrt{\frac{RT}{Fv}}2kC_A^0$ where v is the scan rate.¹⁵ This allows the calculation of the apparent rate constant. Plotting the observed rates against the concentration of CO_2 in the CXE reveals a rapid increase and then plateauing as the concentration of CO_2 increases. A decrease in the apparent rate when the expansion of the solvent becomes significant is then observed as shown in Figure 5.3.

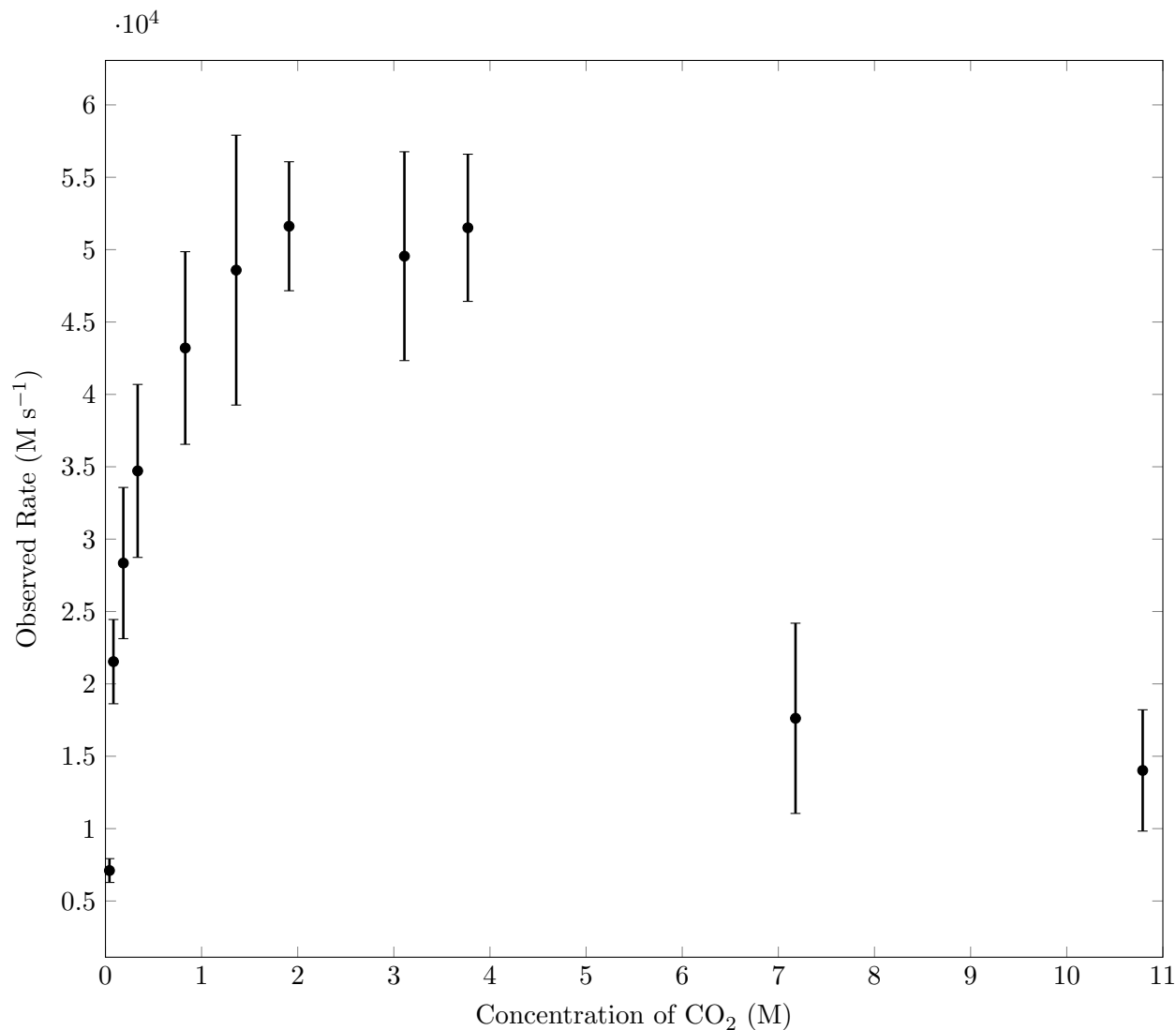


Figure 5.3. Observed rates of electrocatalytic reduction by $\text{Re}(\text{CO})_3(\text{bpy})\text{Cl}$ in CO_2 expanded acetonitrile at various concentrations of CO_2 . $\text{Re}(\text{CO})_3(\text{bpy})\text{Cl}$ concentration for all experiments calibrated to 2 mM after expansion, working electrode was the basal plane of highly-oriented pyrolytic graphite (HOPG, 0.09 cm²). 0.4 M concentration of TBAPF_6 prior to expansion. Error bars are calculated from the error of a linear fit applied to replicate experiments at multiple scan rates.

Bulk electrolysis was carried out to confirm the CV data. Table 5.1 tabulates some of this data, exhibiting the Re complex's precedented selective formation of CO, but now under our new CXE conditions. Notably, as seen in the CV data, there is a drop off in charge passed at the highest degree of expansion. Like in the heterogeneous gold system studied previously, this may arise from changes in electron transfer kinetics as the pseudo-binary solution becomes more liquid CO_2 -like, or in this case may come from yet-unidentified problems with catalyst solubility at high concentrations of CO_2 .

Table 5.1. Product Characterization Data for $\text{Re}(\text{CO})_3(\text{bpy})\text{Cl}$

Pressure (P)	$[\text{CO}_2]$ [M]	Charge Passed (Q)	Volume CO (mL)	F. Y. (%)
0.23 MPa	0.15	4.63 C	0.4	75% \pm 10%
0.51 MPa	0.3	14.37 C	1.2	73% \pm 10%
4.16 MPa	8.2	9.0 C	1.2	110% \pm 10%

Table 5.1. Table summarizing data from a series of bulk electrolysis experiments. An HOPG electrode was polarized at -2 V vs. $\text{Fc}^{+/0}$ for 5 h, after which gas was collected into a steel cylinder and quantified by gas chromatography. 2 mM [Re] catalyst, 0.4 M TBAPF₆ prior to expansion, electrode area 0.09 cm². No products besides CO were detected at any pressure.

The plateauing behavior seen in the observed rate for $\text{Re}(\text{CO})_3(\text{bpy})\text{Cl}$ resembles the Michaelis-Menten kinetic model used in enzyme catalysis, where mixed-order kinetics describe a given catalytic system. This model assumes that at low substrate concentration a first-order dependence is present and at high substrate concentration (where the catalyst is “saturated”) a zero-order dependence is present. As our catalyst is homogeneous, like enzymes are, the analogy seems fitting. For our analysis using the Michaelis-Menten kinetics we assume that the $\text{Re}(\text{CO})_3(\text{bpy})\text{Cl}$ reduction of CO_2 can be understood as a reaction where the $\text{Re}(\text{CO})_3(\text{bpy})\text{Cl}$ reacts reversibly with CO_2 to form a complex, which then reacts irreversibly to create CO and release the catalyst for further reactions as shown in Figure 5.4.

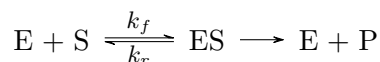


Figure 5.4. Reaction used for Michaelis-Menten kinetic model where E is the catalyst, S is CO_2 , ES is the catalyst\(CO_2 complex, and P is CO

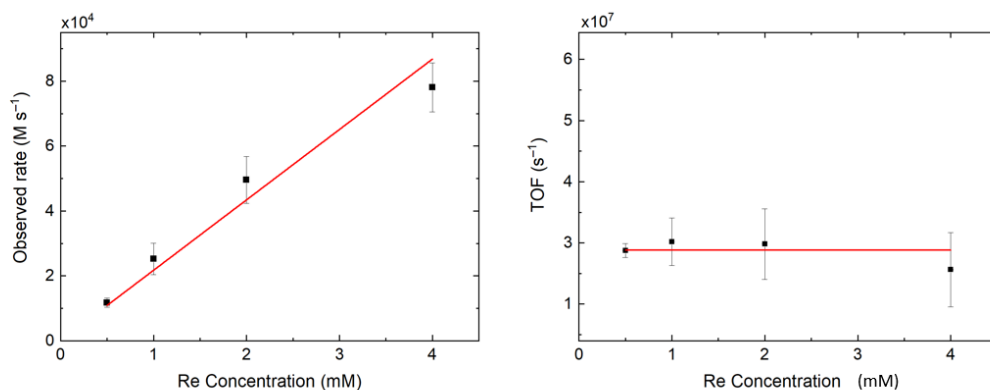


Figure 5.5. Rhenium concentration dependence of kinetics under zero-order conditions for CO₂. (left) Concentration dependence of rhenium on the calculated observed rate, determined from FOWA. Cell pressurized to 2.5 MPa CO₂ (3.5 M CO₂), working electrode was the basal plane of highly-oriented pyrolytic graphite (HOPG, 0.09 cm²). 0.4 M concentration of TBAPF₆ prior to expansion. (right) Normalized concentration dependence exhibiting linear behavior. Error bars are calculated from the error of a linear fit applied to replicate experiments at multiple scan rates.

If this reaction scheme is broadly correct, then the Michaelis-Menten equation as shown in Equation 5.1 will apply. To confirm the reaction scheme as first order in [Re(CO)₃(bpy)Cl], a series of experiments varying the initial concentration of Re(CO)₃(bpy)Cl at a set concentration of CO₂ were performed. Finding the apparent rates of reaction by FOWA confirms a first order dependence on the concentration of Re(CO)₃(bpy)Cl as shown in Figure 5.5.

$$[h]v = \frac{d[P]}{dt} = V_{max} \frac{[S]}{K_M + [S]} = k_{cat}[E]_0 \frac{[S]}{K_M + [S]} \quad (5.1)$$

Equation 5.1. Michaelis-Menten equation for enzymatic catalysis. P is product, S is substrate, V_{max} is the maximum rate of reaction K_M is the Michaelis constant which the concentration of substrate when the reaction rate is half of V_{max} , k_{cat} is the reaction rate constant, and $[E]_0$ is the initial concentration of enzyme or catalyst present

From Equation 5.1 it can be seen that when $[S] \ll K_M$ then the equation will become $v = k_{cat}[E]_0 \frac{[S]}{K_M}$ which is a first order reaction. As $[S] \gg K_M$ then the reaction order goes to zero.

Fitting the Michaelis-Menten model to the observed rates obtained by FOWA an excellent fit was obtained as shown in Figure 5.6. V_{max} , the maximum rate of reaction, was found to be $5.4 \times 10^4 M s^{-1}$ K_M , the concentration of substrate at which half V_{max} is observed, was found to be

166 mM CO₂. Using V_{max} , k_{cat} was then found from the equation $V_{max} = k_{cat}[Re]$ where the concentration of $Re(CO)_3(bpy)Cl = 2mM$ to be $k_{cat} = 2.67 \times 10^{-7} s^{-1}$. As the Michaelis-Menten is typically used for enzymes, to compare the activity of $Re(CO)_3(bpy)Cl$ to enzymes k_{cat} was divided by the Michaelis constant, K_M , to find an activity of $1.58 \times 10^8 M^{-1} s^{-1}$. This value approaches the upper limit of what is possible for specificity constants (on the order of 10^8 to $10^9 M^{-1} s^{-1}$), and suggest that like a highly efficient enzyme, under our conditions the rhenium catalyst operates in a diffusion-limited regime. In other words, the catalyst is operating at its maximum intrinsic rate, limited only by the time it takes for a substrate molecule of CO₂ to diffuse into contact with it.²⁰

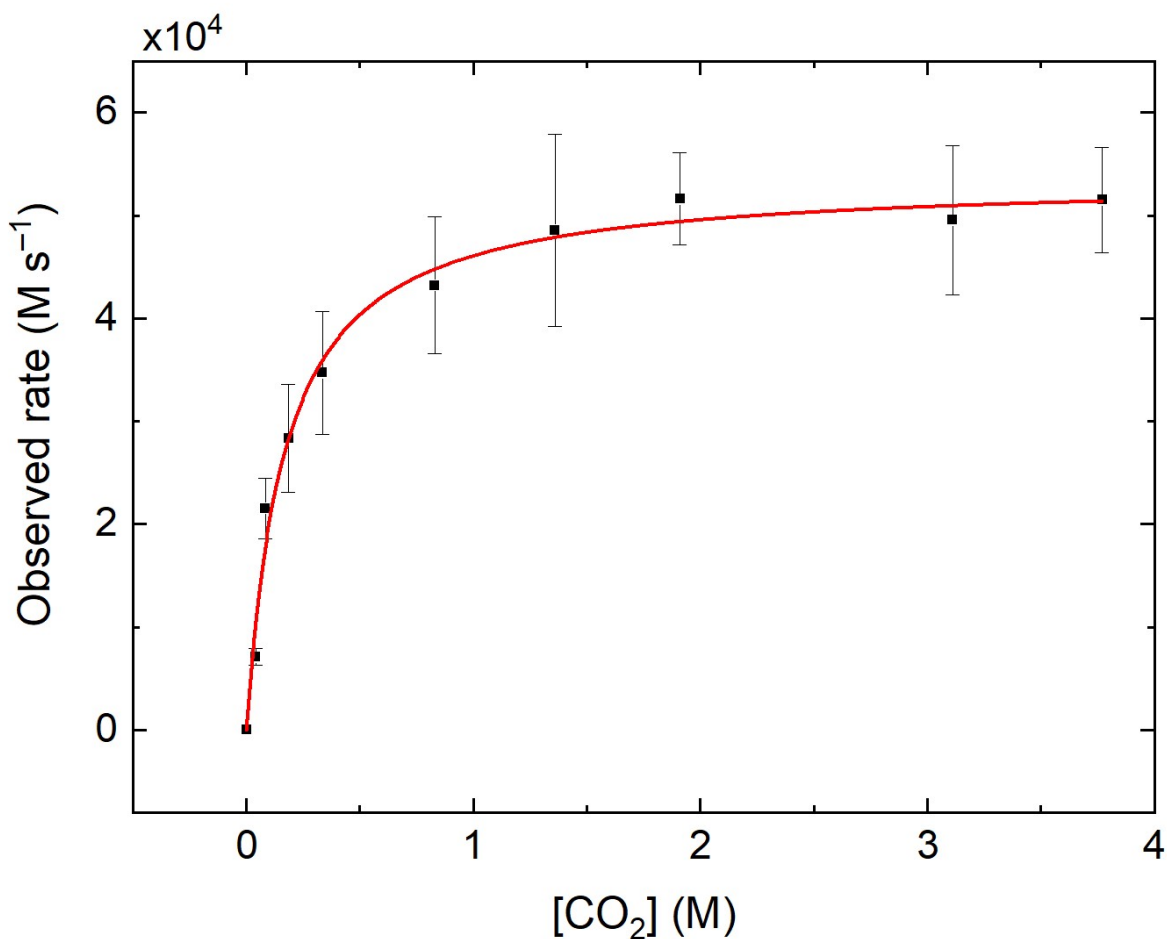


Figure 5.6. Kinetics of electrocatalysis by the rhenium complex. Rate of electrocatalysis determined by foot-of-the-wave analysis performed on cyclic voltammetry data as a function of CO₂ concentration (i.e. with increasing pressure). The red line is a nonlinear regression of the data, modeled by Michaelis-Menten kinetic model. Error bars are calculated from the error of a linear fit applied to replicate experiments at multiple scan rates.

It is believed that the decrease in catalysis seen at the highest concentrations of CO₂ derives from a change in the electron transfer coefficient as seen in the work presented in Chapter 4 on the catalytic reduction of CO₂ on gold. The change in the polarity of the solvent is most probably responsible for this change although a decrease in catalyst solubility cannot be ruled out at this time. Further work is necessary to confirm this hypothesis.

5.5 Conclusion

The use of CXEs had previously been shown to be immensely beneficial both for the electrochemical reduction of CO₂ on heterogeneous catalysts and for elucidating key mechanistic data. For the first time these benefits have been applied to a homogeneous catalyst in a CXE. It was found that the increase in catalytic rates found for heterogeneous catalysts also applies to homogeneous systems. Also similar to heterogeneous catalysts there is an optimum concentration of CO₂ for the catalytic reduction of CO₂ by Re(CO)₃(bpy)Cl. Before the possible change in the electron transfer rate becomes significant, the apparent rate of reduction obeys Michaelis-Menten kinetics. Extracting the kinetic rate constant shows that Re(CO)₃(bpy)Cl is equivalent to a diffusion limited enzyme. This is the first time that this has been shown for a homogeneous catalyst through changing the concentration of CO₂.

5.6 Acknowledgement of Contributions

Catalyst synthesis and analysis of electrochemical data was performed by David Sconyers.

5.7 Supporting Figures

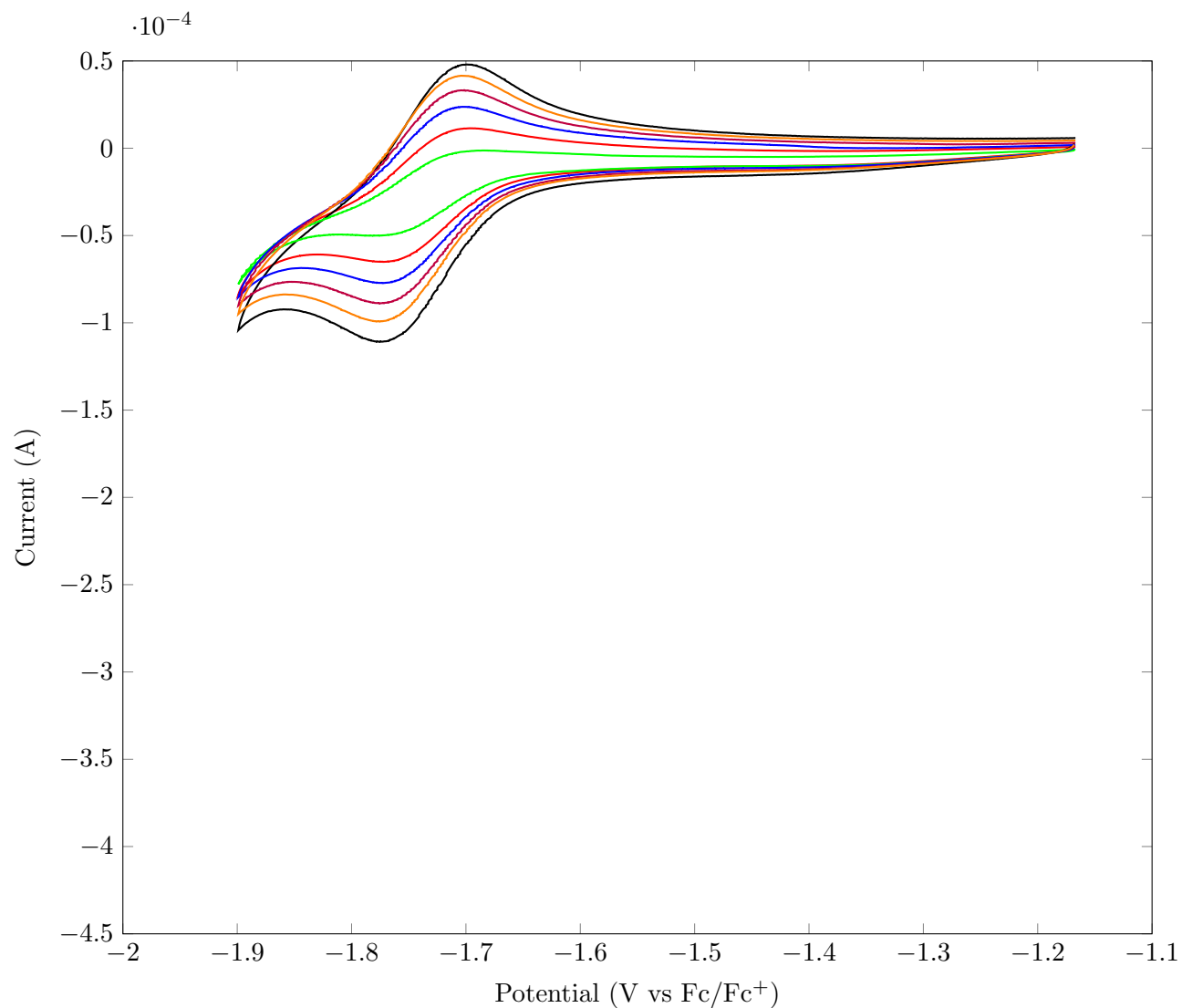


Figure 5.7. Scan rate dependence of 0.2 mM $\text{Re}(\text{CO})_3(\text{bpy})\text{Cl}$ at 0.17 MPa. Working electrode was the basal plane of highly-oriented pyrolytic graphite (HOPG, 0.09 cm²). 0.4 M concentration of TBAPF_6 prior to expansion. (Green: 50 mV/s, Red: 100 mV/s, Blue: 150 mV/s, Purple: 200 mV/s, Orange: 250 mV/s, Black: 300 mV/s)

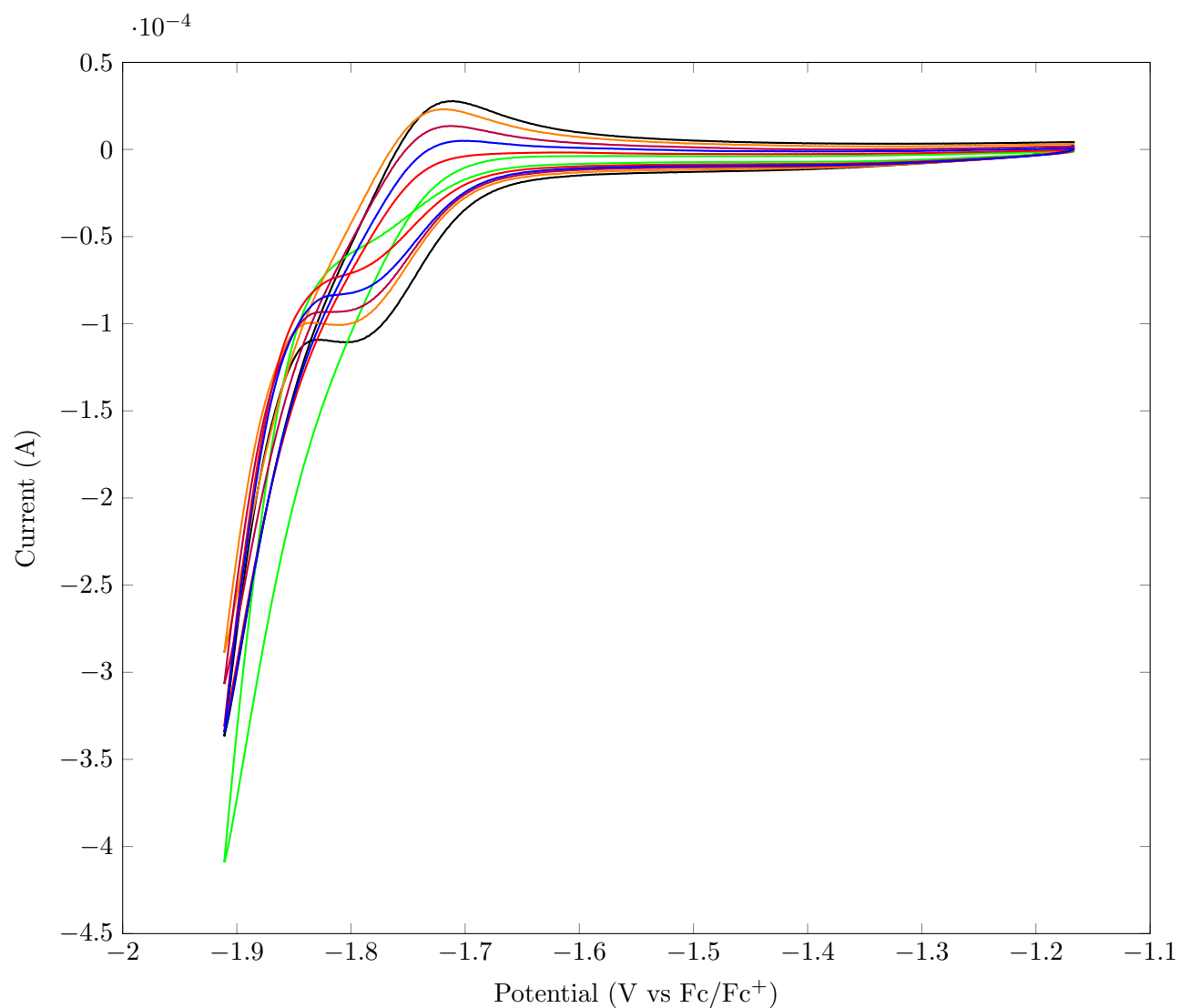


Figure 5.8. Scan rate dependence of 0.2 mM $\text{Re}(\text{CO})_3(\text{bpy})\text{Cl}$ at 2.46 MPa CO_2 . Working electrode was the basal plane of highly-oriented pyrolytic graphite (HOPG, 0.09 cm²). 0.4 M concentration of TBAPF_6 prior to expansion. (Green:50 mV/s, Red:100 mV/s, Blue:150 mV/s, Purple: 200 mV/s, Orange: 250 mV/s, Black: 300mV/s)

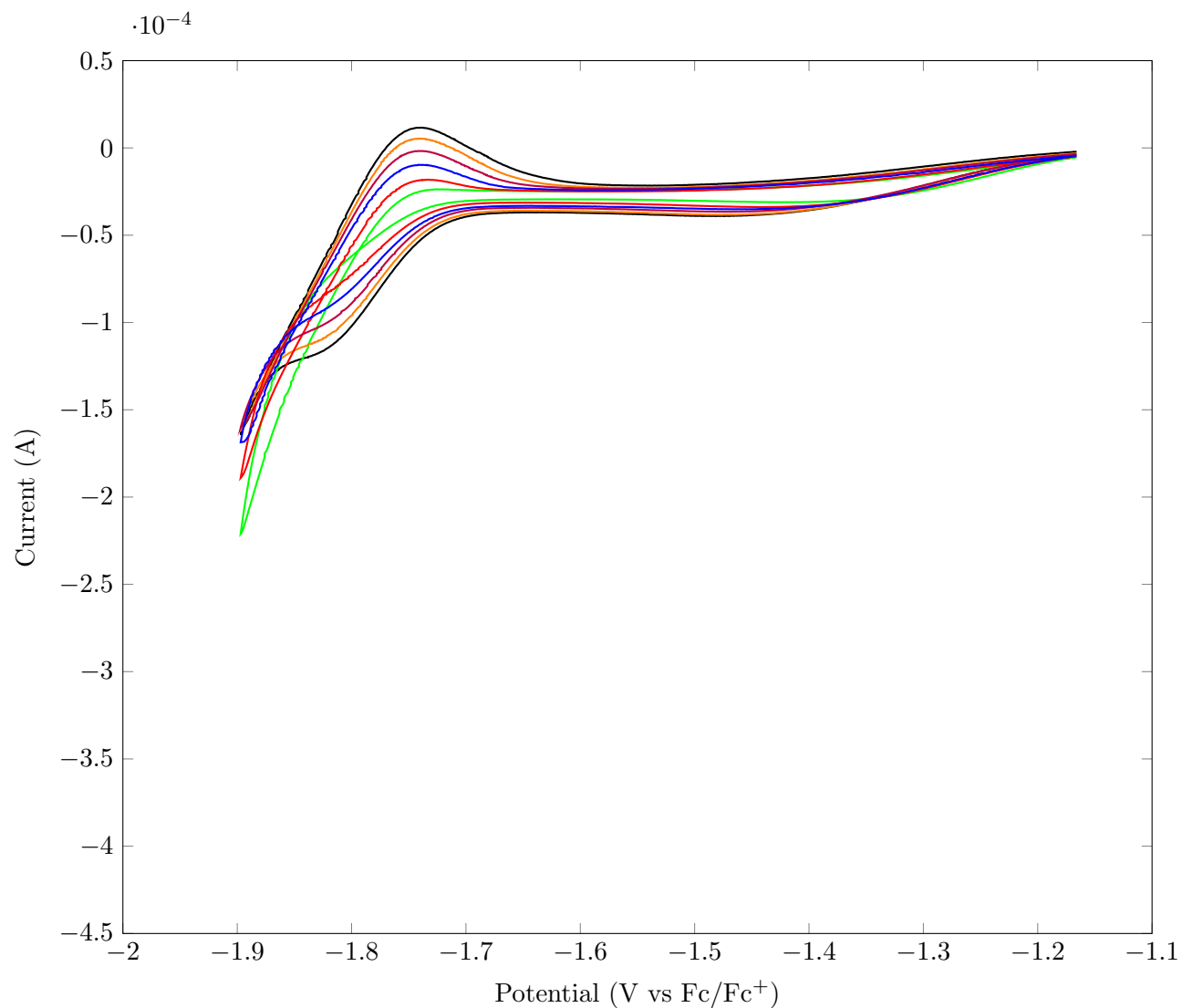


Figure 5.9. Scan rate dependence of 0.2 mM $\text{Re}(\text{CO})_3(\text{bpy})\text{Cl}$ at 2.46 MPa CO_2 . Working electrode was the basal plane of highly-oriented pyrolytic graphite (HOPG, 0.09 cm²). 0.4 M concentration of TBAPF_6 prior to expansion. (Green:50 mV/s, Red:100 mV/s, Blue:150 mV/s, Purple: 200 mV/s, Orange: 250 mV/s, Black: 300mV/s)

References

- [1] Shaughnessy, C. I., Sconyers, D. J., Kerr, T. A., Lee, H.-J., Subramaniam, B., Leonard, K. C., and Blakemore, J. D. (2018) Enhanced Electrocatalytic CO₂ Conversion in Pressure-Tunable CO₂ Expanded Electrolytes. *Unpublished*
- [2] Cosnier, S., Deronzier, A., and Moutet, J.-C. (1988) Electrocatalytic reduction of CO₂ on electrodes modified by fac-Re (2, 2'-bipyridine)(CO) 3Cl complexes bonded to polypyrrole films. *Journal of molecular catalysis* 45, 381–391.
- [3] Wong, K.-Y., Chung, W.-H., and Lau, C.-P. (1998) The effect of weak Brønsted acids on the electrocatalytic reduction of carbon dioxide by a rhenium tricarbonyl bipyridyl complex. *Journal of electroanalytical chemistry* 453, 161–170.
- [4] Hori, H., Koike, K., Suzuki, Y., Ishizuka, M., Tanaka, J., Takeuchi, K., and Sasaki, Y. (2002) High-pressure photocatalytic reduction of carbon dioxide using [fac-Re (bpy)(CO) 3P (OiPr) 3]⁺(bpy= 2, 2'-bipyridine). *Journal of Molecular Catalysis A: Chemical* 179, 1–9.
- [5] Hori, H., Takano, Y., Koike, K., and Sasaki, Y. (2003) Efficient rhenium-catalyzed photochemical carbon dioxide reduction under high pressure. *Inorganic Chemistry Communications* 6, 300–303.
- [6] Johnson, F. P., George, M. W., Hartl, F., and Turner, J. J. (1996) Electrocatalytic Reduction of CO₂ Using the Complexes [Re (bpy)(CO) 3L]_n (n=+ 1, L= P (OEt) 3, CH₃CN; n= 0, L= Cl-, Otf-; bpy= 2, 2'-Bipyridine; Otf= CF₃SO₃) as Catalyst Precursors: Infrared Spectroelectrochemical Investigation. *Organometallics* 15, 3374–3387.
- [7] Stor, G., Hartl, F., Van Outersterp, J., and Stufkens, D. (1995) Spectroelectrochemical (IR,

- UV/Vis) Determination of the Reduction Pathways for a Series of $[\text{Re}(\text{CO})_3(\text{L})_3]$ ($\text{L} = \text{halide, OTf, THF, MeCN, n-PrCN, PPh}_3, \text{P}(\text{OMe})_3$) Complexes. *Organometallics* *14*, 1115–1131.
- [8] Smieja, J. M., and Kubiak, C. P. (2010) $\text{Re}(\text{bipy-tBu})(\text{CO})_3\text{Cl}$ - improved catalytic activity for reduction of carbon dioxide: IR-spectroelectrochemical and mechanistic studies. *Inorganic chemistry* *49*, 9283–9289.
- [9] Sullivan, B. P., Bolinger, C. M., Conrad, D., Vining, W. J., and Meyer, T. J. (1985) One- and two-electron pathways in the electrocatalytic reduction of CO_2 by $\text{fac-Re}(\text{bpy})(\text{CO})_3\text{Cl}$ ($\text{bpy} = 2, 2'$ -bipyridine). *Journal of the Chemical Society, Chemical Communications* 1414–1416.
- [10] Hawecker, J., Lehn, J.-M., and Ziessel, R. (1983) Efficient photochemical reduction of CO_2 to CO by visible light irradiation of systems containing $\text{Re}(\text{bipy})(\text{CO})_3\text{X}$ or $\text{Ru}(\text{bipy})_3^{2+}$ - Co^{2+} combinations as homogeneous catalysts. *Journal of the Chemical Society, Chemical Communications* 536–538.
- [11] Morris, A. J., Meyer, G. J., and Fujita, E. (2009) Molecular approaches to the photocatalytic reduction of carbon dioxide for solar fuels. *Accounts of chemical research* *42*, 1983–1994.
- [12] Sampson, M. D., Froehlich, J. D., Smieja, J. M., Benson, E. E., Sharp, I. D., and Kubiak, C. P. (2013) Direct observation of the reduction of carbon dioxide by rhenium bipyridine catalysts. *Energy & Environmental Science* *6*, 3748–3755.
- [13] Juris, A., Campagna, S., Bidd, I., Lehn, J. M., and Ziessel, R. (1988) Synthesis and photophysical and electrochemical properties of new halotricarbonyl (polypyridine) rhenium (I) complexes. *Inorganic Chemistry* *27*, 4007–4011.
- [14] Costentin, C., Passard, G., Robert, M., and Savéant, J.-M. (2014) Ultraefficient homogeneous catalyst for the CO_2 -to-CO electrochemical conversion. *Proceedings of the National Academy of Sciences* *111*, 14990–14994.
- [15] Costentin, C., Drouet, S., Robert, M., and Saveant, J.-M. (2012) Turnover numbers, turnover frequencies, and overpotential in molecular catalysis of electrochemical reactions. Cyclic

- voltammetry and preparative-scale electrolysis. *Journal of the American Chemical Society* 134, 11235–11242.
- [16] Costentin, C., Drouet, S., Passard, G., Robert, M., and Saveant, J.-M. (2013) Proton-coupled electron transfer cleavage of heavy-atom bonds in electrocatalytic processes. Cleavage of a C–O bond in the catalyzed electrochemical reduction of CO₂. *Journal of the American Chemical Society* 135, 9023–9031.
- [17] Costentin, C., Robert, M., and Saveant, J.-M. (2013) Catalysis of the electrochemical reduction of carbon dioxide. *Chemical Society Reviews* 42, 2423–2436.
- [18] Costentin, C., Drouet, S., Robert, M., and Saveant, J.-M. (2012) A local proton source enhances CO₂ electroreduction to CO by a molecular Fe catalyst. *Science* 338, 90–94.
- [19] Costentin, C., Robert, M., and Saveant, J.-M. (2013) Catalysis of the electrochemical reduction of carbon dioxide. *Chem. Soc. Rev.* 42, 2423–2436.
- [20] Berg, J., Tymoczko, J., and Stryer, L. (2002) Section 8.4-The Michaelis-Menten Model Accounts for the Kinetic Properties of Many Enzymes. *Biochemistry, fifth ed.* WH Freeman, New York. Available from: <http://www.ncbi.nlm.nih.gov/books/NBK22430>

Chapter 6

Conclusions and Future Work

6.1 Conclusion

The recurring theme of the preceding chapters is that the electrochemical reduction of CO_2 is a complex process. To achieve the maximum catalytic effects for a given catalyst or catalyst system, the conditions must be carefully adjusted. By in-situ reduction of the In_2O_3 nanoparticles to form an In^0 - In_2O_3 composite structure the reduction product selectivity was changed from the typical bulk indium product, formate, to CO. We attribute this change to the native oxide layer that is typically present on bulk indium being removed and the surface encountered by the CO_2 being In^0 instead of In_2O_3 . This change of environment makes the first electron transfer step reversible, which suggests that the mechanism may be different on the two different materials. During the process of characterizing this catalyst we also utilized Substrate Generation-Tip Collection Scanning Electrochemical Microscopy (SG-TC SECM) to investigate the potential dependent product detection of the catalyst. This technique was an improvement on bulk electrolysis to create enough product to analyze via gas chromatography. It was easier and faster than gas chromatography due to the elimination of the need to create a gas tight reactor for the reaction, with the narrow tip-substrate distance effectively containing the products for the simultaneous analysis.

With the switch in focus from catalyst to catalytic systems which began when we began work with CO_2 eXpanded Electrolytes (CXEs) the complexity of CO_2 reduction came into greater focus. Beginning the development of CXEs as electrochemical media, we found that tetraethylammonium hexafluorophosphate (TEAPF_6) was not soluble at all degrees of expansion while tetrabutylam-

monium hexafluorophosphate (TBAPF₆) was. The expansion of 0.4M TBAPF₆ was found to be lower than the neat acetonitrile at a given pressure. We then established the concentrations of CO₂ at various degrees of expansion both with and without electrolyte present in the solution. It was found that the concentration of CO₂ was the same with respect to degree of expansion for both with and without electrolyte. This holds regardless of the fact that a higher headspace pressure of CO₂ to achieve a given degree of expansion is required for solutions containing electrolyte. We then established with a model electrochemical compound (ferrocene) that not only was electrochemistry possible at all degrees of expansion, but that aside from a minor increase in the diffusion coefficient, it behaved identically to normal ambient pressure electrochemistry. For CO₂ electrocatalytic reduction it was assumed that the increase in CO₂ concentration would lead to a monotonic increase in the reaction rate up to a possible catalytic site limited regime. This was found to not be the case. Instead of a plateau we observed a maximum catalytic current and then a decrease to ambient pressure levels of current at the highest degrees of expansion. The maximum current observed was an order of magnitude higher than previously reported so the objective of increasing the catalytic activity was met. The decrease, however, was puzzling. The decrease was observed in two heterogeneous catalytic systems (Au and Cu), and one homogeneous system (Re(CO)₃(bpy)Cl). The decrease was confirmed by quantitative gas chromatography.

To investigate the decrease in catalytic rate, COMSOL modeling was utilized. For the first time, a microkinetic model of CO₂ reduction incorporating the accepted reaction mechanism for gold in acetonitrile was created. Utilizing this model to fit cyclic voltammograms at key CO₂ pressures (0.17, 3.13, and 5.10 MPa) it was found that the driving factor behind the decrease in the rate of catalysis is the decrease in the rate of the first electron transfer step. We theorize that the reason behind this decrease is that as the CO₂ begins to be the dominant molecule in the electrolyte solution, the reorientation necessary for it to accept an electron becomes more difficult, as the partial negatives are not supported by the increasingly nonpolar solution. Evidence backing up this hypothesis is that the rate of the first electron transfer step does not fall until the expansion of the solvent becomes significant.

Continuing the investigation of CXEs as media for electrocatalytic reduction, we wished to try a homogeneous catalyst. We used Re(CO)₃(bpy)Cl, which has previously been extensively investigated at ambient CO₂ pressures. By utilizing the tunability of CO₂ concentration enabled by

CXEs to generate cyclic voltammograms at widely separated concentrations of CO_2 , the kinetics of $\text{Re}(\text{CO})_3(\text{bpy})\text{Cl}$ were investigated. The observed rates increased to a plateauing rate with increasing concentration of CO_2 . These rates match well with Michealis-Menten kinetics for enzymatic catalysis. Using the Michealis-Menten equation the kinetic rate constant for electrocatalytic reduction was found. Past the plateau region, a reduction in the catalytic rate was observed at the highest degree of expansion, consistent with what was observed for both gold and copper catalysts.

As seen, the complexities of CO_2 electrocatalytic reduction contribute to fundamental problems for the field. Contributions of this work to the field of CO_2 electrocatalytic reduction address three of the fundamental problems identified including:

1. Low product selectivity (Chapter 2)
2. Low catalyst activity (Chapter 3 and 5)
3. Insufficient fundamental understanding of electrocatalytic reduction (Chapters 4 and 5)

These contributions will advance CO_2 electrocatalytic reduction towards industrial adoption.

6.2 Future Work

The use of CXEs for electrocatalysis involving CO_2 is very exciting. The work in this dissertation has established that they can enhance the rates of CO_2 electrocatalytic reduction by an order of magnitude. In addition, the tunability of CO_2 concentration that they enable, allows investigations into the fundamental reaction kinetics for the electrocatalytic reduction of CO_2 . This combination has already been shown to address three of the five largest obstacles to the adoption of CO_2 electrocatalytic reduction and has the potential to address the last two as well. In addition, there are other electrocatalytic reactions, such as electrocarboxylation, that could benefit from the utilization of CXEs. The investigation of these areas will be an excellent way to attempt to bring electrocatalytic technology to industrial relevance.

The first, and easiest, direction that the continuing investigation into the utilization of CXEs should go is using their tunable properties in combination with an understanding of the basic reaction kinetics to attempt to change product distribution. For the basic work, we specifically

chose gold as a catalyst to investigate because in acetonitrile it is known to exclusively utilize the aprotic adsorbed mechanism for CO₂ reduction shown in Figure 1.2.³ Future work should investigate other catalysts such as iron or titanium which can reduce CO₂ by either adsorbed or nonadsorbed reaction pathways in organic media (Figs. 1.2 and 1.4) to see if the product distribution can be tuned by the change in solvent properties. These changes, in Chapter 4, were shown to affect the kinetic rate constant in the first electron transfer step. As shown by several metals such as tin and indium which tend towards the adsorbed reaction product (CO) in organic media and the nonadsorbed reaction product (HCCO) in aqueous media, the environment that the catalyst is in can have an important role in product selectivity. It is highly probable that the ability to tune the solvent from a mildly polar environment to a mostly nonpolar CO₂ environment will change the product distribution for catalysts that are less selective than gold.

Following this fundamental study to further understand the media, the focus should be upon finding ways to address the final two obstacles outlined in the introduction, catalyst stability and reactor design. Of these two the first to be investigated should be the reactor design. The current batch reactor is excellent for basic electrochemistry in CXEs and to gain data to understand the fundamentals of the electrocatalytic reduction mechanisms. It, however, is completely unsuitable for industrial use. The problems are:

1. Uncontrolled reaction products
2. Reactor employs an undivided cell
3. Reactor is a batch reactor

The problem of the uncontrolled oxidation products can be seen in Figure 6.1. The tar-like substance on the platinum wire counter electrode is hypothesized to be either oxidized acetonitrile or TBAPF₆ electrolyte. The oxidation of solvent would be unacceptable in an industrial process from an economic standpoint. In addition this oxidation product seems to foul the cell after long electrolyses and would be detrimental to the catalyst longevity. One method that may be possible to increase catalyst longevity is to keep oxidative products from reaching the surface of the catalyst.

The issue of the uncontrolled oxidation products leads to the second problem. The normal method of addressing the problem of keeping oxidative products from reaching the cathode is to



Figure 6.1. Electrodes after a chronoamperometry experiment using the current reactor. This shows the oxidation product buildup on the counter electrode

have a divided cell utilizing a membrane. Polymer Electrolyte Membranes (PEMs) are extensively used in water splitting reactors to maintain electrical conductivity while keeping the cathode and anode separate.¹⁷⁷ These work well for water electrolysis, but have not been used in GXLs before. The high pressure and organic environment may pose serious problems for typical membranes. An alternative membrane-less approach may be possible however. During preliminary experiments attempting to control the oxidation reaction by adding water, separate liquid phases were observed. This was unusual as acetonitrile is typically considered miscible with water at all concentrations. The experiments with water oxidation to act as the proton source in the system were discontinued to focus attention on the reduction of CO_2 but the separate phases offer the possibility to separate the oxidation reaction and the reduction reaction. Simply place the anode in a water rich phase and the cathode in the acetonitrile/ CO_2 phase. The largest problem anticipated for this is that a selective catalyst would need to be used to avoid parasitic water reduction. These catalysts have already been developed though so this would not be insurmountable. One possibility would be to use the $\text{In}^0\text{-In}_2\text{O}_3$ catalyst developed in Chapter 2. This control over the oxidative reaction is necessary before developing a continuous process.

Finally, once the issue of the oxidation reaction is dealt with, for a continuous process a batch reactor is inherently unsuitable. The necessity of depressurizing the current reactor to extract products would severely cut into the productivity of a given system. A continuous flow reactor

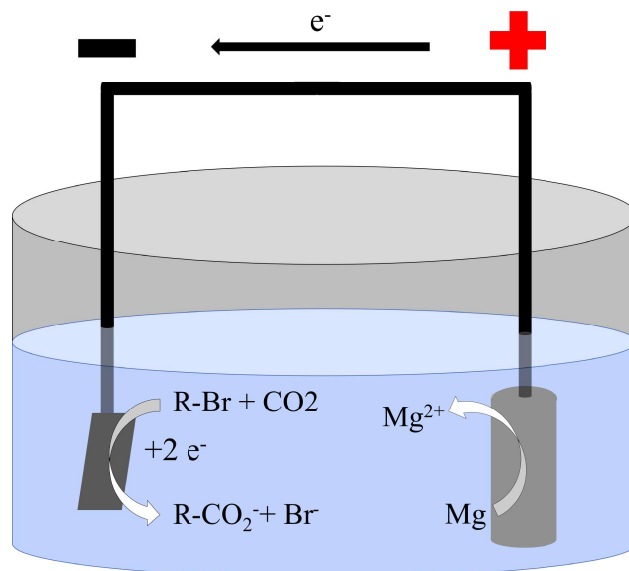


Figure 6.2. Schematic of an experimental electrocarboxylation setup utilizing a sacrificial anode

would need to be created, possibly utilizing a high surface area open cell metal foam or carbon cloth supported catalyst would need to be created.

Once this continuous process is created the need for increased catalyst stability will leap into the forefront. It is possible that the high activity that CXEs enable will allow the use of less elegantly structured catalysts which have high stability. For example if instead of nanostructured gold, simple dispersed gold nanoparticles are used, it may be anticipated that the nanoparticles should have higher stability. Once the stability concerns have been addressed, a continuous process with the high catalyst activity enabled by CXEs make development of an electrocatalytic CO_2 reduction process attractive for industrial use of CO_2 .

Extending the use of CXEs beyond CO_2 electrocatalytic reduction is also an exciting possibility. One reaction that seems promising is electrocarboxylation. Electrocarylation is excellent from the standpoint of using as much CO_2 as possible because it uses one electron per CO_2 molecule incorporated as opposed to electrocatalytic reduction which needs at least two for CO or formate, and can range higher to make higher value molecules. Electrochemical carboxylation has been studied under a variety of conditions and with a variety of substrates. The literature record on electrocarboxylation begins in the early 1960s with a patent by Loveland detailing the production of acyclic carboxylic acids from butadiene.¹⁷⁸ Loveland performed his work in a divided cell which can impose high ohmic losses. Shortly thereafter Gambino and Silvestre published a technique in

which they utilized a sacrificial aluminum anode to electrocarboxylate ethylene.¹⁷⁹ This technique rapidly became the most widely used way to study the carboxylation of a variety of substrates.¹⁸⁰ The carboxylation of a variety of different types of substrates has been conducted with sacrificial anodes as shown in Figure 6.2 with a generic halide. There are two possibilities for how an electrocarboxylation can occur. The first route is when the cathode reduces the CO₂ first which then subsequently adds to the substrate. In the second route the substrate is first reduced and then attacks the CO₂. Which route taken depends both on the substrate and the catalyst.¹⁸¹

Although most of the literature reports on carboxylation reactions are run at low pressures, two reports, both carboxylating halides, have utilized supercritical CO₂. Tateno et al reports that the current efficiency in an ionic liquid increases from 32 percent at atmospheric CO₂ to 60 percent at 10 MPa on a Pt working electrode.⁶⁷ Chanfreau et al reports that for electrocarboxylation of benzyl chloride in supercritical CO₂ and in a DMF GXL that there existed an optimum pressure for selectivity at 6 MPa with experiments conducted at 1,6,7 and 8 MPa.⁶⁸ The existence of an optimum pressure for benzyl chloride suggests that there will be one as well for other carboxylation reactions. This report on using a GXL for electrochemistry neglects all pressures between 1 and 6 MPa. Since there exists a maximum for current density at 3 MPa for the electrochemical reduction of CO₂ to CO it seems that further investigation in this pressure region would be warranted for electrocarboxylation.¹⁶⁶ Investigating electrocarboxylation reactions in CXEs could initially be performed in the current reactor setup utilized for the electrocatalytic reduction experiments. Target electrocarboxylation reactions for research could involve halides or alkenes.

Using sacrificial anodes sidesteps the problems encountered with oxidizing the solvent, while giving rise to different problems. The first is that the use of a sacrificial anode obviously necessitates putting metal ions into solution, which is problematic from a green chemistry standpoint.¹⁸² In addition, the recovery of metals imposes additional cost and complexity to the process. Another issue is, as the anode is used up, the distance between the electrodes changes, which can lead to a change in the voltage necessary to drive the reaction.¹⁸³ In addition, the precipitation of insoluble salts, while desirable from a product separation standpoint, can foul the cathode and inhibit current.¹⁸⁴ These problems indicate that the sidestep is not the best way to continue working with electrocarboxylation. Instead, using the biphasic system in CXEs already outlined may be better.

6.3 Final Thoughts

The large scale industrial adoption of electrochemical reduction of CO₂ has some major problems, many of which have been addressed in this dissertation. The main obstacles to adoption are (1) low catalyst activity, (2) low product selectivity, (3) insufficient catalyst stability, (4) insufficient fundamental understanding, (5) and non-optimized reactor and system design. Chapter 2 has shown a synthetic route to make a selective catalyst from indium nanoparticles to eliminate competitive water reduction in aqueous electrolyte (Obstacle 2). In Chapters 3-5 I have detailed efforts to create a new electrochemical reaction medium from Gas eXpanded Liquids (GXLs). These efforts succeeded and resulted in both an order of magnitude improvement in catalyst activity (Obstacle 1) while retaining and even slightly improving catalytic selectivity (Obstacle 2) as well as an improved understanding of the fundamental reaction kinetics of CO₂ reduction (Obstacle 4). Moving forward the future of this project and field will be addressing catalyst stability and reactor design (Obstacles 3 and 5).

References

- [1] Hori, Y. i. *Modern aspects of electrochemistry*; Springer, 2008; pp 89–189.
- [2] Carmo, M., Fritz, D. L., Mergel, J., and Stolten, D. (2013) A comprehensive review on PEM water electrolysis. *International journal of hydrogen energy* 38, 4901–4934.
- [3] Loveland, J. W. Electrolytic production of acyclic carboxylic acids from hydrocarbons. 1962; US Patent 3,032,489.
- [4] Gambino, S., and Silvestri, G. (1973) On the electrochemical reduction of carbon dioxide and ethylene. *Tetrahedron Letters* 14, 3025 – 3028.
- [5] Zhang, Y., Yu, S., Luo, P., Xu, S., Zhang, X., Zhou, H., Du, J., Yang, J., Xin, N., Kong, Y., Liu, J., Chen, B., and Lu, J. (2018) Fixation of CO₂ along with bromopyridines on a silver electrode. *Open Science* 5.
- [6] Mattheissen, R., Fransaer, J., Binnemans, K., and De Vos, D. E. (2014) Electrocarboxylation: towards sustainable and efficient synthesis of valuable carboxylic acids. *Beilstein journal of organic chemistry* 10, 2484.
- [7] Tateno, H., Nakabayashi, K., Kashiwagi, T., Senboku, H., and Atobe, M. (2015) Electrochemical fixation of CO₂ to organohalides in room-temperature ionic liquids under supercritical CO₂. *Electrochimica Acta* 161, 212 – 218.
- [8] Chanfreau, S., Cognet, P., Camy, S., and Condoret, J.-S. (2008) Electrocarboxylation in supercritical CO₂ and CO₂-expanded liquids. *The Journal of Supercritical Fluids* 46, 156 – 162.
- [9] Shaughnessy, C. I., Sconyers, D. J., Kerr, T. A., Lee, H.-J., Subramaniam, B., Leonard, K. C.,

- and Blakemore, J. D. (2018) Enhanced Electrocatalytic CO₂ Conversion in Pressure-Tunable CO₂ Expanded Electrolytes. *Unpublished*
- [10] Anastas, P. T., and Warner, J. C. *Green chemistry: theory and practice*; Oxford university press Oxford, 2000; Vol. 30.
- [11] Matthesen, R., Fransaer, J., Binnemans, K., and DeVos, D. E. (2015) Paired Electrosynthesis of Diacid and Diol Precursors Using Dienes and CO₂ as the Carbon Source. *ChemElectroChem* *2*, 73–76.
- [12] Senboku, H., Nagakura, K., Fukuhara, T., and Hara, S. (2015) Three-component coupling reaction of benzylic halides, carbon dioxide, and N,N-dimethylformamide by using paired electrolysis: sacrificial anode-free efficient electrochemical carboxylation of benzylic halides. *Tetrahedron* *71*, 3850 – 3856.